LBNL-38973
UC-404

ERNEST ORLANDO LAWRENCE
BERKELEY NATIONAL LABORATORY

X-ray Spectroscopy of Manganese Clusters

M.M. Grush
Energy and Environment Division

June 1996
Ph.D. Thesis

LBL-38973
UC-404

X-ray Spectroscopy of Manganese Clusters

by

Melissa Marie Grush
Ph.D. Thesis

Department of Applied Science
University of California
Davis, California 95616

and

Energy & Environment Division
Ernest Orlando Lawrence Berkeley National Laboratory
University of California
Berkeley, California 94720

June 1996

This work was funded by the Director, Office of Energy Research, Office of Health and Environmental Research, of the U.S. Department of Energy under Contract No. DE-AC03-76SF00098, by the National Institutes of Health under Contract No. GM-44380 and GM-48145, and by the ACS Petroleum Research Fund under Contract No. 25912-AC3.

X-ray Spectroscopy of Manganese Clusters

Abstract

Two examples of chemical conversions in metalloproteins which require the redox properties of manganese are the detoxification of hydrogen peroxide by Mn catalase and the oxidation of water in Photosystem II. Understanding these redox cycles requires a knowledge of both oxidation states and local structure of the manganese. K-edge x-ray absorption spectroscopy (XAS) is often used for investigating electronic and molecular structure.

Much of this thesis represents the groundwork necessary in order to probe Mn clusters more productively than with conventional Mn K-edge XAS and is presented in Part I. Part II contains the application of x-ray techniques to Mn metalloproteins and includes a prognosis at the end of each chapter.

Individual Mn oxidation states are more readily distinguishable in Mn L-edge spectra. An empirical mixed valence simulation routine for determining the average Mn oxidation state has been developed. The first Mn L-edge spectra of a metalloprotein were measured and interpreted.

The energy of Mn Kβ emission is strongly correlated with average Mn oxidation state. Kβ results support oxidation states of $Mn(III)_2(IV)_2$ for the S_1 state of Photosystem II while chemically reduced preparations contain predominately Mn(II).

A strength and limitation of XAS is that it probes all of the species of a particular element in a sample. It would often be advantageous to selectively probe different forms of the same element. The first demonstration that

chemical shifts in x-ray fluorescence energies can be used to obtain oxidation state-selective x-ray absorption spectra is presented. Spin-dependent spectra can also be used to obtain a more simplified picture of local structure. The first spin-polarized extended x-ray absorption fine structure using Mn Kβ fluorescence detection is shown.

The Ca binding sites(s) near the Mn cluster in Photosystem II were examined by conventional extended x-ray absorption fine structure (EXAFS). The feasibility of Tb and Ca EXAFS was investigated, resulting in the first experiments from the point of view of the Ca^{2+} binding site, instead of the Mn. A Mn-Ca^{2+} binding site interaction was observed at ~3.3 Å.

To those who believed I could finish,
especially Matthew

Acknowledgements

This work has been performed in Professor Stephen Cramer's laboratories at the University of California, Davis, and Lawrence Berkeley National Laboratory. I am grateful to him for providing me with an opportunity to learn about x-ray spectroscopy as well as for giving me freedom in exploring these projects.

X-ray experiments were carried out at the Advanced Light Source (Berkeley, California), European Synchrotron Radiation Facilite (Grenoble, France), National Synchrotron Light Source (Brookhaven, New York), and Stanford Synchrotron Radiation Laboratory (Stanford, California) with the help of the support staff at each of these facilities. Inorganic model compounds were provided through collaborations with George Christou (Indiana University), Bill Armstrong (Boston College), Vince Peccoraro (University of Michigan, Ann Arbor), and Sergiu Gorun (Exxon) - many thanks to them and their graduate students for taking time to synthesize what I needed for my experiments and a special thanks to Mike Wemple who provided the majority of the compounds which are presented here. Protein samples were provided by Jim Penner-Hahn (University of Michigan, Ann Arbor), Mel Klein (University of California, Berkeley), Wayne Frasch (Arizona State University), and Dave Britt (University of California, Davis). Again, thanks to their graduate students and especially to Tim Stemmler for all of the catalase samples and both Pam Riggs and Pam deMarois for most of the Photosystem II samples. In all cases I had the luxury of being provided with the finished product except for the PSII L-edge experiments where I had the opportunity to work on sample preparation in Mel Klein's laboratory - thanks to Henk Visser for taking time away from his own thesis project.

I have enjoyed knowing many of the current and past members of the Cramer Group and "other related people" who have participated in venting steam at the coffee house, helping with data collection, and being more or less supportive of the PSII experiments even while scratching their heads and wondering why on earth anyone would want to work on a light sensitive system. And thanks, Jason, for cheerleading the PSII.

Most of all, I need to thank my husband, Matthew Latimer, for his unwavering support as well as for being an inspiration - in letting me bounce ideas off him and in being patient when beamtime seemed to drag on forever. We are both very lucky to have supporting families and I am grateful to them for continuing to believe in me.

Table of Contents

Abbreviations

ALS	Advanced Light Source
acac	acetylacetonate
acen	dianion of N,N'-ethylenebis(acetylacetone imine)
biphen	2,2'-biphenol
bipy or bpy	2,2'-dipyridyl
dbmH	dibenzoyl-methane
ESRF	European Synchrotron Radiation Facilite
EPR	Electron Paramagnetic Resonance
EXAFS	Extended X-ray Absorption Fine Structure
Htphpn	n,N,N',N'-tetra(2-methylpyridyl)-2-hydroxypropanediamine
Me	methyl
"Mn_{16}"	$[Ba_8Na_2ClMn_{16}(OH)_8(CO_3)_4L_8]\cdot 53H_2O$, L=1,3-diamino-2-hydroxy-propane-N,N,N',N'-tetraacetic acid
NBu_4	tetrabutylammonium
NSLS	National Synchrotron Light Source
OEC	Oxygen-Evolving Complex
ph	phenyl
phen	1,10-phenanthroline
pic	picolinate
picpn	picolinimino propane
PSII	Photosystem II
PSII-Ca	PSII samples which have had some of the adventitious Ca^{2+} removed

PSII-Tb	PSII with Tb^{3+} substituted for Ca^{2+}, ~8 Tb per PSII
PSII-Tb-lo	PSII with Tb^{3+} substituted for Ca^{2+}, ~1 Tb per PSII
PSII-Sr	PSII with Sr^{2+} substituted for Ca^{2+}
py	pyridine
pz	pyrazolyl
SPEXAFS	Spin Polarized EXAFS
SSRL	Stanford Synchrotron Radiation Laboratory
XANES	X-ray Absorption Near Edge Structure
XAS	X-ray Absorption Spectroscopy

Introduction

Manganese can be an important part of redox reactions. Examples of chemical conversions in metalloproteins which require the redox properties of Mn clusters are the detoxification of hydrogen peroxide by Mn catalase (Penner-Hahn, 1992) and the oxidation of water in Photosystem II (Debus, 1992). A potential redox role for Mn is in rechargeable batteries. The possibility of replacing Ni with Mn in Li batteries has been suggested as a less expensive and less toxic alternative (Thackeray et al., 1983). Understanding redox cycles - both the electronic and structural changes - requires a knowledge of both the oxidation states and the local structure of the Mn clusters.

X-ray absorption spectroscopy (XAS) has long been a popular tool for investigating electronic and molecular structure. With the advent of high brightness synchrotron sources, using XAS to study the active sites of many dilute systems, such as metalloproteins, has become feasible (Cramer et al., 1988; Stohr et al., 1992). However, as conventionally measured, K-edge XAS techniques have inherent limitations restricting the amount of information obtainable (Chapter 1).

The use of K-edge x-ray absorption near edge structure (XANES) to determine individual Mn oxidation states in a cluster is complicated by the sensitivity of the edge position to both electronic configuration and interatomic distances. Until recently, XAS applications to metalloproteins have ignored the potential of the soft x-ray regime ($\leq$ 2.5 keV) and instead concentrated only on the hard x-ray region (from about 4 keV up to ~20 keV). However, Mn L-edge XAS yields spectra in which individual Mn oxidation states are more readily distinguishable due to their sharper resolution

(Chapter 2) as compared to Mn K-edges. An empirical mixed valence simulation routine for determining the relative amounts of Mn oxidation states in a cluster is presented in Chapter 2 and applied to super-oxidized Mn catalase (Chapter 4). In addition, the reduced form of Mn catalase is interpreted by ligand field atomic multiplet calculations and by comparison to model compound spectra (Chapter 4). These are the first Mn L-edge spectra from metalloproteins. The measurement of Mn L-edges on Photosystem II was also attempted (Chapter 5).

One of the strengths of XAS is element specificity. When studying a metalloprotein, it is generally possible to perform XANES and extended x-ray absorption fine structure (EXAFS) experiments which probe a single element by selecting energy regions which are free from other absorption edges. However, probing the totality of a particular element in a sample can also be a limitation. The relatively low resolution between components results in XANES and EXAFS analysis of mixtures having great difficulty in untangling overlapping features. These techniques generally can not distinguish between different environments surrounding individual sites of the same element and instead obtain information about the average environment. In samples containing heterogeneity in the chemical state of the element and/or local environment, it would be advantageous to selectively probe different oxidation or spin states of the same element. The first demonstration that chemical shifts in x-ray fluorescence energies can be used to obtain site-selective x-ray absorption spectra is presented in Chapter 3. This technique has been applied to Photosystem II (Chapter 6). Another technique that can potentially yield a more simplified picture of local structure is spin-selective EXAFS (Chapter 3).

Although the major portion of this thesis has involved developing novel x-ray techniques as applicable to Mn-containing systems, conventional EXAFS was used in order to investigate the Ca binding sites(s) near the Mn cluster in Photosystem II. In addition to performing Mn K-edge experiments, I have also investigated the potential of both Tb and Ca EXAFS for probing Photosystem II. This resulted in the first EXAFS experiments from the point of view of the Ca binding site, instead of that of the Mn (Chapter 7).

Part I of this thesis (Chapters 1 through 3) represents the groundwork necessary in order to probe Mn containing clusters more productively than previously possible using conventional Mn K-edge XAS. The application of x-ray techniques to Mn metalloproteins is presented in Part II (Chapters 4 through 7). Following each of the oxygen-evolving complex chapters (Chapters 5 through 7), a prognosis is given for the technique employed.

Cramer, S.P. "Biochemical Application of X-ray Absorption Spectroscopy," in *X-ray Absorption: Principles, Applications, Techniques of EXAFS, SEXAFS, and XANES* ; Konigsberger, D.C., Prins, R., Eds., Wiley & Sons: New York, 1988.

Debus, R.J. *Biochim. Biophys. Acta* **1992** *1102*, 269-352.

Penner-Hahn, J.E. "Structural Properties of the Mn site in the Mn Catalases," in *Mn Redox Enzymes* ; Pecoraro, V.L., Ed., VCH Publishers: New York, 1992.

Stohr, J. *NEXAFS Spectroscopy* ; Gomer, R., Ed., Springer-Verlag: New York, 1992.

Thackeray, M.M.; David, W.F.; Bruce, P.G.; Goodenough, J.B. *Mat. Res. Bull.* **1983** *18*, 461-472.

Part I: Techniques

Chapter 1: The Hard X-ray Experiment

In x-ray absorption spectroscopy (XAS), photons of the appropriate energy can promote core level electrons to higher unoccupied levels or into the continuum. These transitions can be probed either directly, by monitoring the transmitted x-ray intensity, or indirectly, by collecting the Auger electrons or fluorescence resulting from electrons filling the core hole. Both of these secondary processes are proportional to the absorption process. The type of detection employed is determined by both the energy range and the type of sample.

K-edge transitions result when 1s electrons are excited to empty levels with p character or ejected from the atom. A typical K-edge absorption spectrum is shown in Figure 1.1. The spectrum consists of two distinct regions: the x-ray absorption near edge structure (XANES) and the extended x-ray absorption fine structure (EXAFS).

The XANES region is comprised of pre-edge and edge features and contains both electronic and some structural information. The pre-edge results from "forbidden" 1s to 3d dipole transitions which can arise from the overlap of p and d orbitals. The favorability of this mixing is symmetry-determined, allowing the extraction of local molecular structural information from the pre-edge features. $KMnO_4$, with tetrahedral symmetry, has a very prominate pre-edge peak, often referred to as a "white line" due to its sharpness. Compounds with more centro-symmetric geometries, such as MnF_2, have less opportunity for p-d orbital overlap and thus have relatively small pre-edge features. Other features which are sometimes observed have been assigned as 1s to 4s or $4p_z$ transitions. The inflection point of the edge

Figure 1.1: Mn K-edge absorption spectrum of $KMnO_4$. The spectrum consists of two distinct regions: the x-ray absorption near edge structure (XANES) and the extended x-ray absorption fine structure (EXAFS).

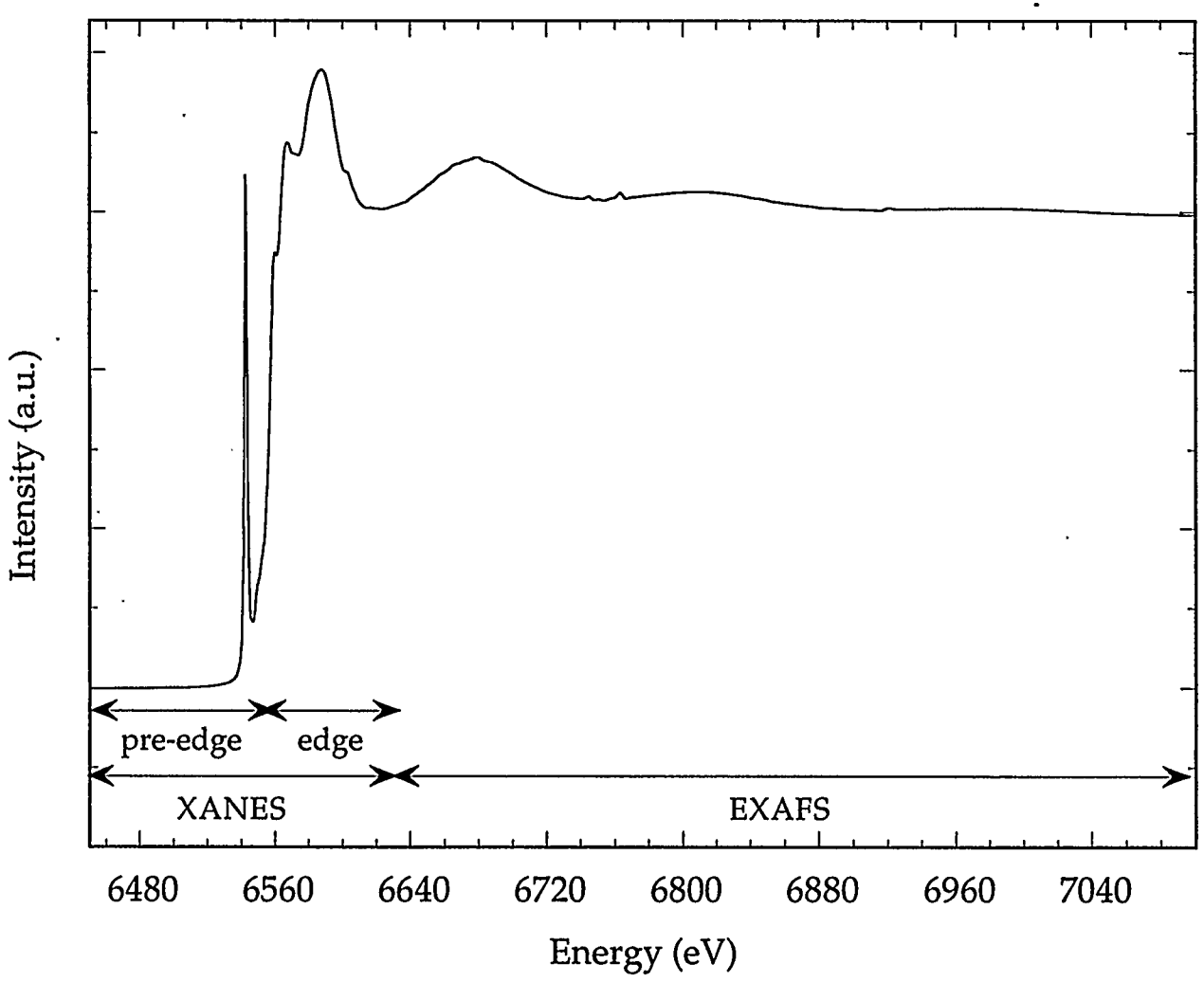
Intensity (a.u.)
pre-edge
edge
XANES
EXAFS
6480
6560
6640
6720
6800
6880
6960
7040
Energy (eV)

occurs at an energy that is characteristic of the electron density of the element being probed. The higher the oxidation state of the element and the more electron-withdrawing the ligands, the more energy it takes to ionize an electron from the central atom, resulting in a higher edge inflection energy. Typical energy shifts for homovalent Mn(II), Mn(III), and Mn(IV) model compounds are shown in Figure 1.2.

When the electrons receive sufficient energy, they can be ejected from the atom. The outgoing photoelectron waves are backscattered off of neighboring atoms, setting up an interference pattern which results in oscillations of the absorption coefficient (EXAFS). The equation describing this phenomenon can be written as:

$$\chi(k) = \sum_j N_j f_j(\pi,k) e^{-2k^2\sigma^2} e^{-2R_j/\lambda_j} \frac{sin[2kR_j + \Phi_{ij}(k)]}{kR_j^2} \qquad (1)$$

for K-edges and

$$\chi(k) = \sum_j N_j f_j(\pi,k) e^{-2k^2\sigma^2} e^{-2R_j/\lambda_j} \frac{sin[2kR_j + \Phi_{ij}(k) - \pi]}{kR_j^2} \qquad (2)$$

for L_{II} and L_{III} edges (transitions originating from the 2p level instead of the 1s, for a description of the L-edge transitions, see Chapter 2) where i is the absorbing atom, j is the backscattering atom, N_j is the number of backscatterers, $f_j(\pi,k)$ is the backscattering amplitude of the jth atom, R_j is the distance between the absorbing atom and the jth scatterer, σ_j^2 is the root mean square deviation of R_j, λ_j is the mean free path for inelastic scattering of the photoelectron, Φ_{ij} is the total phase shift for atoms i and j, and

Figure 1.2: Chemical Shifts of Mn(II), Mn(III), and Mn(IV) K-edge XANES. From left to right: $[L_2Mn(II)_2(\mu\text{-}OH)(\mu\text{-}CH_3CO_2)_2](PF_6)\cdot CH_3OH$ (dotted line); $[L_2Mn(III)_2(\mu\text{-}O)(\mu\text{-}CH_3CO_2)_2](ClO_4)_2$ (dotted and dashed line); $[L_2Mn(IV)_2(\mu\text{-}O)_2(\mu\text{-}O_2)](ClO_4)_2$ (solid line). L=N,N',N''-trimethyl-1,4,7-triazacyclononane.

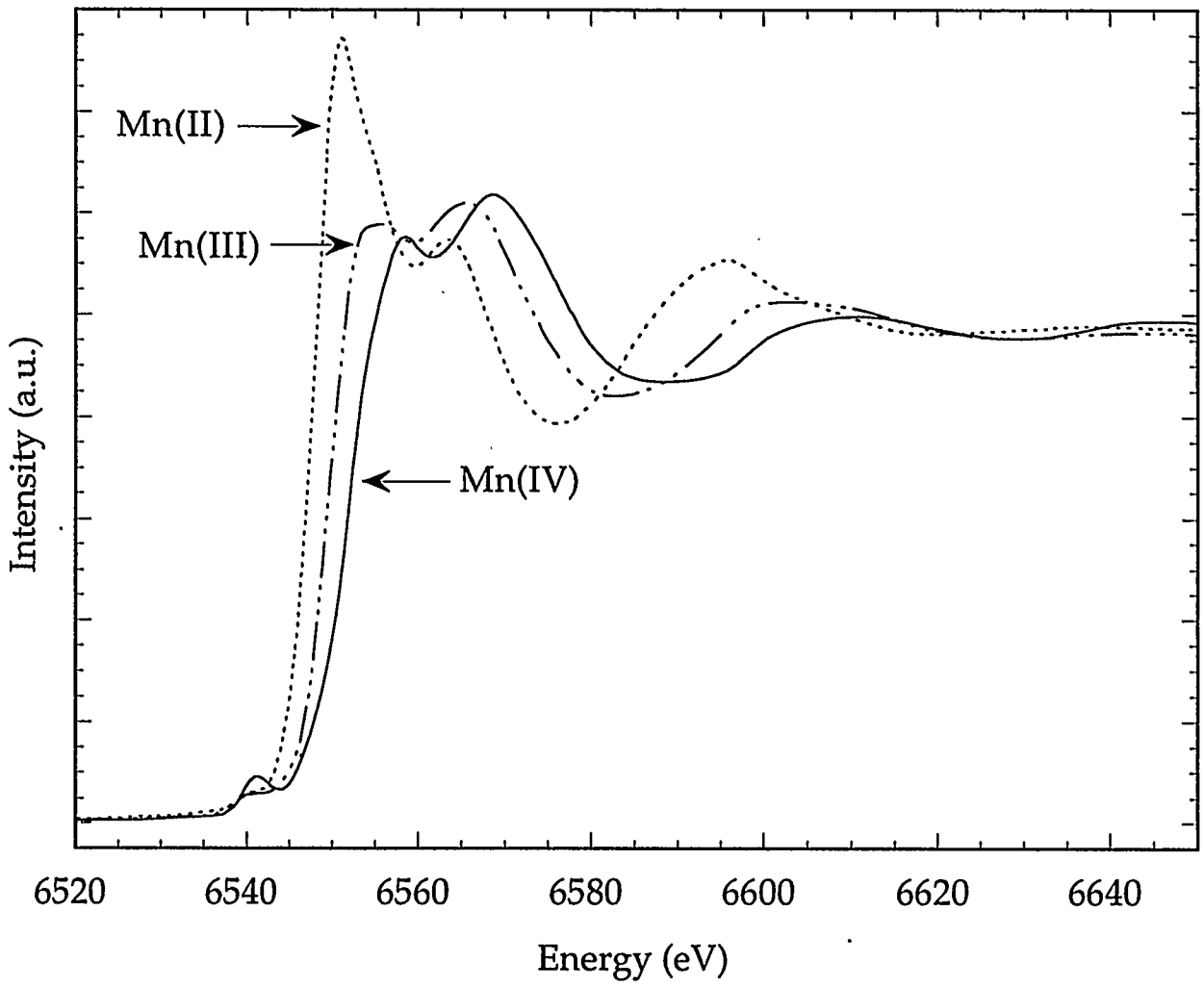
Mn(II)
Mn(III)
Mn(IV)
Intensity (a.u.)
6520
6540
6560
6580
6600
6620
6640
Energy (eV)

$$k = [(8\pi^2 m_e/h^2)(E - E_0)]^{1/2} \quad (3)$$

where m_e is the mass of the ejected electron, h is Planck's constant, E is the monochromator energy, and E_0 is the ionization potential of the absorbing element. For both K- and L-edges, the EXAFS oscillations can be fit with a series of damped sine waves generated either empirically or by *ab initio* calculations for individual absorber-backscatterer pairs. These simulations yield information on the number, atom type, and distance of backscattering atoms relative to the central atom (up to ~ 4 or 5 Å away). In practice, L-edge EXAFS is generally only employed for metals in the second transition row or beyond (with binding energy greater than 4 keV). This is due to the proximity of other edges in the 300 eV to 1 keV range where the first row transition metal L-edges occur and the need for a large data range for accurate simulations. The reader is referred to several review articles on XAS and references therein for more detailed discussions of XANES and EXAFS (Lee et al., 1981; Teo, 1986; Scott, 1984).

Data reduction of XANES spectra consists of first subtracting a linear background fit to the region before the edge. In transmission measurements, this background is due to the falloff of the absorption coefficients with increase in energy for all lighter elements present in the sample; for fluorescence measurements, it is determined by the shape of the detector window. The spectrum is normalized to unit intensity at the point where a line extrapolated through the EXAFS oscillations crosses the edge. For spectra without a sufficient data range for extrapolation, the XANES was normalized to unit intensity at the data point corresponding to the highest excitation energy.

The isolation of the EXAFS oscillations is illustrated in Figure 1.3. As in the data reduction of XANES spectra, a background fit to the pre-edge region is subtracted from the spectrum. It is also necessary to subtract a spline function fit to the data above the edge in order to eliminate the background which was not completely removed during the pre-edge subtraction. Dividing by the free atom fall-off leaves the EXAFS oscillations which are then converted from energy-space to *k*-space. An approximation to the free atom fall-off can be made using the Victoreen equation, a polynomial of the form $C\lambda^3 - D\lambda^4$. The coefficients (International Tables for X-ray Crystallography, 1968) for this function are specific for each absorption edge. The data is generally multiplied by k^3 to compensate for the dampening of oscillations at higher k due to both the k^{-1} dependence of the EXAFS and the $e^{-k^2\sigma^2}$ term in the EXAFS equation (see equations 1 and 2).

As a visual aid, the Fourier transform of the data can be taken and the expression describing the signal becomes a function of R instead of k:

$$f(R) = \int \chi(k) e^{-ikR} dk \qquad (4).$$

The data is then presented as a radial distribution of scatterers which surround the element being probed and can be "Fourier filtered" by back-transforming either the whole data range or specific peaks. The analysis procedure is simplified by first fitting individual peaks which correspond to fewer shells of backscattering atoms before undertaking the final analysis of the raw EXAFS data.

Figure 1.3: Isolation of EXAFS from the raw data. a) the raw data (dotted and dashed line), the pre-edge background (dotted line) subtracted from the raw data, and the data after subtraction (solid line); b) the data after pre-edge subtraction (dotted and dashed line), the spline function to be subtracted from the EXAFS region (solid line), and the Victoreen polynomial for Mn (dotted line); c) the isolated EXAFS; d) the k-weighted EXAFS (EXAFS multiplied by k^3); e) the Fourier Transform, phase-corrected for the oxygen backscatterer.

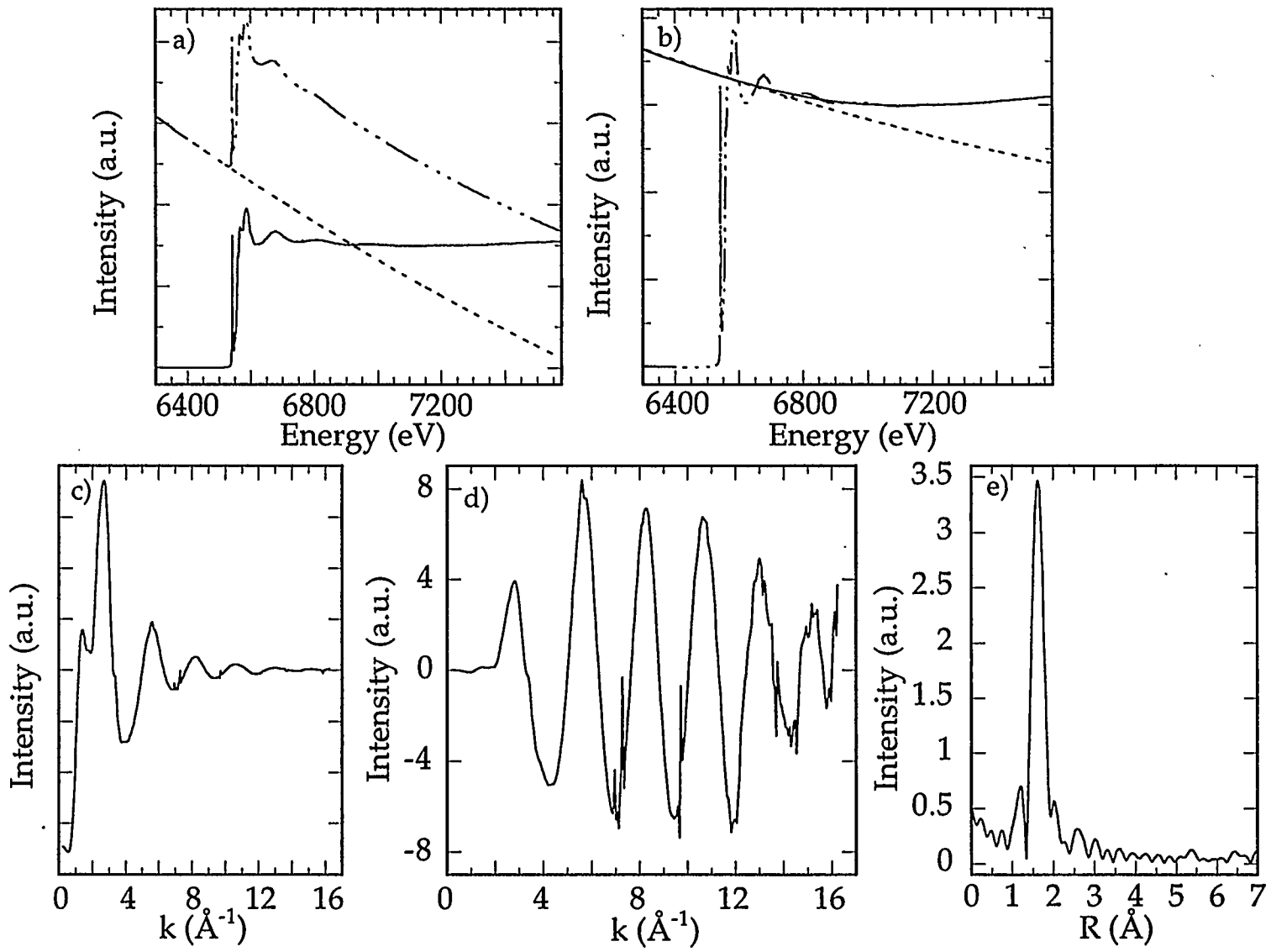
a)
b)
c)
d)
e)
Intensity (a.u.)
Energy (eV)
6400
6800
7200
k (Å^{-1})
R (Å)
0
4
8
12
16
-8
-4
0.5
1
1.5
2
2.5
3
3.5
5
6
7

Figure 1.4: The Effects of Varying Backscatterer N, R, and Z on the Mn EXAFS and Fourier Transforms. The EXAFS oscillations are shown on the left, the Fourier Transforms on the right have been phase corrected for the oxygen backscatterer. From top to bottom: a) 6 oxygen atoms at 2.0Å (solid line) and 2 oxygen atoms at 2.0Å (dotted line); b) 2 oxygen atoms at 3.0Å (solid line) and 2 oxygen atoms at 2.0Å (dotted line); c) 2 Mn atoms at 3.0Å (solid line) and 2 oxygen atoms at 3.0Å (dotted line).

Intensity (a.u.)
k (Å^{-1})
a)
b)
c)
Intensity (a.u.)
R (Å)
a)
b)
c)

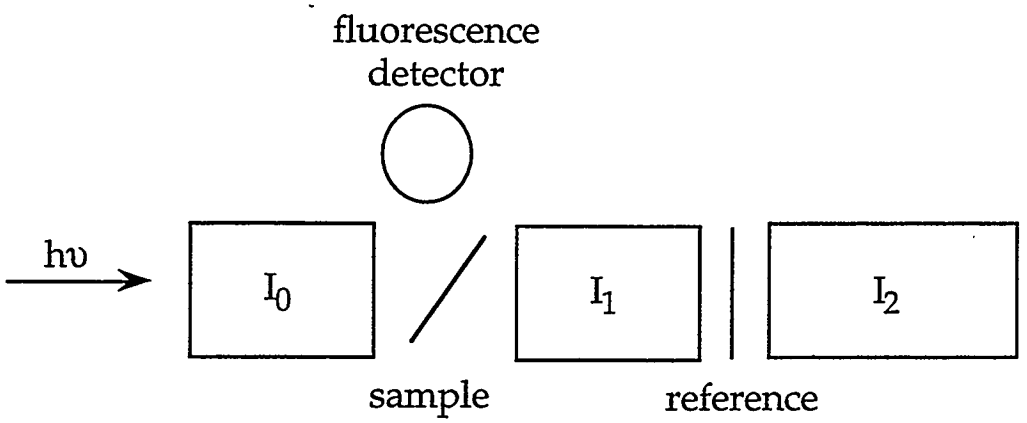

Figure 1.5: The EXAFS Experimental Set-up

The effects of varying coordination number, absorber-backscatterer distance, and backscatterer type on both the EXAFS oscillations and the Fourier transforms are shown in Figure 1.4.

Data isolation and analysis was performed using the data analysis package EXAFSPAK as obtained from the SSRL Biotechnology Group. Theoretical phase and amplitude functions as tabulated by McKale et al. (McKale et al., 1986) were used to simulate the EXAFS oscillations using a single scattering approximation.

The typical set-up of a transition metal EXAFS experiment is shown in Figure 1.5. The intensity of the incoming beam is monitored by an ion chamber, I_0. The absorption of the sample can be probed by fluorescence detection using a detector positioned at right angles to the incoming beam. The detector is placed in this position because, although the fluorescence is approximately isotropic, the elastic scatter for the polarized incident radiation is minimal in this configuration. As long as the sample is either spectroscopically thin or dilute and thick (Jaklevic et al., 1977), the fluorescence is directly proportional to the absorption process. Alternatively,

instead of monitoring the fluorescence, the intensity of the transmitted light can be measured by an ion chamber directly behind the sample, I_1. The transmission intensity is related to the absorption (A) by the following relationship:

$$A = log(I_0 / I_1) \qquad (5).$$

Care must be taken, however, to avoid inhomogeneities in the sample as even small flaws, such as slight differences in thickness over the sample area or pinholes in the sample cell, can affect the transmission intensity. A typical experiment includes simultaneous energy calibration of the beamline monochromator by placing a reference compound between the second (I_1) and third (I_2) ion chambers and monitoring the resulting transmission spectrum. Mn K-edge spectra were calibrated relative to either the first inflection point of a Mn foil (6539.00 eV) or the pre-edge feature of $KMnO_4$ (6543.33 eV). Tb L_{II} spectra were calibrated with respect to either the first inflection point of a Ni foil (8333.00 eV) or relative to each other. Ca K-edge spectra were not individually referenced and after the initial beamline calibration could only be calibrated relative to each other.

The choice of detection is largely dependent upon the type of sample to be characterized. For concentrated model compounds, either a transmission experiment, as described above, or a fluorescence experiment using a Lytle detector is performed. The Lytle detector is an ion chamber situated to collect a large solid angle of fluorescence from the sample. In order to eliminate background contributions, a "Z-1" filter is positioned between the Soller slits and the Lytle detector, where Z is the atomic number of the element being probed. "Z-1" filters can only absorb the fluorescence from elements with atomic numbers of at least Z, in addition to the elastic scatter. The Soller slits

help to eliminate the scatter by blocking photons not on a direct (90 degree) path from the sample to the detector. Fluorescence photons emitted from the filter cause gas molecules inside the chamber to ionize. A potential applied to two parallel metal plates inside the ion chamber produces an electric field which causes the ionized particles to flow to oppositely charged plates, creating a current. The current can be amplified using a low noise current amplifier and converted into digital pulses to be read by a computer. The choice of the gas inside the ion chamber determines the beam attenuation at a given energy. For ion chambers, nitrogen, which has an efficiency of 43% at 6.5 keV, was used except for severely flux-limited experiments where helium was used in I_0 (efficiency of 0.5% at 6.5 keV); for the Lytle detector, the chamber was filled with argon, which has an efficiency of 100% at 6.5 keV (Thompson, 1986).

Spectra of more dilute samples were measured with solid state fluorescence detectors, typically a 13 element Ge detector. Photons hitting the Ge can create multiple electron-hole pairs, each pair requiring 2.98 eV at 77K. An electric field across the face of the detector causes the differently charged particles to migrate in opposite directions resulting in a voltage pulse with height proportional to the number of electron-hole pairs produced. The signal is amplified by the preamplifier and then sent to the shaping amplifier for integration. A single channel analyzer (SCA) is set to accept a specific range of pulse heights. If the voltage pulse is within the window, a signal is sent to the hex scaler. The number of SCA signals is proportional to the fluorescence intensity. This pulse is then converted from analog to digital and recorded by the computer. Typical resolution of the detector is approximately 175 eV at 5.9 keV.

Model complexes used in the hard x-ray experiments were finely powdered and diluted to 10% (w/w) or less in the element of interest using BN or sucrose. They were then packed into ~1 mm thick metal plates sealed with Kapton tape. Spectra were measured below room temperature with an Oxford liquid helium cryostat operating at a temperature between 20 K and 25 K. $[L_2Mn_2(\mu\text{-}OH)(\mu\text{-}CH_3CO_2)_2](PF_6)\cdot CH_3OH$ (Bossek et al., 1989), $[L_2Mn_2(\mu\text{-}O)(\mu\text{-}CH_3CO_2)_2](ClO_4)_2$ (Wieghardt et al., 1985), and $[L_2Mn(IV)_2(\mu\text{-}O)_2(\mu\text{-}O_2)](ClO_4)_2$ (Bossek et al., 1990), where L=N,N',N''-trimethyl-1,4,7-triazacyclononane, were provided by K. Wieghardt. $KMnO_4$ was used as obtained from Aldrich Chemical Company.

Model compound spectra presented in this chapter were collected on Beamline X19A at the NSLS. Typically, XANES data were recorded using Si(220) monochromator crystals with the vertical entrance slits to the monochromator set at 1 mm or less. It is not necessary to have this precise of resolution when probing the EXAFS oscillations and therefore EXAFS spectra were usually collected with 2 mm slits. Si(111) crystals have a higher flux (and lower resolution) than the Si(220) crystals, however, the trade off is that at Mn K-edge energies there are generally more glitches in I_0 with the Si(111) monochromator. Additional diffraction planes at certain monochromator angles can give rise to a sudden drop in the beam intensity, a "glitch." Although dividing by I_0 should in theory account for any changes in the incident beam, these glitches often do not correctly ratio out, giving incongruous data points.

A limitation of K-edge XANES in the hard x-ray regime is the inherent resolution due to the lifetime of the 1s core hole. This can make it very difficult to quantitate the number of each type of a given element present in a sample. One solution to this problem is to measure the L-edges, gaining

resolution by the increase in the core hole lifetime (Chapter 2). Another method of quantitation involves recording the Kβ fluorescence spectra (Chapter 3).

One of the strengths of the EXAFS technique is that it is element-specific. However, when measuring the spectra of a mixture or compound containing different oxidation and/or spin states of a given element, it is only possible to probe the average state of that element with traditional XAS. To overcome this limitation, the technique of site-selective XAS has been developed (Chapter 3).

Bossek, U.; Wieghardt, K.; Nuber, B.; Weiss, J. *Inorg. Chim. Acta* **1989** *165*, 123-129.

Bossek, U.; Weyhermuller, T.; Wieghardt, K.; Nuber, B.; Weiss, J. *J. Am. Chem. Soc.* **1990** *112*, 6387-6388.

International Tables for X-ray Crystallography, vol. III; MacGillavry, C.H., Rieck, G.D., Eds., Kynoch: Birmingham, 1968, pp 171-173.

Jaklevic, J.; Kirby, J.A.; Klein, M.P.; Robertson, A.S. *Solid State Comm.* **1977** *23*, 679-682.

Lee, P.A.; Citrin, P.H.; Eisenberger, P.; Kincaid, B. *Rev. of Modern Physics* **1981** *53*, 769-806.

McKale, A.G.; Knapp, G.S.; Chan, S.-K. *Phys Rev. B* **1986**, *33*, 841-846.

Scott, R.A. "X-ray Absorption Spectroscopy" in *Structural and Resonance Techniques in Biological Research* ; Rousseau, D.L. , Ed., Academic Press: Orlando, 1984, pp 295-362.

Teo, B.K. *EXAFS: Basic Principles and Data Analysis* ; Springer-Verlag: Berlin, 1986.

Thompson, A.C. "X-ray Detectors," in *X-ray Data Booklet* ; Vaughan, D., Ed., Lawrence Berkeley Laboratory: Berkeley, 1986, pp 6.1-6.8.

Wieghardt, K.; Bossek, U.; Ventur, D.; Weiss, J. *J. Chem. Soc., Chem. Commun.* **1985** 347-349.

Chapter 2: The Soft X-ray Experiment

In L-edge x-ray excitation, photons of the appropriate energy can promote core level electrons to higher unoccupied levels. L_I edges arise from 2s to 3p transitions, L_{II} $2p_{1/2}$ to 3d, and L_{III} $2p_{3/2}$ to 3d, where the subscript 1/2 or 3/2 denotes the angular momentum, j. For first row transition metals, the final state of the L_{II} and L_{III} edges is the valence shell. This results in the L-edge technique being sensitive to both the metal oxidation state and the ligand environment.

It is generally advantageous to probe the XANES of L-edge transitions rather than K-edges (transitions from the 1s level to higher unoccupied shells with p character) due to the more distinctive features of the L-edges. L-edges are much lower in energy than the corresponding K-edge (Mn K-edge ~6540 eV; Mn L_{III} edge ~640 eV) and have a longer core hole lifetime. This results in a smaller linewidth over the Mn L-edge region and leads to more resolved features as compared to the K-edge 1s to 3d transition (Figure 2.1). This decrease in linewidth more than compensates for the smaller energy shift with increasing oxidation state of Mn L-edges as compared to K-edges. Table 2.1 compares the energy shift to lifetime broadening (Nyholm et al., 1981) ratio for Mn K, L_{II}, and L_{III} edges. The energy shift is an average of that measured for Mn(II) to Mn(III) and Mn(III) to Mn(IV) transitions.

At the energies corresponding to the L-edges of first row transition metal complexes (400 to 1200 eV), air absorbs significantly (nitrogen K-edge ~410 eV, oxygen K-edge ~543 eV). This makes it necessary for the entire sample apparatus to be under ultra high vacuum (UHV $<4.5 \times 10^{-9}$ torr). A schematic of the UHV chamber is shown in Figure 2.2. The x-ray beam intensity (I_0) is monitored by recording the current produced when the beam

Figure 2.1: The Improved Resolution of Mn L-edge Spectra Versus the Corresponding K-edge. Top to bottom: the L_{III} edge of MnF_2; the 1s to 3d pre-edge feature from the K-edge of MnF_2.

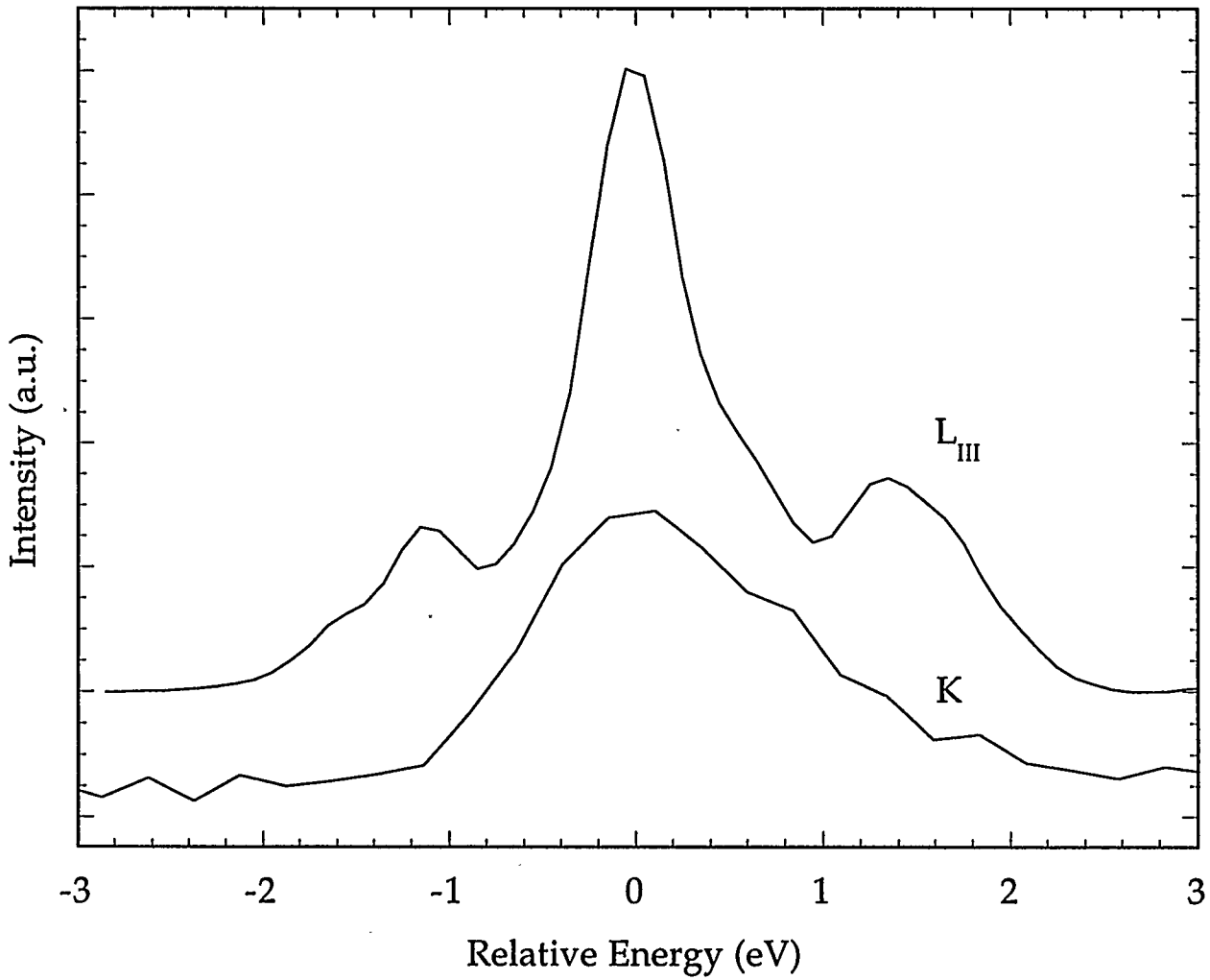
Intensity (a.u.)
L III
K
-3
-2
-1
0
1
2
3
Relative Energy (eV)

Table 2.1: A Comparison of Energy Shift per Oxidation State Change with Lifetime Broadening for Mn K, L_{II}, and L_{III} edges.

	Lifetime Broadening	Energy Shift	Shift/Broadening
K	1.16 eV	2.4 eV	2.0
L_{II}	0.34	1.2	3.5
L_{III}	0.20	1.7	8.5

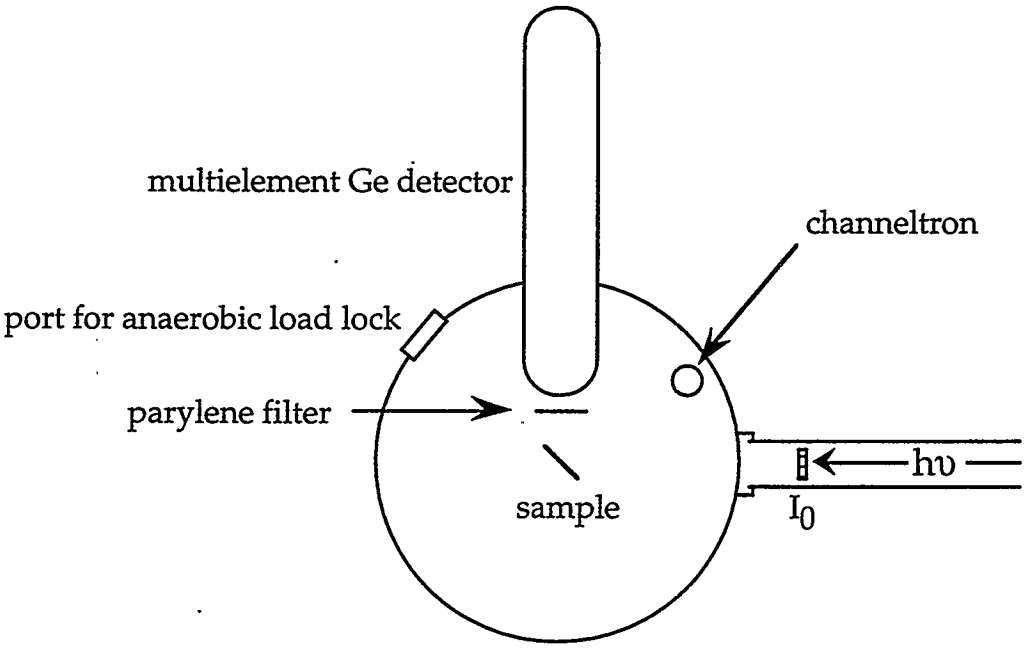

Figure 2.2: A schematic of the L-edge Experimental Set-up (top view).

passes through a fine gold mesh. There is room in the chamber for the sample, cryostat, both electron yield and fluorescence detectors, ion gauges, and an anaerobic sample load lock system.

Mn L-edge spectra of model compounds are most readily probed by electron yield. A Galileo 4716 channeltron electron multiplier mounted perpendicular to the sample counted the total electron yield as a result of the absorption process. Each electron hitting the SiO_2 face of the channeltron produces more electrons, causing a cascade effect. The electrons hitting the high voltage biased back plate are multiplied to create a current which can then be measured. These spectra were taken on Beamlines U4B (Chen et al., 1989) and X1B (Randall et al., 1992) at the NSLS, and on Beamline 10-1 (Karpenko et al., 1989) at SSRL. Beamline slits were set at 15 microns or less, resulting in a beamline resolution of better than 0.16 eV.

L-edge spectra of the following Mn model compounds are presented here. $Mn_6O_2(O_2CPh)_{10}(py)_2(MeCN)_2$ (Baskin et al., 1988) and $Mn_4O_3Cl(O_2CMe)_3(dbm)_3$ (Hendrickson et al., 1992) were synthesized by S. Wang, $Mn_2O_2(O_2CMe)Cl_2(bpy)_2$ (Schake et al., 1989) by M.W. Wemple, $Mn_3(O_2CPh)_2(biphen)_3(bpy)_3$ (Christou et al., 1989) by A.R. Schake, and $NBu_4[Mn_4O_2(O_2CMe)_7(pic)_2]$ (Libby et al., 1991) by E. Libby in the G. Christou laboratory. A. Gelasco in the V.L. Pecoraro laboratory prepared $[Mn_4(2\text{-}OHpicpn)_4](ClO_4)_4$ (Gelasco et al., 1995) and S. Gorun synthesized $[Ba_8Na_2ClMn_{16}(OH)_8(CO_3)_4L_8]\cdot 53H_2O$, or "$Mn_{16}$", where L=1,3-diamino-2-hydroxy-propane-N,N,N',N'-tetraacetic acid (Gorun et al., 1991a; Gorun et al., 1991b). MnF_2, $MnSO_4$, and MnO_2 were used as obtained from Aldrich Chemical Company.

Finely powdered samples were affixed to Cu sample holders with the aid of Scotch double sided sticky tape which was free of adventitious Mn. The

sample holders were then mounted on the cold finger at an angle of 45° to the incident beam. Air sensitive samples were prepared in either a N_2 glove box or a glove bag filled with Ar and anaerobically loaded into the chamber via a load lock system. Model compound spectra presented here are typically the sum of 2-3 scans, representing less than an hour of data collection.

The isolation of L-edge spectra consists of calibration, background removal, and normalization steps. Mn L-edge spectra were calibrated relative to the L_{III} edge of MnF_2 which was assigned an energy of 640.0 eV. Due to the closeness of the oxygen K-edge (~543 eV) to the Mn L-edge (640 eV) and to varying amounts of water adsorbed onto the sample surface, it was not possible to consistently measure the overall Mn L-edge jump. To allow comparison of different Mn spectra, backgrounds were generated by using a combination of separate linear fits underneath the L_{III} and L_{II} regions of the data and then subtracted from the spectra (Figure 2.3). The height of the L_{II} peak was normalized to unit intensity. A more rigorous procedure would normalize to the area under the L_{II} peak, however, for the applications described here, this simplified method was adequate.

The shape and position of the Mn L-edges vary dramatically with oxidation state, as is shown in Figure 2.4. The L_{II} and L_{III} edges are due to electronic transitions to the 3d levels from the $2p_{1/2}$ and $2p_{3/2}$ levels, respectively. The additional complex features result from 2p-3d and 3d-3d Coulomb and exchange interactions, as well as crystal field effects (deGroot et al., 1990). High spin Mn(II), as illustrated by $MnSO_4$, exhibits a sharp peak near 640 eV with lesser peaks on both sides of the main L_{III} transition and a smaller L_{II} edge ~11 eV higher. Mn(III) and Mn(IV) have broader L-edge features which occur at higher energy than Mn(II), as shown for $[Mn(III)_4O_2(O_2CMe)_7(pic)_2]$ and $Mn(IV)O_2$.

Figure 2.3: L-edge Background Removal. From top to bottom: a) Mn L-edge raw data of $Mn_2O_2(O_2CMe)Cl_2(bpy)_2$ (solid line), line 1 (dashed line), line 2 (dotted and dashed line); b) Mn L-edge raw data of $Mn_2O_2(O_2CMe)Cl_2(bpy)_2$ (dotted and dashed line), background (solid line); c) Mn L-edge spectrum of $Mn_2O_2(O_2CMe)Cl_2(bpy)_2$ after background subtraction (solid line).

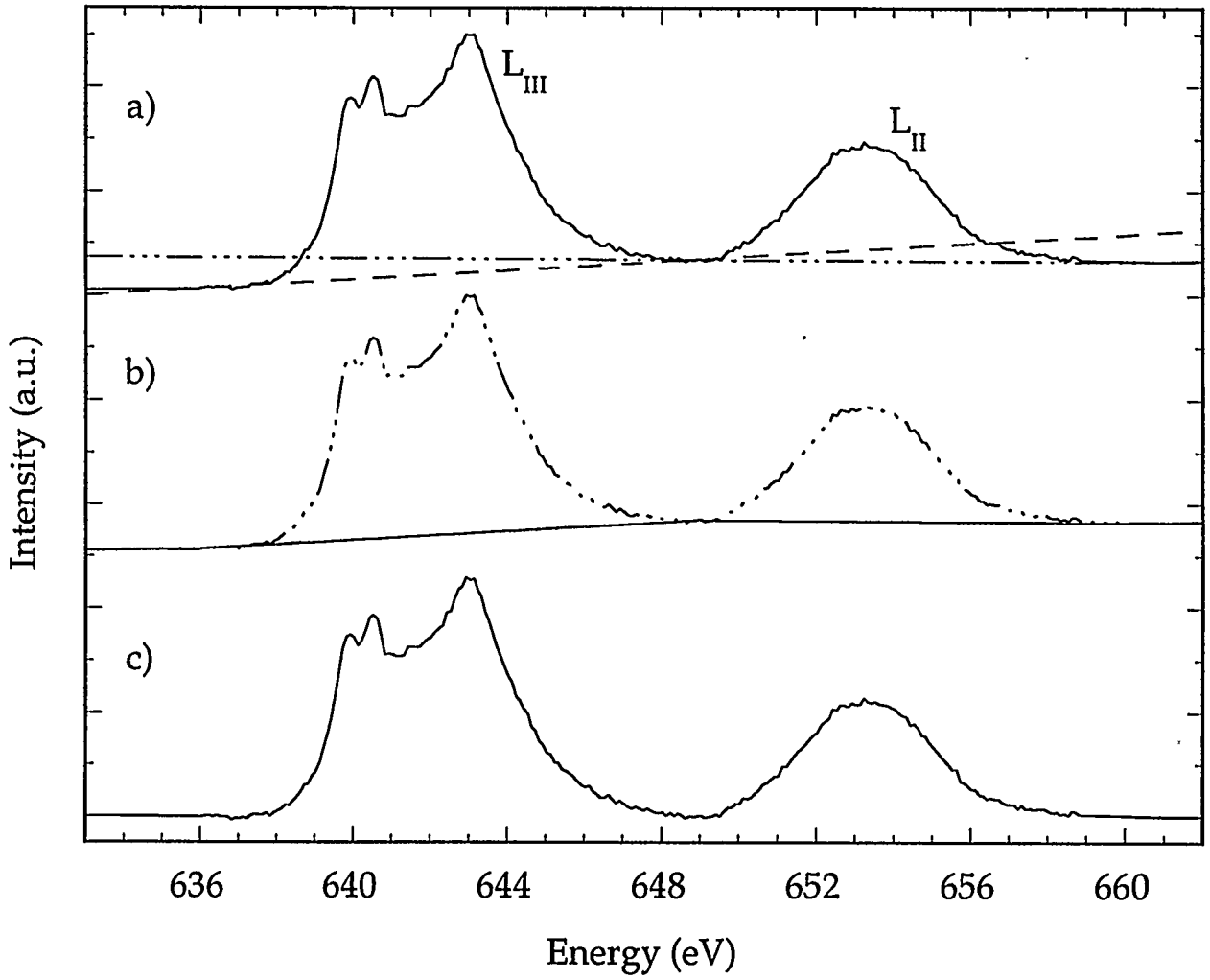
a)
b)
c)
L_{III}
L_{II}
Intensity (a.u.)
636
640
644
648
652
656
660
Energy (eV)

Figure 2.4: Chemical Shifts of Manganese L-edge Spectra. From left to right: $Mn(II)SO_4$ (dotted line), $NBu_4[Mn(III)_4O_2(O_2CMe)_7(pic)_2]$ (solid line), and $Mn(IV)O_2$ (dotted and dashed line).

Intensity (a.u.)
Energy (eV)
636
640
644
648
652
656
660
L_{III}
L_{II}
Mn(II)
Mn(III)
Mn(IV)

Atomic Multiplet Calculations

Atomic multiplet calculations similar to those developed by van der Laan and Kirkman (van der Laan et al., 1992) were used to simulate Mn(II) spectra. These simulations assume transitions between a $2p^63d^5$ ground state and a $2p^53d^6$ excited state, with the electron localized on the Mn. Racah and RCN parameters were used as tabulated (van der Laan et al., 1992), and the Slater integrals were set at 80% of the atomic values. The individual transitions were broadened with Lorentzians of 0.1 eV and 0.3 eV around the L_{III} and L_{II} regions, respectively, to compensate for the inherent linewidth due to the lifetime of the final state. The beamline resolution was accounted for by convoluting the spectrum with a 0.15 eV Gaussian. The features of $MnSO_4$ were reproduced by atomic multiplet calculations (Figure 2.5). In general, as the ligand field strength increases, the peaks in the wings split further away from the central line (Cramer et al., 1991).

Because charge transfer and covalency become more important for Mn(III) and Mn(IV), simple ligand field multiplet calculations for these oxidation states are less successful. More sophisticated procedures have been developed to account for charge transfer (deGroot et al., 1994 and Kawai et al., 1990) but have yet to be satisfactorily applied to Mn(III) and Mn(IV).

Empirical Mixed Valence Simulations

For the analytical interpretation of spectra which contain a mixture of oxidation states, it is not always necessary or practical to use theoretical simulations. Instead, an empirical approach to the spectral analysis of manganese mixed valence complexes has been taken. This method assumes almost no interaction between Mn sites, and relies on models with similar ligand fields. To fit a mixed valence spectrum, these simulations optimize

Figure 2.5: Atomic Multiplet Simulation of $Mn(II)SO_4$. Experimental data (dotted line), theoretical calculation (sticks), and smoothed theoretical spectrum (solid line).

Intensity (a.u.)
636
640
644
648
652
656
660
Energy (eV)

the relative weights of homovalent experimental spectra, also allowing for small energy shifts. As described above, it was not possible to normalize the overall edge jump to unit Mn. The arbitrary normalization procedure made it necessary to calibrate the actual ratio of Mn oxidation states in the sample versus the fractions of normalized Mn single oxidation state spectra required in the experimental simulations for a range of characterized mixed valence complexes.

For simulations of $Mn(II)_x(III)_y$ spectra, a combination of $Mn(II)SO_4$ and $NBu_4[Mn(III)_4O_2(O_2CMe)_7(pic)_2]$ spectra were used as homovalent standards. The results from a series of fits are presented in Figure 2.6 and Table 2.2. As an example, the spectrum of the trinuclear mixed valence complex, $Mn(II)Mn(III)_2(O_2CPh)(biphen)_3(bpy)_3$, is nicely simulated by a sum of $Mn(II)SO_4$ and $NBu_4[Mn(III)_4O_2(O_2CMe)_7(pic)_2]$ spectra. All of the main peaks are reproduced, as well as the ratio of L_{III} to L_{II} intensity. There is slight discrepancy in the 641-642 eV range where the overall peak for the Mn(III) component is expected. The Mn(III) L_{III} peak is often sensitive to the nature of the axial ligand in Jahn-Teller distorted complexes. A more elaborate simulation procedure would use a range of models with different ligand field parameters (10 Dq, Ds, etc.), but for the present application the fit is more than adequate.

Although the component peak energies were allowed to vary in the simulation algorithm, for the $Mn(II)_x(III)_y$ simulations they varied very little. This is consistent with trapped valence Mn species with little delocalization across metal centers, similar to results with most oxygen-bridged dinuclear iron complexes (Peng et al., 1995). In contrast, in the fully delocalized $[Fe_2(Me_3tacn)_2(\mu\text{-}OH)_3][BPh_4]_2$ complex, the individual Fe(II) and Fe(III) peak positions move on the order of 0.6 eV closer together compared to isolated

Figure 2.6: Simulations of Mn_2(II/III) Model Compounds. Left (top to bottom): a) $Mn_6O_2(O_2Ph_{10})(py)_2(MeCN)_2$ (solid line) and mixed valence simulation (dotted line); b) Mn(II) component (dotted line) and Mn(III) component (solid line) of simulation for $Mn_6O_2(O_2Ph_{10})(py)_2(MeCN)_2$; c) $Mn_3(O_2CPh)_2(biphen)_3(bpy)_2$ (solid line) and simulation (dotted line). Right: Fraction of Mn(II) to total Mn in best fit versus actual ratio of Mn(II) to total Mn in model compound. The horizontal bar corresponds to the ratio of Mn(II) to total Mn found for "Mn_{16}" using the empirical simulations. Linear regression: $y = -0.0052005 + 0.9256 \times x$, $r^2 = 0.999$.

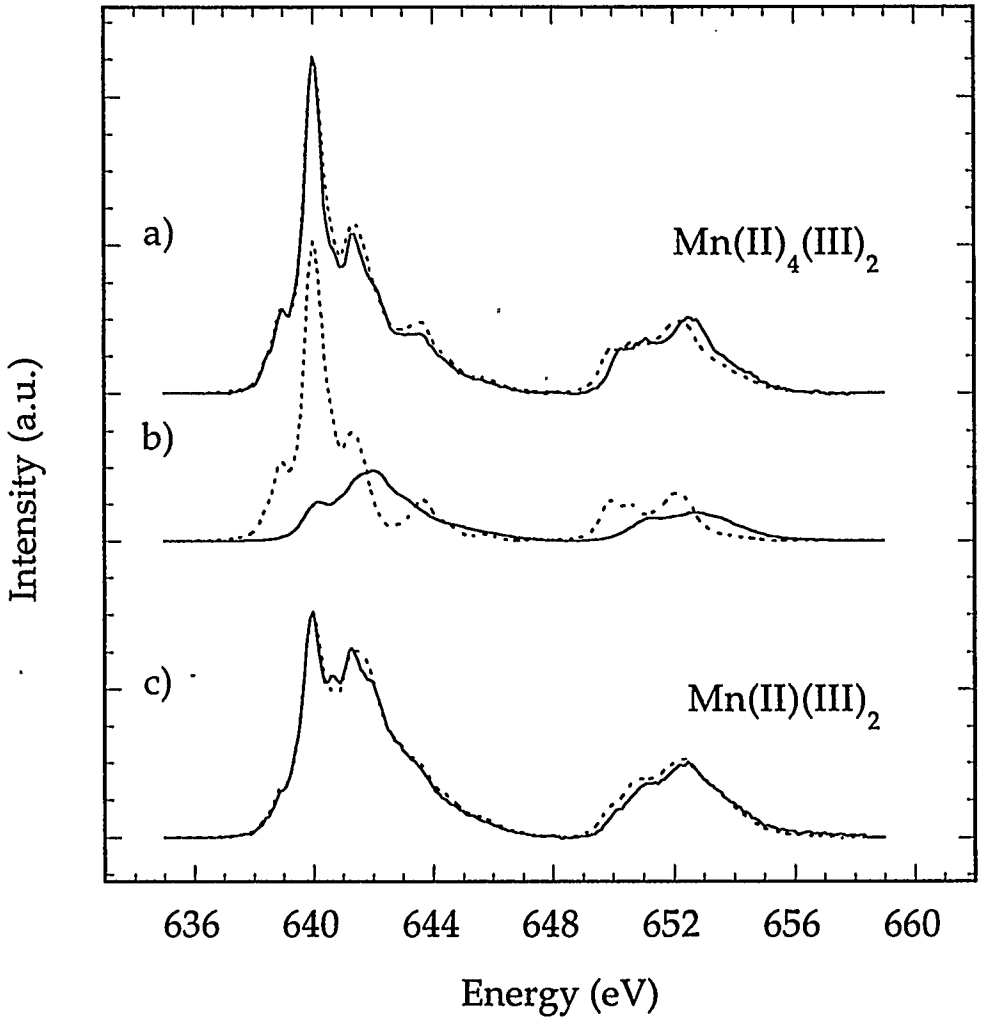
a)
Mn(II)$_4$(III)$_2$
b)
c)
Mn(II)(III)$_2$
Intensity (a.u.)
636
640
644
648
652
656
660
Energy (eV)

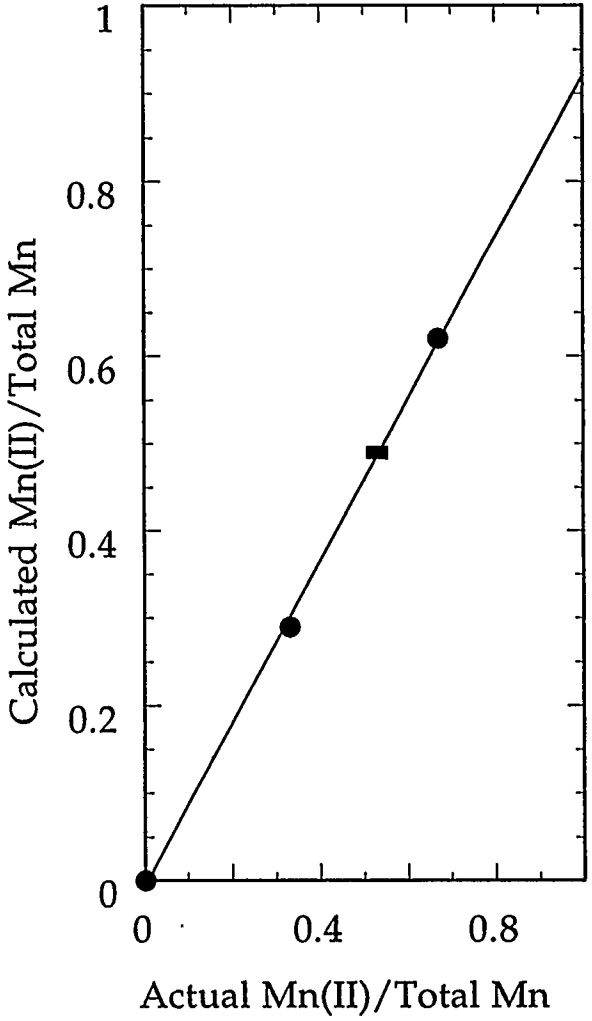
1
0.8
0.6
0.4
0.2
0
0
0.4
0.8
Calculated Mn(II)/Total Mn
Actual Mn(II)/Total Mn

Table 2.2: Mixed-Valent Simulation Fitting Parameters for $Mn(II)_x(III)_y$ compounds.

Model Compound	Oxidation States	Fit Fraction	Energy Shift
$Mn_3(O_2CPh)_2(biphen)_3(bpy)_3$	$(II)(III)_2$	0.29 Mn(II)/total Mn	-0.09 eV(2+) -0.10 eV(3+)
$Mn_6O_2(O_2CPh)_{10}(py)_2(MeCN)_2$	$(II)_4(III)_2$	0.62 Mn(II)/total Mn	-0.06 eV(2+) +0.14 eV(3+)
$[Ba_8Na_2ClMn_{16}(OH)_8(CO_3)_4L_8]$	$(II)_{8.5}(III)_{7.5}$	0.49 Mn(II)/total Mn	+0.01 eV(2+) +0.02 eV(3+)

Fe(II) and Fe(III) spectra and coalesce into a single broad profile (Peng et al., 1995).

The fractional ratios of monovalent Mn(II) to Mn(III) needed in the best fit slightly underestimate the actual ratios as arbitrarily normalizing the height of the L_{II} edge to unity does not take into account the decrease in branching ratio (L_{III} intensity / total line strength) with increase in oxidation state of Mn. It was therefore necessary to calibrate the spectral ratio by finding the best scale factor using a linear regression (Figure 2.6). The origin was included in the linear regression of the data as simulations on trivalent manganese did yield a value of zero for the Mn(II) component. A high level of correlation was achieved in these fits which mimic the shape of the experimental spectra well. Taking into account the scatter in the data, it

should be possible to determine the Mn(II) fit fraction in an unknown $Mn(II)_x(III)_y$ compound to within ± 0.01 of the actual value.

This algorithm was used to determine the oxidation state composition of the mixed valence compound, $[Ba_8Na_2ClMn_{16}(OH)_8(CO_3)_4L_8]\cdot 53H_2O$, L=1,3-diamino-2-hydroxy-propane-N,N,N',N'-tetraacetic acid, "Mn_{16}". This complex is the largest structurally characterized polynuclear Mn aggregate to date and consists of pentagonal bipyramidal Mn(II) sites and octahedral Mn(III) sites. The best simulation had a spectral ratio of 0.49 ± 0.01 Mn(II)/total Mn which corresponds to a ratio of 8.5 ± 0.2 Mn(II) to 7.5 ± 0.2 Mn(III). The energy shifts were negligible, being + 0.01 eV and + 0.02 eV for the Mn(II) and Mn(III) components, respectively, indicating little delocalization between the metal centers. Both single crystal x-ray diffraction measurements and elemental analysis of "Mn_{16}" support a ratio of approximately 9:7 (Gorun et al., 1991c). Mn coordination geometries in closely related Mn complexes, as determined via x-ray and neutron diffraction, also support these oxidation state assignments (Schulz et al., 1994). Figure 2.7 presents the best fit to the data, and also compares simulations with Mn(II) to Mn(III) ratios of 10:6, 9:7, 8:8, and 7:9 to the data.

This technique was also applied to mixed valence $Mn(III)_a(IV)_b$ spectra. The results of fitting with $NBu_4[Mn(III)_4O_2(O_2CMe)_7(pic)_2]$ and $Mn(IV)O_2$ are shown in Figure 2.8 and tabulated in Table 2.3. For example, the spectrum of the dinuclear mixed valence complex, $Mn(III)Mn(IV)O_2(OAc)Cl_2(bpy)_2$, was simulated by a sum of $NBu_4[Mn(III)_4O_2(O_2CMe)_7(pic)_2]$ and $Mn(IV)O_2$ spectra. Both the general shape of the spectrum and the ratio of L_{III} to L_{II} intensity are reproduced in the simulations. However, there is some discrepancy on both sides of the L_{III} peak, and also in the L_{II} region. These differences could arise because the homovalent standards have broad features which cannot

Figure 2.7: Simulations of $[Ba_8Na_2ClMn_{16}(OH)_8(CO_3)_4L_8]*53H_2O$, L=1,3-diamino-2-hydroxy-propane-N,N,N',N'-tetraacetic acid. Top to bottom: "Mn_{16}" (solid line) and simulation with a Mn(II)/Mn(III) ratio of 10:6 (dotted line); "Mn_{16}" (solid line) and simulation with a Mn(II)/Mn(III) ratio of 9:7 (dotted line); "Mn_{16}" (solid line) and best fit simulation with a Mn(II)/Mn(III) ratio of 8.5:7.5 (dotted line); "Mn_{16}" (solid line) and simulation with a Mn(II)/Mn(III) ratio of 8:8 (dotted line); and "Mn_{16}" (solid line) and simulation with a Mn(II)/Mn(III) ratio of 7:9 (dotted line).

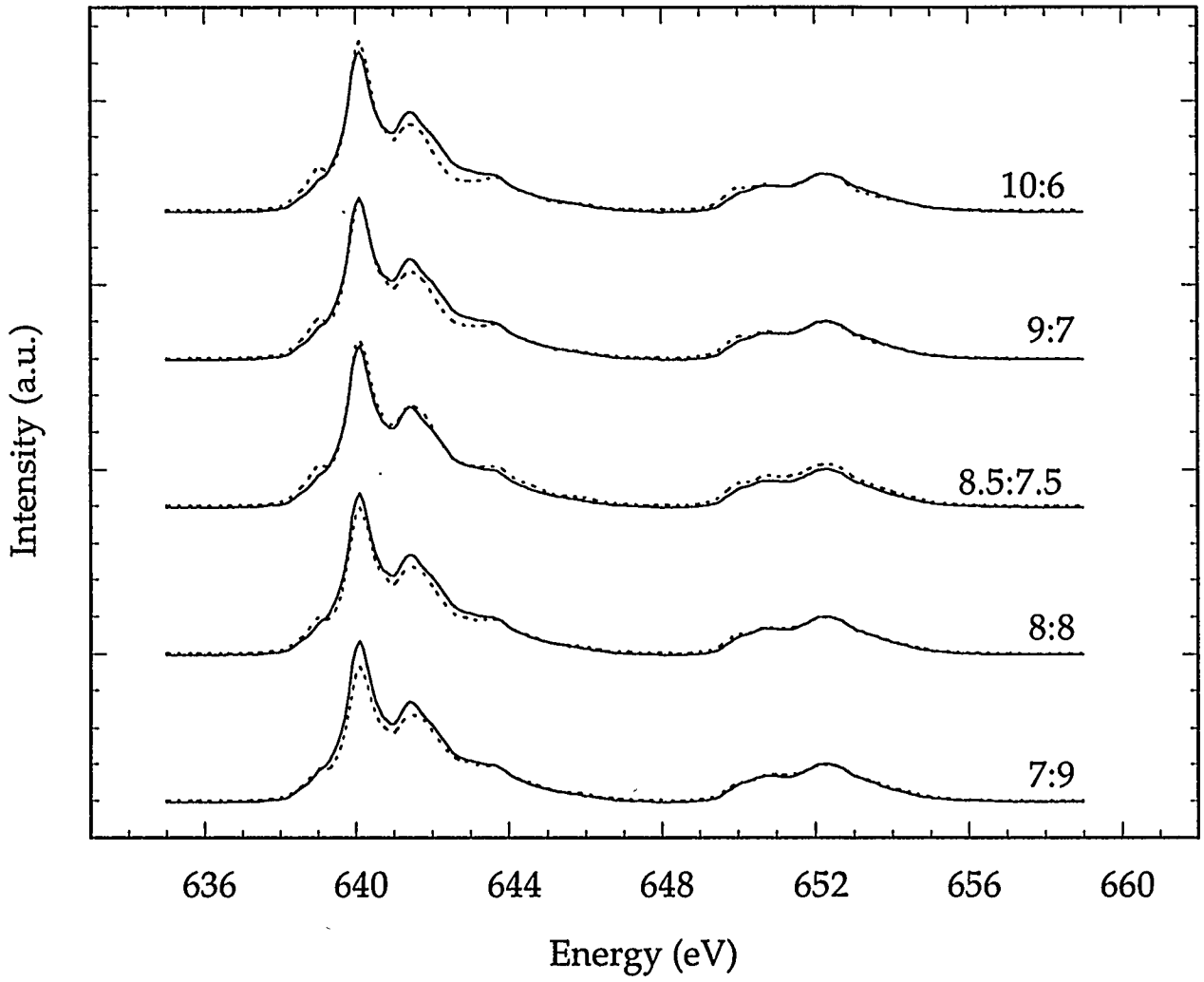
10:6
9:7
8.5:7.5
8:8
7:9
Intensity (a.u.)
636
640
644
648
652
656
660
Energy (eV)

Figure 2.8: Simulations of Mn_2(III/IV) Model Compounds. Left top to bottom: a) $Mn_2O_2(OAc)Cl_2(bpy)_2$ (solid line) and simulation (dotted line); b) Mn(III) component (solid line) and Mn(IV) component (dotted line) of simulation for $Mn_2O_2(OAc)Cl_2(bpy)_2$; c) $Mn_4O_3Cl(OAc)_3(dbm)_3$ (solid line) and simulation (dotted line). Right: Fraction of Mn(III) to total Mn in best fit versus actual ratio of Mn(III) to total Mn in model compound. Linear regression: $y = -0.0078571 + 0.84286 \times x$, $r^2 = 0.996$.

Intensity (a.u.)
a)
b)
c)
$Mn_2(III)(IV)$
$Mn_4(III)_3(IV)$
636
640
644
648
652
656
660
Energy (eV)
Calculated Mn(III) / Total Mn
0
0.2
0.4
0.6
0.8
1
0
0.4
0.8
Actual Mn(III)/Total Mn

Table 2.3: Mixed-Valent Simulation Fitting Parameters for $Mn(III)_a(IV)_b$ compounds.

Model Compound	Oxidation States	Fit Fraction	Energy Shift
$Mn_2O_2(O_2CMe)Cl_2(bpy)_2$	(III)(IV)	0.39 Mn(III)/total Mn	-0.04 eV(3+) -0.08 eV(4+)
$Mn_4O_3Cl(OAc)_3(dbm)_3$	$(III)_3(IV)$	0.64 Mn(III)/total Mn	-0.01 eV(3+) + 0.25 eV(4+)

reproduce all of the mixed valence structure. There may also be some delocalization between the metal centers. However, since the magnitudes of the energy shifts are less than 0.1 eV, these clusters are not highly delocalized. One exception is the energy shift for the Mn(IV) component of the $Mn_4O_3Cl(O_2CMe)_3(dbm)_3$ simulation which is 0.25 eV. As this shift is positive, it is more likely to be the effect of metal to ligand charge transfer rather than metal-metal delocalization. The ratios obtained from the $Mn(III)_a(IV)_b$ simulations are less than the actual numbers, again resulting from the normalization procedure. The origin was included in the linear regression and a good correlation observed. The scatter in this data corresponds to an uncertainty of ± 0.02 in determining the Mn(III) fit fraction for an unknown $Mn(III)_a(IV)_b$ compound.

The Mn/O Problem

Applying this technique to dilute metalloproteins requires the energy discrimination and sensitivity of a windowless solid state detector, such as the 13 element Ge detector. A major difficulty in measuring Mn L-edge protein

spectra is the predominance of oxygen K_α fluorescence from the sample. Oxygen K_α fluorescence (525 eV) and manganese L_α fluorescence (637 eV) are unresolvable using a windowless Ge detector which has resolution on the order of 140 eV at 600 eV. As the absorption cross section of carbon above its K-edge (284 eV) decreases with increasing energy, a Parylene ($-C_8H_8-$) filter placed between the sample and the detector eliminates predominately oxygen fluorescence, at the expense of total flux, and allows the detection of Mn fluorescence.

The effect of a one micron filter on the fluorescence spectrum of MnO as collected by a 13 element windowless Ge detector is illustrated in Figure 2.9. The Mn fluorescence is virtually undetectable without the filter. Although the filter reduces the overall intensity to ~2 % of the original signal, it also allows the detection of the Mn fluorescence. For Mn proteins which, ignoring the water solvent, contain ~23 % O and on the order of 0.1 to 0.3 %Mn, the predominance of oxygen fluorescence is much worse than in the case of MnO. In order to use Mn L-edge spectroscopy to characterize the electronic structure of metalloproteins, 2 or 4 micron Parylene filters were necessary.

The L-edge technique can be a powerful probe of the symmetry, ligand field, and oxidation state composition of an unknown Mn cluster. By using Parylene filters to selectively pass manganese fluorescence, this should become a useful technique for studying Mn metalloproteins (Chapters 4 and 5).

Figure 2.9: The Reduction of Oxygen Fluorescence from a Sample of MnO using a Parylene Filter. The Mn fluorescence (solid line) obtained using the filter has been multiplied by a factor of 30 for easier comparison to the predominately O fluorescence spectrum observed without the filter (dotted line).

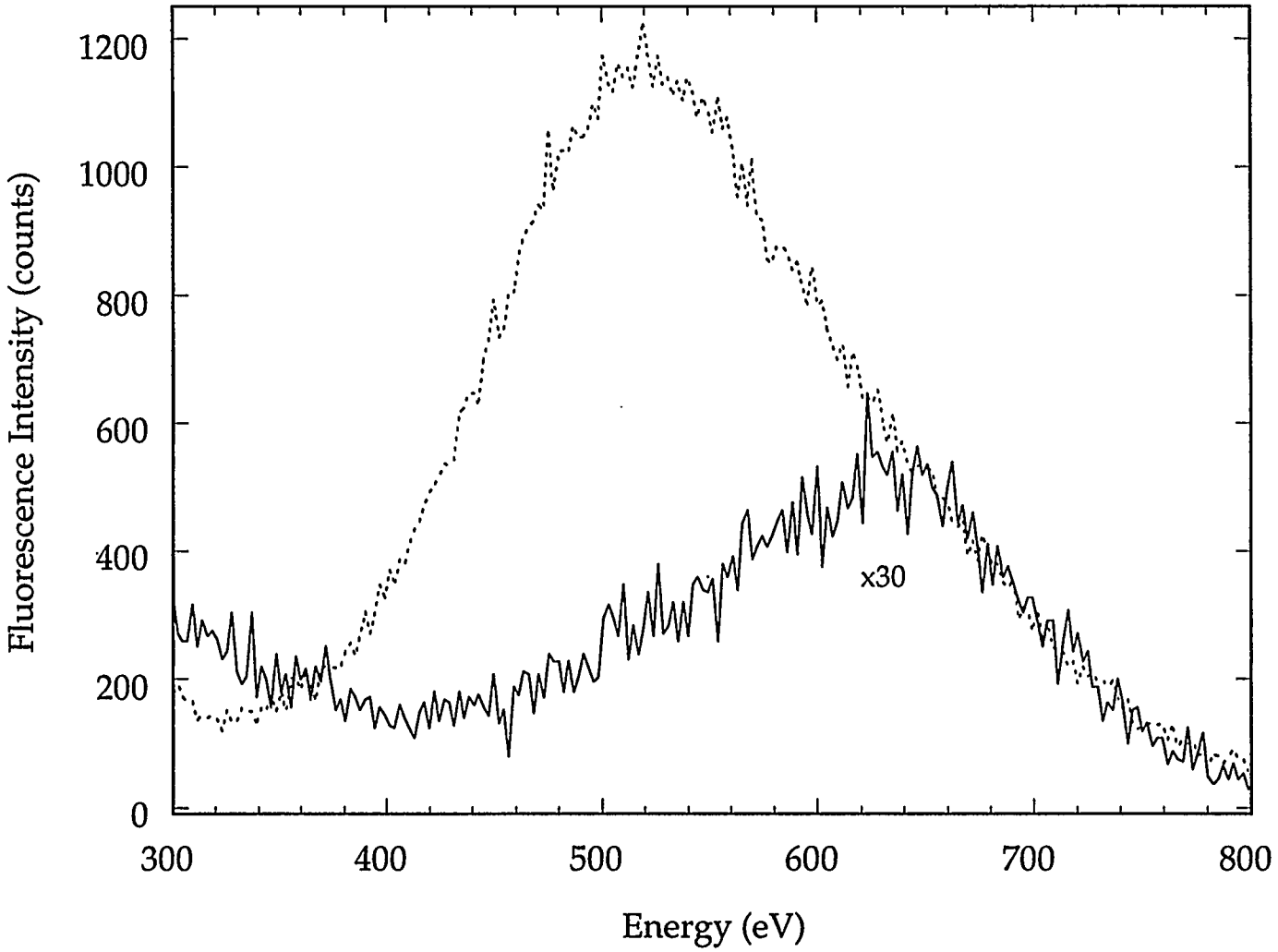
Fluorescence Intensity (counts)
1200
1000
800
600
400
200
0
300
400
500
600
700
800
Energy (eV)
x30

Bashkin, J.S.; Schake, A.R.; Vincent, J.B.; Chang, H.R.; Li, Q.; Huffman, J.C.; Christou, G.; Hendrickson, D.N. *J. Chem. Soc., Chem. Comm.* **1988**, 700-702.

Chen, C.T.; Sette, F. *Rev. Sci. Instr.* **1989**, *60*, 1616-1621.

Christou, G. *Acc. Chem. Res.* **1989**, *22*, 328-335.

Cramer, S.P.; deGroot, F.M.F.; Ma, Y.; Chen, C.T.; Sette, F.; Kipke, C.A.; Eichhorn, D.M.; Chan, M.K.; Armstrong, W.H.; Libby, E.; Christou, G.; Brooker, S.; McKee, V.; Mullins, O.C.; Fuggle, J.C. *J. Am. Chem. Soc.* **1991**, *113*, 7937-7940.

deGroot, F.M.F.; Fuggle, J.C.; Thole, B.T.; Sawatzky, G.A. *Phys. Rev. B* **1990**, *42*, 5259-5468.

deGroot, F.M.F.; Fontaine, A.; Kao, C.C.; Krisch, M. *J. Phys.: Condens. Matter* **1994**, *6*, 6875-6884.

Gelasco, A.; Askenas, A.; Pecoraro, V.L., *J. Am. Chem. Soc.*, submitted (1995).

Gorun, S.M.; Stibrany, R.T., manuscript in preparation. A preliminary account of this work was presented at the ACS National Meeting, Atlanta, GA, 1991a.

Gorun, S.M.; Stibrany, R.T., U.S. Patent No. 5,041,575 (1991b).

Gorun, S.M.; Stibrany, R.T., U.S. Patent No. 5,099,045 (1991c).

Hendrickson, D.N.; Christou, G.; Schmitt, E.A.; Libby, E.; Baskin, J.S.; Wang, S.; Tsai, H.-L.; Vincent, J.B.; Boyd, P.D.W.; Huffman, J.C.; Folting, K.; Li, Q.; Streib, W.E. *J. Am. Chem. Soc.* **1992**, *114*, 2455-2471.

Karpenko, V.; Kinney, J.H.; Kulkarni, S.; Neufeld, K.; Poppe, C.; Tirsell, K.G.; Wong, J.; Cerino, J.; Troxel, T.; Yang, J.; Hoyer, E.; Green, M.; Humphries, D.; Marks, S.; Plate, D. *Rev. Sci. Instr.* **1989**, *60*, 1451- 1456.

Kawai, J.; Takami, M.; Satoko, C. *Phys. Rev. Lett.* **1990**, *65*, 2193-2196.

Libby, E.; McCusker, J.K.; Schmitt, E.A.; Folting, K.; Hendrickson, D.N.; Christou, G. *Inorg. Chem.* **1991**, *30*, 3486-3495.

Nyholm, R.; Mårtensson, N.; Lebugle, A.; Axelsson, U. *J. Phys.* **1981**, *F 11*, 1727.

Peng, G.; van Elp, J.; Jang, H.; Que, L., Jr.; Armstrong, W.H.; Cramer, S.P. *J. Amer. Chem. Soc* **1995**, *117*, 2515-2519.

Randall, K.J.; Eberhardt, W.; Feldhaus, J.; Erlebach, W.; Bradshaw, A.M.; Xu, Z.; Johnson, P.D.; Ma, Y. *Nucl. Instr. and Meth A* **1992**, *319*, 1-3:101-105.

Schake, A.R.; Vincent, J.B.; Li, Q.; Boyd, P.D.W.; Folting, K.; Huffman, J.C.; Hendrickson, D.N.; Christou, G.*Inorg. Chem.* **1989**, *28*, 1915-1923.

Schulz, A. unpublished neutron diffraction data; presented at the ACS National Meeting, San Diego, CA, 1994.

van der Laan, G.; Kirkman, I.W. *J. Phys.: Condens. Matter* **1992**, *4*, 4189-4204.

Chapter 3: The High Resolution X-ray Fluorescence Experiment

For mixed-valence manganese systems in electrochemical batteries and metalloprotein clusters, probing Mn(II), Mn(III), and Mn(IV) sites individually would yield more information than conventional XAS which averages over all Mn environments in the sample. Using ion-desorption detection (Jaeger et al., 1980), luminescence detection (Goulon et al., 1984 and Dexpert-Ghys et al., 1990), x-ray standing waves (Yokoyama et al., 1989 and Malgrange et al., 1992), and diffraction anomalous fine structure (DAFS) (Sorenson et al., 1994 and Pickering et al., 1993), site-selective XAS has been recorded. However, each of these techniques requires specific types of samples which are generally not applicable to non-crystalline bulk materials.

Chemical shifts in x-ray emission have been known for many years (Ekstig et al., 1970). With the use of custom-built spectrometers consisting of spherically bent crystals in a Rowland circle geometry, the line-sharpening (Hämäläinen et al.,1991) and spin-selectivity (Hämäläinen et al., 1992 and Peng et al., 1994) gained from high resolution fluorescence spectroscopy has become appreciated (Hämäläinen et al., 1994).

The Mn high resolution fluorescence spectrometer (Figure 3.1) consists of spherically bent Si(440) crystals and a NaI scintillation counter positioned on a Rowland circle with diameter of 85 cm. The fluorescence from the sample is reflected by the crystal and refocussed at the detector, the position depending on the emission energy according to the Bragg equation:

$$n\lambda = 2d\sin\theta \qquad (1)$$

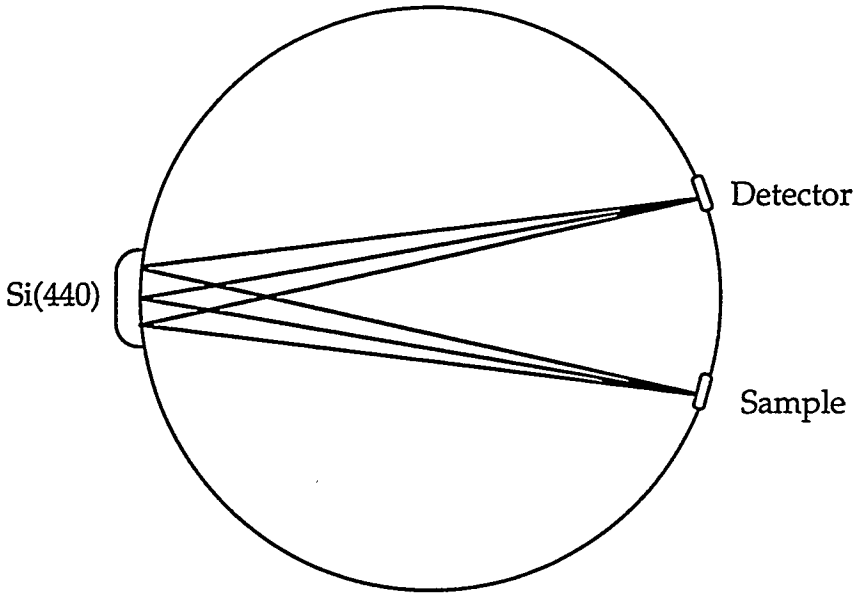

Figure 3.1: The Custom Built High Resolution Fluorescence Spectrometer (side view).

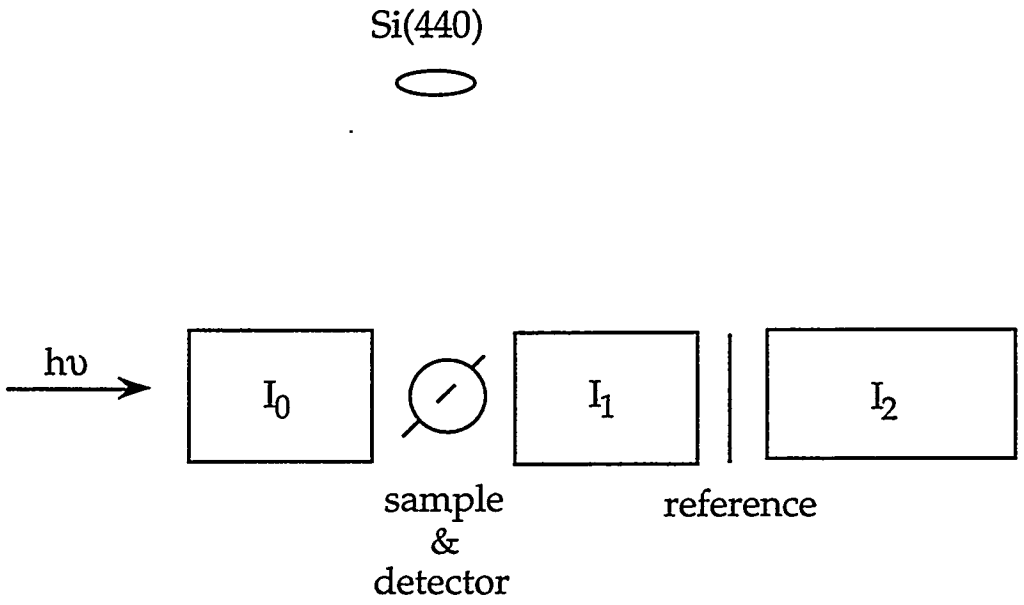

Figure 3.2: The High Resolution Fluorescence Experimental Set-up (top view). The Rowland circle shown in Figure 3.1 is now perpendicular to the page.

where n is the order of reflection, λ is the wavelength of the incident energy, $2d$ is the lattice spacing, and θ is the angle of reflection. More than one crystal can be used to collect a larger solid angle of fluorescence, creating a set of intersecting Rowland circles. The resolution of the spectrometer with a single analyzer has been shown to be ~ 0.3 eV (Stojanoff et al., 1992).

By setting the beamline monochromator energy above the Mn K-edge, the angle of sample to crystal to detector can be scanned and emission spectra recorded. Alternately, the fluorescence at a particular energy (angle) can be detected while scanning the beamline monochromator, thus recording excitation (absorption) spectra. The spectrometer is designed such that simultaneously monitoring the sample by transmission as well as collecting reference spectra are possible during absorption measurements (see Figure 3.2).

One limiting factor in these measurements is the solid angle of fluorescence collected. We have recently begun to use form-bent crystals instead of spherically bending a silicon wafer. Eliminating the need for the bending apparatus allows the positioning of the individual crystals closer together for collection of a larger solid angle of sample fluorescence. The form-bent crystals were obtained from Crismatec and consist of a Si(440) wafer mounted onto a spherically-curved glass holder. Count rates from the form-bent crystals were approximately twice that from the mechanically bent crystals, mainly due to the larger 2" diameter of usable surface area as compared to only about a 1" diameter region which bends approximately spherically for the wafers. Our current spectrometer can accomodate up to 6 form-bent crystals.

Spectra of the following model compounds are presented in this chapter. $Mn_2O(CH_3CO_2)_2Cl_2(bipy)_2](CH_3CO_2H)\cdot H_2O$ (Vincent et al., 1993),

$Mn_2(biphen)_2(biphenH)(bipy)_2$ (Bashkin et al., 1988), $Mn_2O(CH_3CO_2)_2(bpy)_2(H_2O)_2](ClO_4)_2$ (Vincent et al., 1993), $Mn_2(CH_3CO_2)_2(bpy)_2(H_2O)(S_2O_8)\cdot H_2O$ (Blackman et al., 1991), $Mn_2O_2(bipy)_4(ClO_4)_3$ (Plaskin, 1972), $Mn_2O_2(CH_3CO_2)Cl_2(bpy)_2$ (Bashkin et al., 1988), $[Mn_2(CH_3CO_2)_2(bpy)_2(H_2O)_2][ClO_4]_2$ (Schake et al., 1994), $[Mn_2O_2(pic)_4]$ (Christou, 1989), $Mn_3O(O_2CPh)_6(py)_2(H_2O)$ (Vincent et al., 1987), $Mn_3(O_2CPh)_6(bpy)_2$ (Vincent et al., 1989), $[Mn_3O(O_2CCH_3)_6(py)_3](ClO_4)$ (Vincent et al., 1987), and $Mn_4O_3Cl(O_2CCH_3)_3(dbm)_3$ (Hendrickson et al., 1992) were synthesized in the G. Christou laboratory. $Mn(HB(3,5\text{-}(CH_3)_2pz)_3)_2$ (Chan, 1991), $[Mn_4O_2(tphpn)_2(H_2O)_2(ClO_4)_2](ClO_4)_3$ (Chan, M.K. et al., 1990), Mn(acen)Cl (Boucher et al., 1977), $[Mn(HB(3,5\text{-}(CH_3)_2pz)_3)_2][ClO_4]$ (Chan, 1991), $[Mn(HB(3,5\text{-}(CH_3)_2pz)_3)_2][ClO_4]_2$ (Chan et al., 1989), $[Mn_2(HB(3,5\text{-}(CH_3)_2pz)_3)_2(\mu\text{-}OH)(CH_3CO_2)_2][PF_6]$ (Sheats et al., 1987), $[Mn_4O_6(1,4,7\text{-triazacyclononane})_4](ClO_4)_4$ (Wieghardt et al., 1983), $[Mn_2O_2(phen)_4](ClO_4)_3$ (Cooper et al., 1977), and $[Mn_2Zn_2O_2(tphpn)_2(H_2O)_2(ClO_4)_2](ClO_4)_3$ (Suzuki et al., 1990) were prepared in the W.H. Armstrong laboratory. $Mn(B(pz)_4)_2$ (Brooker et al., 1989) was synthesized in the McKee laboratory and $[Mn(phen)]Cl_3$ (Gmelins, 1982) and $K_3Mn(CN)_6$ (Trageser et al., 1978) in the Cramer laboratory. $[L_2Mn_2(\mu\text{-}O)(CH_3CO_2)_2][BPh_4]_2$ (Wieghardt et al., 1985) and $[L_2Mn_2(\mu\text{-}O)_3][PF_6]_2\cdot H_2O$ where L=N,N',N''-trimethyl(-1,4,7-triazacyclononane) (Wieghardt et al., 1988) were prepared in the K. Wieghardt laboratory. $BaMn_8O_{16}\cdot 2H_2O$ was provided by A. Campbell and $Mn(acac)_2$, $Mn(acac)_3$, $MnCl_2$, and MnF_2 were used as obtained from Aldrich Chemical Company.

Model compounds were finely powdered, diluted with BN or sucrose to a concentration of ≤ 10 %Mn(w/w), and packed in copper sample holders with a depth of ~1 mm. For emission spectra recorded on Beamline X21, the

model compounds were mixed with Ducoa cement and placed into Lucite sample holders. The physical mixture consisted of equal amounts of Mn from MnF_2 and $BaMn_8O_{16}\cdot 2H_2O$ with a total Mn concentration of 10 %Mn(w/w). The trimer EXAFS was measured at ~77 K using a Janis liquid nitrogen cryostat; the site-selective and spin-selective EXAFS used a Displex He refrigerator operating at a temperature of ~30 K; all other spectra were recorded at room temperature.

Mn K-edge absorption spectra presented in this chapter were recorded on NSLS Beamline X25 (Berman et al., 1992) using a Si(220) excitation monochromator and the Si(440) fluorescence analyzer(s). The emission spectra were recorded on Beamline X21 (Kao et al., 1995) using 14 keV excitation except for the emission spectra of $Mn_3O(O_2CPh)_6(py)_2(H_2O)$, $Mn(O_2CPh)_6(bpy)_2$, $[MnO(O_2CMe)_6(py)_3](ClO_4)$, and $Mn_2O_2(bpy)_4(ClO_4)_3$ which were measured on Beamline VI-2 at SSRL (Hoyer et al., 1983) with a Si(111) excitation monochromator. Conventional Mn EXAFS of $Mn_3O(O_2CPh)_6(py)_2(H_2O)$ were recorded on Exxon Beamline X10C at the NSLS (Sansone et al., 1991) using a Si(220) monochromator.

The main Kβ peak of MnF_2 was used as a reference for emission spectra. This energy (6491.7 eV) had been previously determined by using the measurement of the analyzer angle for the Kβ peak of a Mn foil as a reference. The spectra were calibrated by linear shifts in theta before converting to eV. It was necessary to subtract a linear background from the X21 data. All emission spectra were normalized to unit intensity at the Kβ peak except for the physical mixture and spin-selective XANES studies. Excitation spectra were analyzed as described in Chapter 1.

Kβ Emission

Kβ fluorescence results from a 3p electron filling a 1s core hole and is sensitive to the 3d valence shell of first row transition metals through exchange and spin-orbit couplings. Using the high resolution fluorescence technique, both the energy and shape of the Mn Kβ emission have been shown to depend on the oxidation and spin state of Mn (Peng et al., 1994). The Kβ emission spectra from a series of homovalent Mn compounds are shown in Figure 3.3. The main features of these spectra are a peak (Kβ) and a satellite (Kβ'), separated by approximately 16 eV. The Kβ emission results from transitions with a final state containing a spin down 3p hole, the Kβ' to a spin up hole, with up being the direction of the majority spin in the 3d level. The splitting between the two main features is a result of the 3p-3d exchange splitting, while other processes, such as spin-orbit coupling, exert smaller effects on the spectra. These spectra are much more sensitive to oxidation state changes than to different ligand field values, with the exception of low spin spectra which differ greatly from spectra of high spin compounds both in the position of the Kβ peak and the magnitude of the Kβ' satellite. As an example, the Kβ emission spectra of high and low spin Mn(III) are contrasted in Figure 3.4.

Examination of the Kβ peak energy shift with oxidation state for high spin Mn complexes shows a correlation between the two, as is presented in Figure 3.5. The Kβ peak energies and the corresponding model compounds which were used in this approximation are tabulated at the end of this chapter (Table 3.1). Using the linear regression from this set of model

Figure 3.3: Chemical Shifts in Mn Kβ Emission Spectra. From top to bottom: $Mn(II)Cl_2$ (solid line) and $Mn(II)(B(pz)4)_2$ (dotted line); Mn(III)(acen)Cl (solid line) and $Mn(III)(acac)_3$ (dotted line); and $Mn(IV)(HBpz_3)_2[ClO_4]_2$ (solid line) and $[L_2Mn(IV)_2(\mu\text{-}O)_3][PF_6]_2$ (dotted line).

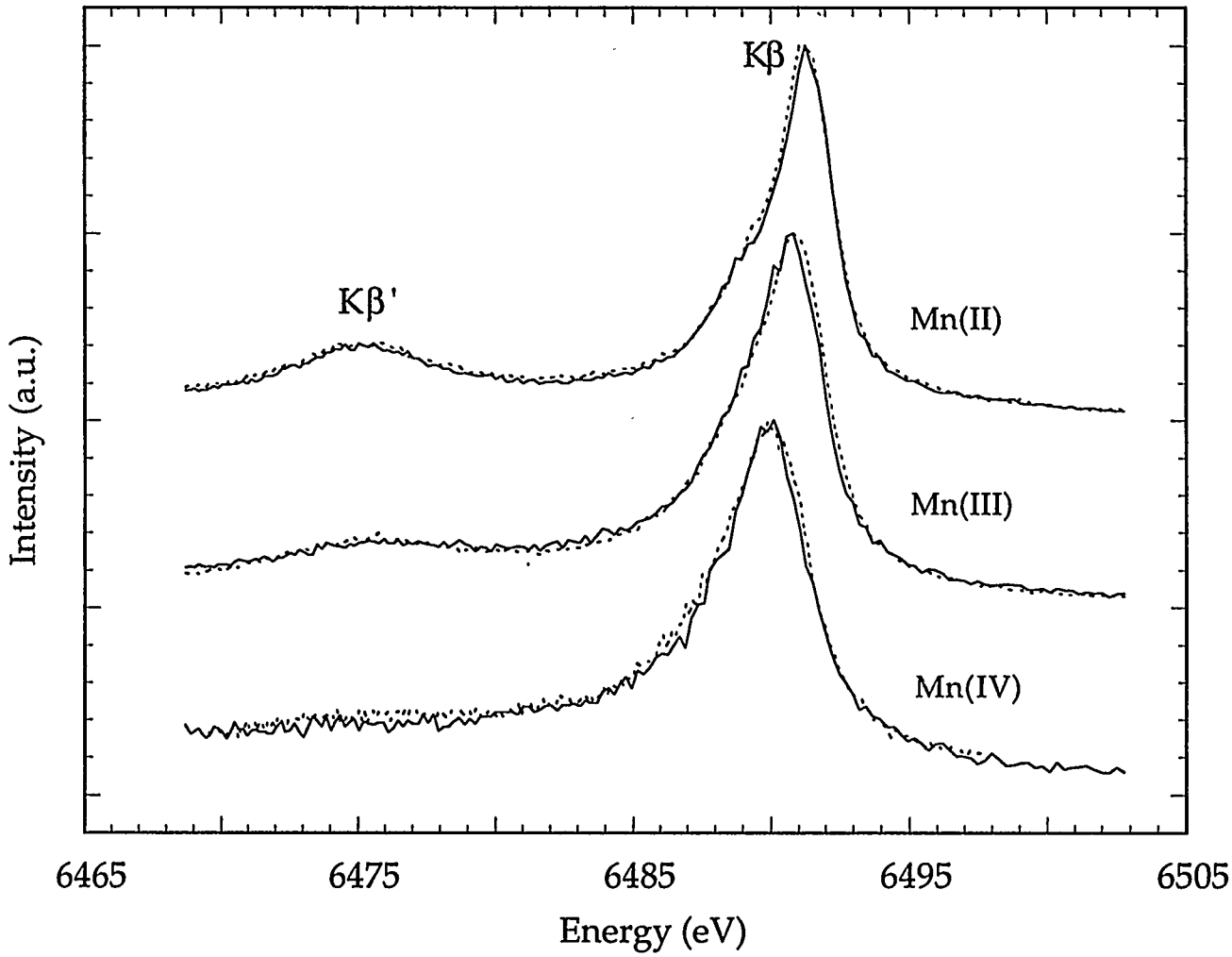
Kβ
Kβ'
Mn(II)
Mn(III)
Mn(IV)
Intensity (a.u.)
6465
6475
6485
6495
6505
Energy (eV)

Figure 3.4: Kβ Emission Spectra of High Spin versus Low Spin Mn(III). From top to bottom: low spin $[Mn(HBpz_3)_2][ClO_4]$ and high spin $Mn(acac)_3$.

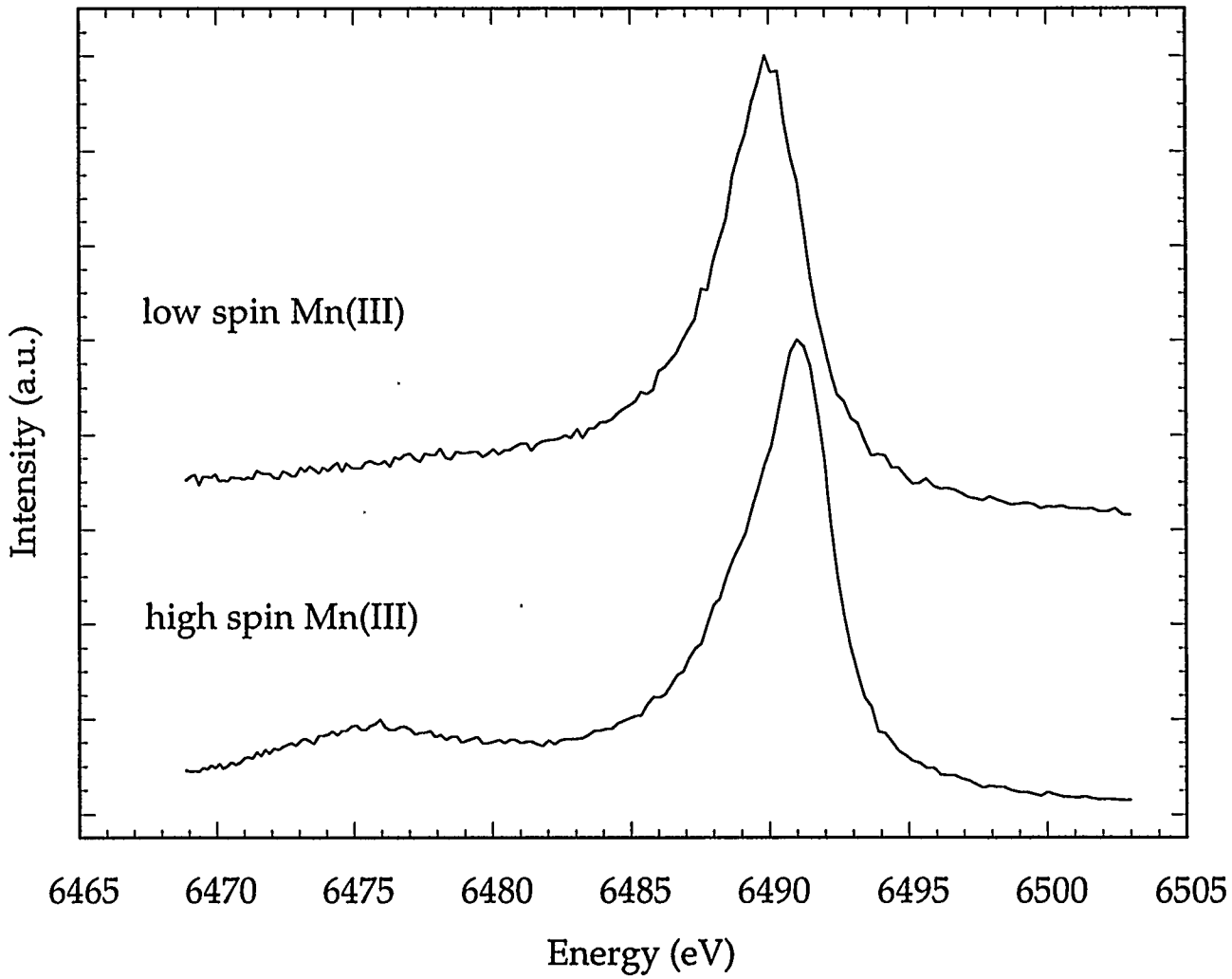
low spin Mn(III)
high spin Mn(III)
Intensity (a.u.)
6465
6470
6475
6480
6485
6490
6495
6500
6505
Energy (eV)

Figure 3.5: The correlation of average Mn oxidation state and Kβ emission peak energy for a series of high spin Mn model compounds. Linear regression: $y = 6492.7 - 0.68065 \times x, r^2 = 0.96$.

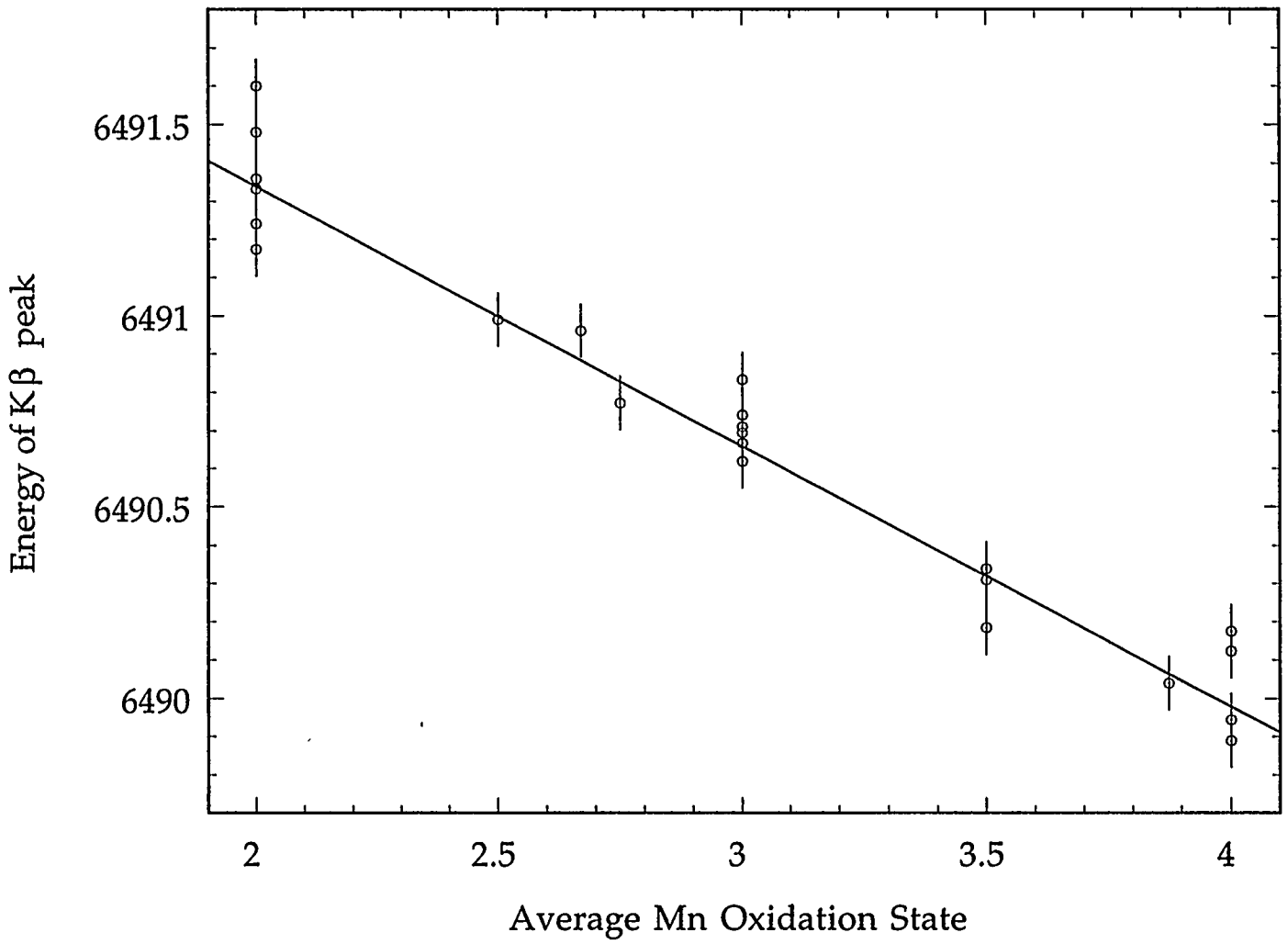
6491.5
6491
6490.5
6490
Energy of Kβ peak
2
2.5
3
3.5
4
Average Mn Oxidation State

compounds, a predicted average oxidation state should be accurate to ± 0.3 with a 95% confidence level. The Kβ peak position is a relatively easy way to obtain a rough average Mn oxidation state for an unknown compound. However, caution must be used with multinuclear Mn clusters as the uncertainties associated with this simple correlation can become overwhelming.

Site-Selectivity

In addition to making it possible to assign an average oxidation state to an unknown Mn complex, the shifting to lower energy of the Kβ emission with increasing oxidation state also suggests the possibility of selectively probing the absorption spectrum of a single oxidation state in a mixed valence complex by monitoring the appropriate emission energy. The feasibility of the site-selective XAS technique is demonstrated in this section. Site-selective XANES of a physical mixtue of two Mn components, $Mn(II)F_2$ and $BaMn(III)Mn(IV)_7O_{16}\cdot 2H_2O$, illustrates the qualitative information obtainable from this technique. This is also shown in XANES experiments on $[Mn(II)Mn(III)Mn(IV)Mn(II)O_2(tphpn)_2(H_2O)_2(ClO_4)_2](ClO_4)_3$, a chemically coupled mixed valence system. Studies on a mixed valence manganese trimer, $Mn(II)Mn(III)_2O(O_2CPh)_6(py)_2(H_2O)$, show that quantitative information is extractable from site-selective EXAFS.

The Kβ emission spectra of pure $Mn(II)F_2$, $BaMn(III)Mn(IV)_7O_{16}\cdot 2H_2O$, and a physical mixture containing equal amounts of Mn from each of these compounds are presented in Figure 3.6. As expected, the Mn(II) spectrum is at higher energy than that of the $BaMn_8O_{16}\cdot 2H_2O$ and the physical mixture emission is nicely simulated by the average of the two pure component

Figure 3.6: Left: Mn Kβ Emission Spectra of MnF_2 (top, (II)), $BaMn_8O_{16}\cdot 2H_2O$ (bottom, $(III)(IV)_7$), a physical mixture consisting of equal amounts of Mn from both components (middle, —), and the average of the pure component spectra (middle, ····); the energy monitored for probing predominately Mn(II) species in the physical mixture is indicated (arrow). Right: Mn XANES spectra obtained from MnF_2 (—, (II)), $BaMn_8O_{16}\cdot 2H_2O$ (– ··· – ···, $(III)(IV)_7$), and the physical mixture monitored at 6491.4 eV (· · ·, "(II)").

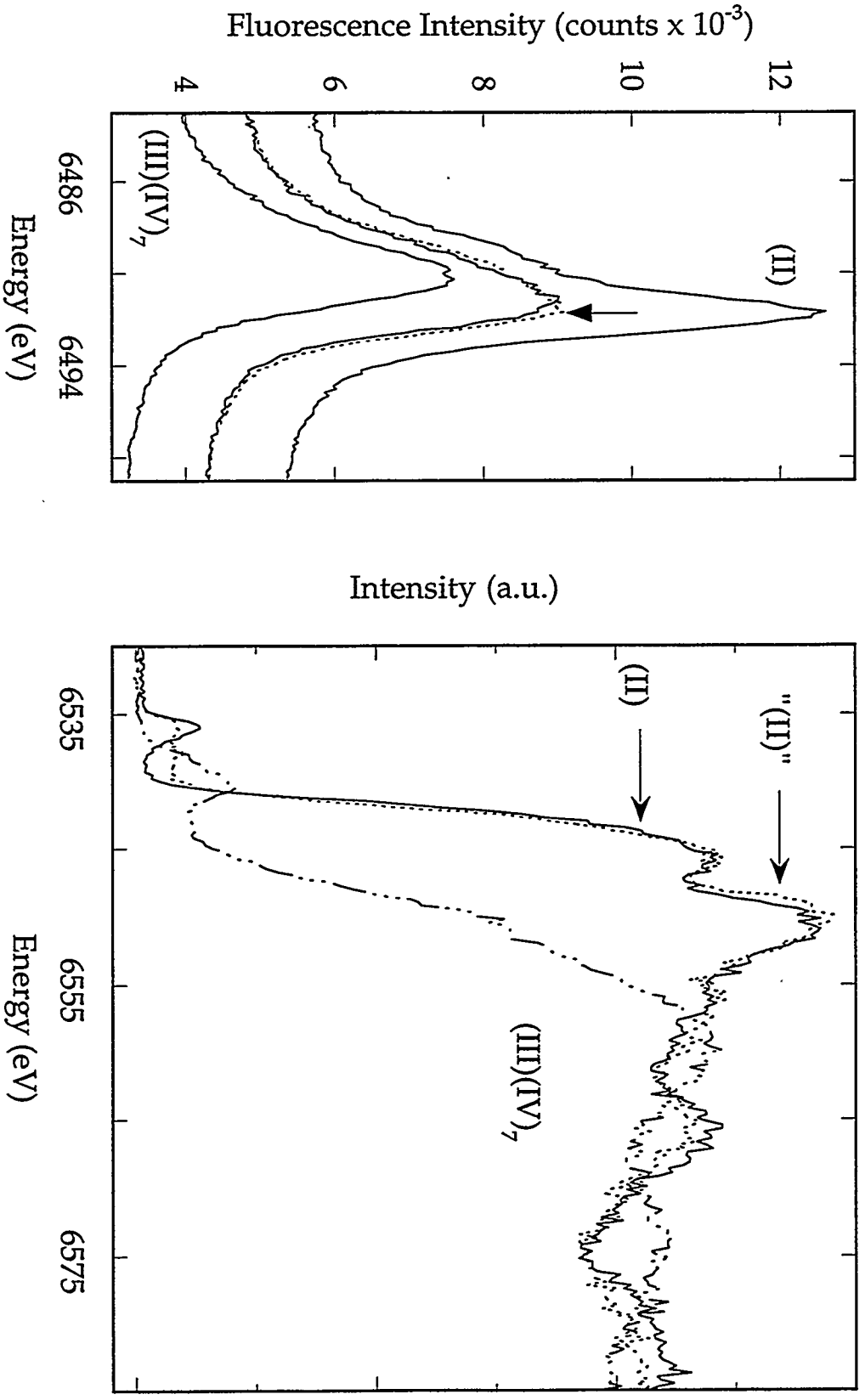
Fluorescence Intensity (counts x 10^{-3})
4
6
8
10
12
(II)
$(III)(IV)_7$
6486
6494
Energy (eV)
Intensity (a.u.)
(II)
"(II)"
$(III)(IV)_7$
6535
6555
6575
Energy (eV)

spectra. The emission spectra in this series were not normalized to unit intensity at the Kβ peak as they contained equal amounts of Mn.

The fluorescence analyzer was set at an energy selective for Mn(II), 6491.4 eV, and the excitation energy was scanned. A Mn K-edge spectrum selective for the Mn(II) component of the physical mixture was obtained (Figure 3.6). In the region above 6540 eV, the Mn(II)-selective XANES is almost identical to that of the pure Mn(II) component. Some differences occur in the pre-edge region which may be due to contamination from the $BaMn_8O_{16}\cdot 2H_2O$ or to resonant Raman scattering (deGroot et al., 1995). These results show the feasibility of probing Mn(II) sites in a mixture of Mn oxidation states to obtain qualitative information.

Site-selective XANES of a series of Mn model compounds are presented in Figure 3.7. The spectrum obtained by monitoring predominately the lowest oxidation state present in $[Mn_4O_2(tphpn)_2(H_2O)_2(ClO_4)_2](ClO_4)_3$, a tetramer with the oxidation states Mn(II)Mn(III)Mn(IV)(Mn(II), is distinctively characteristic of Mn(II) - note the relatively sharp edge as compared to the rounded edge from the higher oxidation states.

Mixed valence $Mn(III)_x(IV)_y$ spectra vary with detection energy as well. However, similar differences are also present in the "site-selective" edges of homovalent $Mn(III)_4$ and $Mn(IV)_4$ compounds (Figure 3.7). In order to fully understand the subtleties of site-selective XANES, a comprehensive mapping of the dependence of Mn K-edges on detection energy will have to be undertaken on a number of characterized systems with different oxidation states and ligand fields.

To demonstrate that quantitative information can be obtained from site-selective EXAFS of mixed valence complexes, the transmission, emission, and excitation spectra of $Mn_3O(O_2CPh)_6(py)_2(H_2O)$ were recorded. This

Figure 3.7: Site-Selective XANES of Mn Model Compounds. From top to bottom: $[Mn(II)Mn(III)Mn(IV)Mn(II)O_2(tphpn)_2(H_2O)_2(ClO_4)_2](ClO_4)_3$ monitored at 6489.0 eV (dotted line) and 6491.9 eV (solid line); $Mn(III)_4O_2(CH_3CO_2)_6(py)_2(dbm)_3$ monitored at 6488.7 eV (dotted line) and 6492.0 eV (solid line); $[Mn(III)Mn(IV)Zn_2O_2(tphpn)_2(H_2O)_2\ (ClO_4)_2](ClO_4)_3$ monitored at 6488.3 eV (dotted line) and 6491.7 eV (solid line); $[Mn(IV)_4O_6(1,4,7\text{-triazacyclononane})_4](ClO_4)_4$ monitored at 6488.1 eV (dotted line) and 6491.4 eV (solid line). The higher detection energies correspond to spectra favoring the lower oxidation state and the lower detection energies to the higher oxidation state(s).

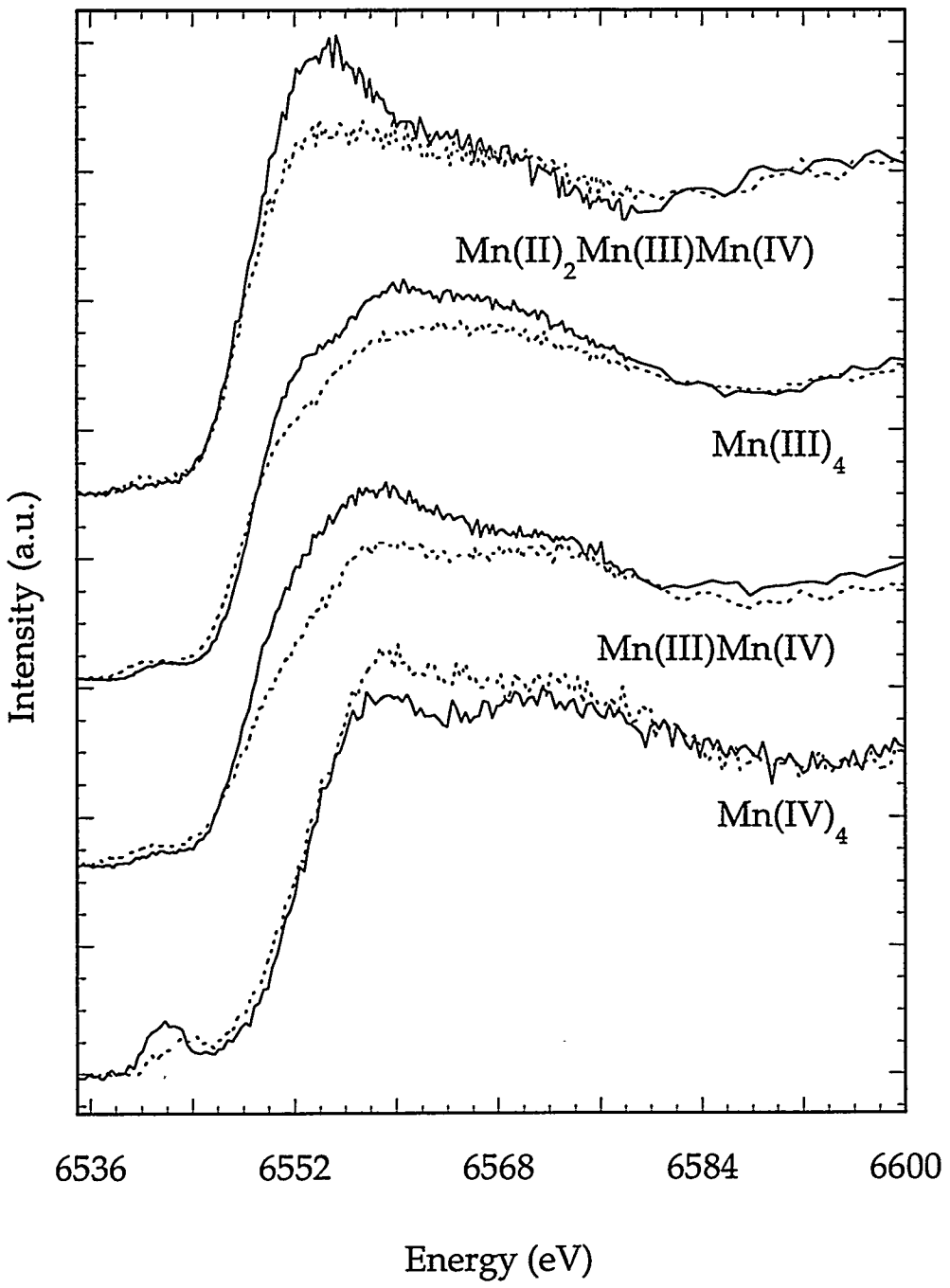
Mn(II)2Mn(III)Mn(IV)
Mn(III)4
Mn(III)Mn(IV)
Mn(IV)4
Intensity (a.u.)
6536
6552
6568
6584
6600
Energy (eV)

trinuclear mixed valence system has a single trapped valence Mn(II) center with a different local structure from the two Mn(III) ions (Vincent et al., 1987) (Figure 3.8). The Mn(II)-Mn(III) distances are 3.36 Å ± 0.02 Å while the Mn(III)-Mn(III) distance is 3.21 Å. Thus, from the Mn(II) perspective the Mn-Mn interactions are homogenous, while the Mn(III) sites see a more disordered environment with 2 different Mn-Mn distances, which should result in weaker Mn-Mn EXAFS. The overall average Mn-Mn interaction is 3.31 ± 0.07 Å and should be the Mn-Mn distance observed when this complex is probed by conventional EXAFS.

The Kβ emission spectra of $Mn(II)Mn(III)_2O(O_2CPh)_6(py)_2(H_2O)$, $Mn(II)_3(O_2CPh)_6(bpy)_2$, and $[Mn(III)_3O(O_2CMe)_6(py)_3](ClO_4)$ are presented in Figure 3.9. The Kβ emission spectrum of $Mn_3O(O_2CPh)_6(py)_2(H_2O)$ is nicely simulated by a weighted average of $Mn(II)_3$ and $Mn(III)_3$ component spectra.

EXAFS of the Mn(II) and Mn(III) species were selectively probed by monitoring the Kβ fluorescence at 6492.6 eV and 6488.9 eV, respectively, and traditional EXAFS was recorded by transmission. The site-selective EXAFS oscillations are clearly different from each other (Figure 3.10). Although they are similar at low k to the transmission spectrum, at high k the site-selective spectra show stronger and sharper oscillations, presumably due to eliminating disorder inherent in probing more than one type of Mn. The Fourier transform of the Mn(II) spectrum, which reflects 2 Mn-Mn interactions at 3.36 Å, shows a clear peak for this interaction, while the transmission and Mn(III) selective spectra show much broader structure in this region.

EXAFS data were isolated as described in Chapter 1 and smoothed with a window of 0.1 and 0.3 k for the transmission and site-selective data, respectively. Due to the noise in the site-selective data, a k- range of 2 to 9 $Å^{-1}$

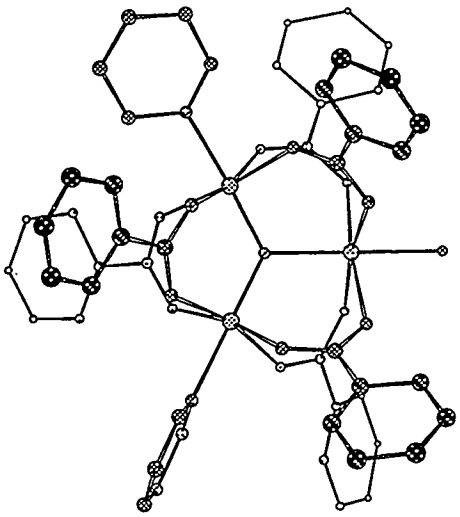

Mn-Mn distances

Mn(II) - Mn(III) 3.36Å

Mn(III) - Mn(III) 3.21Å

Theoretical average Mn-Mn distance

Transmission	3.31Å
Mn(II) EXAFS	3.36Å
Mn(III) EXAFS	3.29Å

Figure 3.8: Model of $Mn_3O(O_2CPh)_6(py)_2(H_2O)$, shown without the H atoms.

Figure 3.9: Mn Kβ Emission Spectra. $Mn(II)Mn(III)_2O(O_2CPh)_6(py)_2(H_2O)$ (top, ——); the energies monitored for probing predominately Mn(III) and Mn(II) species, respectively, are indicated (arrows). Shown below for comparison are the Kβ emission spectra of $Mn(II)_3(O_2CPh)_6(bpy)_2$ (——, $(II)_3$) and $[Mn(III)_3O(O_2CMe)_6(py)_3](ClO_4)$ (· · · ·, $(III)_3$). Also shown is the weighted average of the $Mn(II)_3$ and $Mn(III)_3$ spectra (top, · · · ·).

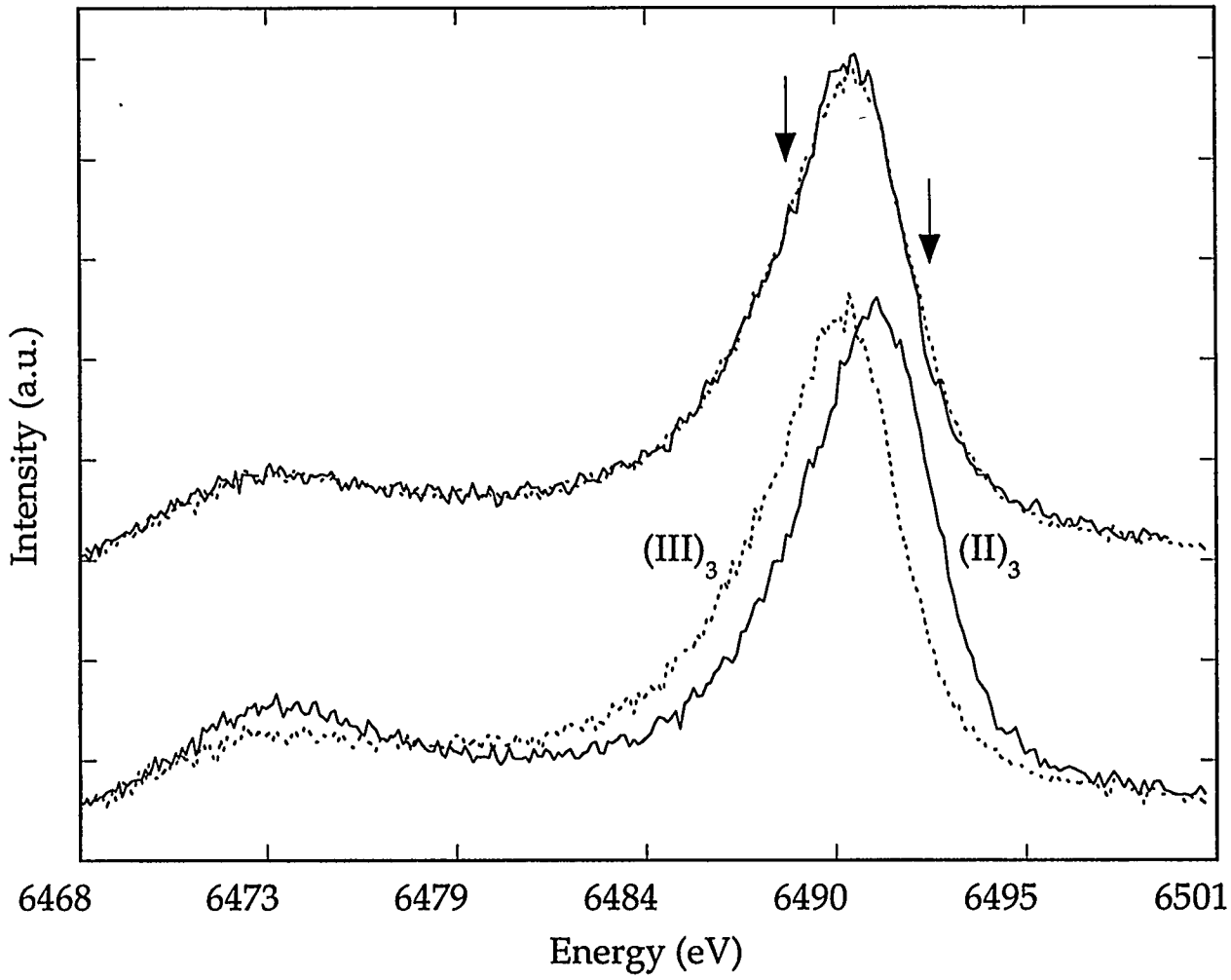
Intensity (a.u.)
(III)3
(II)3
6468
6473
6479
6484
6490
6495
6501
Energy (eV)

Figure 3.10: EXAFS data (—) and simulation using one Mn-Mn distance (···) for $Mn_3O(O_2CPh)_6(py)_2(H_2O)$, monitored by transmission (top); site selective EXAFS using 6492.6 eV detection (middle); and using 6488.9 eV detection (bottom). Right: Fourier transform of the EXAFS data (—) and simulation using one Mn-Mn distance (···) for transmission (top, $(II)(III)_2$); 6492.6 eV detection (middle, "(II)"); and 6488.9 eV detection (bottom, "(III)"). The Fourier transforms have been phase corrected for Mn.

Intensity (a.u.)
10
5
0
-5
2
4
6
8
k (Å^{-1})
Intensity (a.u.)
2.4
2
1.6
1.2
0.8
0.4
0
(II)(III)$_2$
"(II)"
"(III)"
0
2
4
6
R (Å)

was used for the simulations and Fourier transforms of all data sets. The number of variables allowed to vary in the simulations is determined by the following relationship:

$$M = \frac{2(\Delta k)(\Delta R)}{\pi} \cdot \qquad (2)$$

where M is the maximum number of independent variables, Δk is the k-range of data used in the simulations, and ΔR is the range in distance-space of information-containing data. For these data sets, the number of independent variables is 14. Simulations on other Mn models compounds have indicated that assigning E_0 the arbitrary value of 6548 eV typically results in the value of ΔE_0 being -10.0 ± 1.0 eV and that the additional improvement in the fit obtained by allowing ΔE_0 to vary is generally negligible. In order to stay within the number of variable parameters allowed for this limited range of data, ΔE_0 was fixed at -10.0. The rest of the parameters - coordination number, distance, and debye-waller disorder - were allowed to vary with the exception of the total octahedral coordination number for the short Mn-O shell and the coordination numbers of the Mn-Mn interactions which were set to values obtained from the crystal structure.

A good fit to the transmission data was obtained using either 2 Mn-Mn interactions at 3.32 Å or $^2/_3$ Mn-Mn at 3.22 Å and $^4/_3$ at 3.37 Å, as well as Mn-O components at 1.85 and 2.13 Å (Figure 3.10). Simulations of the smoothed site-selective EXAFS required 2 Mn-O components and at least one Mn-Mn component (Figure 3.10). Shells of O and C at 3.0 Å and 3.4 Å also contribute and complicate the analysis. The Mn(II)-selective data was best fit to a homogenous Mn-Mn component at 3.36 Å ($R_{crystal}$ = 3.36 Å). For the Mn(III)-selective measurement, the emission from Mn(III) always overlaps

that from Mn(II), and the selectivity is lower. Nevertheless, spectra taken using 6488.9 eV detection predominately probe the Mn(III) sites. Fitting with a single Mn-Mn interaction gave an average distance of 3.29 Å ($R_{crystal-ave}$ = 3.29 Å). A slightly better fit was obtained when the Mn(III)-Mn interaction was split into two components at 3.22 Å ($R_{crystal}$ = 3.21 Å) and 3.34 Å ($R_{crystal}$ = 3.36 Å). The simulation parameters from these and additional fits are summarized in Table 3.2 at the end of this chapter. Better statistics and a wider range of data would allow better discrimination between different models, however it is clear that quantitative site-selective information can be obtained using this technique.

Spin-Selectivity

The separation between the Kβ and Kβ' regions in Mn emission spectra results in the potential for measuring spin-polarized spectra. The Kβ emission results mainly from transitions with a final state containing a spin down 3p hole. The shoulder on the low energy side of the Kβ peak, however, arises from a spin up hole, as does fluorescence in the Kβ' region. Thus by selecting detection energies on the high energy side of the Kβ peak and in the Kβ' region, the resulting spectra are polarized spin down and spin up, respectively, where up is taken to be the direction of the majority spin of the 3d electrons (see Figure 3.11).

The feasibility of spin-selective XAS is best illustrated using a high spin Mn(II) example. High spin Mn(II) has five d electrons in the spin up orientation. As all the up positions are already filled, only 1s to 3d transitions for spin down electrons should be allowed. This is indeed observed experimentally, as is shown in Figure 3.12. The XANES have not been

Figure 3.11: Mn Kβ Emission spectrum of MnF_2. The energies monitored for Kβ and Kβ' detection are indicated and the direction of the arrow represents the spin polarization of the core hole with respect to the 3d majority spin. The spin up transition region illustrated with an asterisk beside the arrow was not monitored.

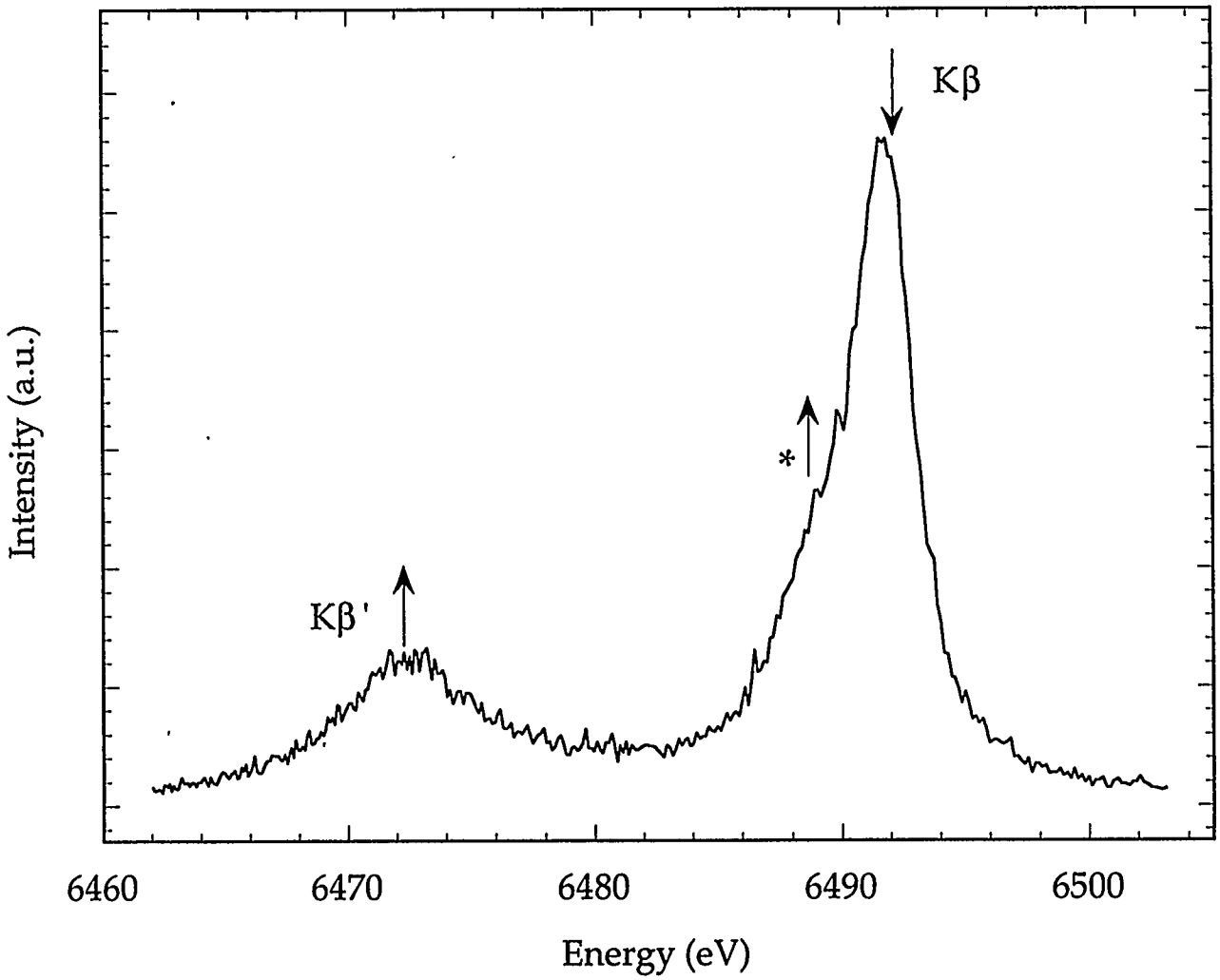
Kβ
*
Kβ'
Intensity (a.u.)
6460
6470
6480
6490
6500
Energy (eV)

Figure 3.12: A demonstration of spin-selectivity using MnF_2. Mn XANES using Kβ detection (solid line) and Kβ' detection (dashed and dotted line). The 1s to 3d pre-edge feature is only observed when the outgoing electron is spin down (Kβ detection).

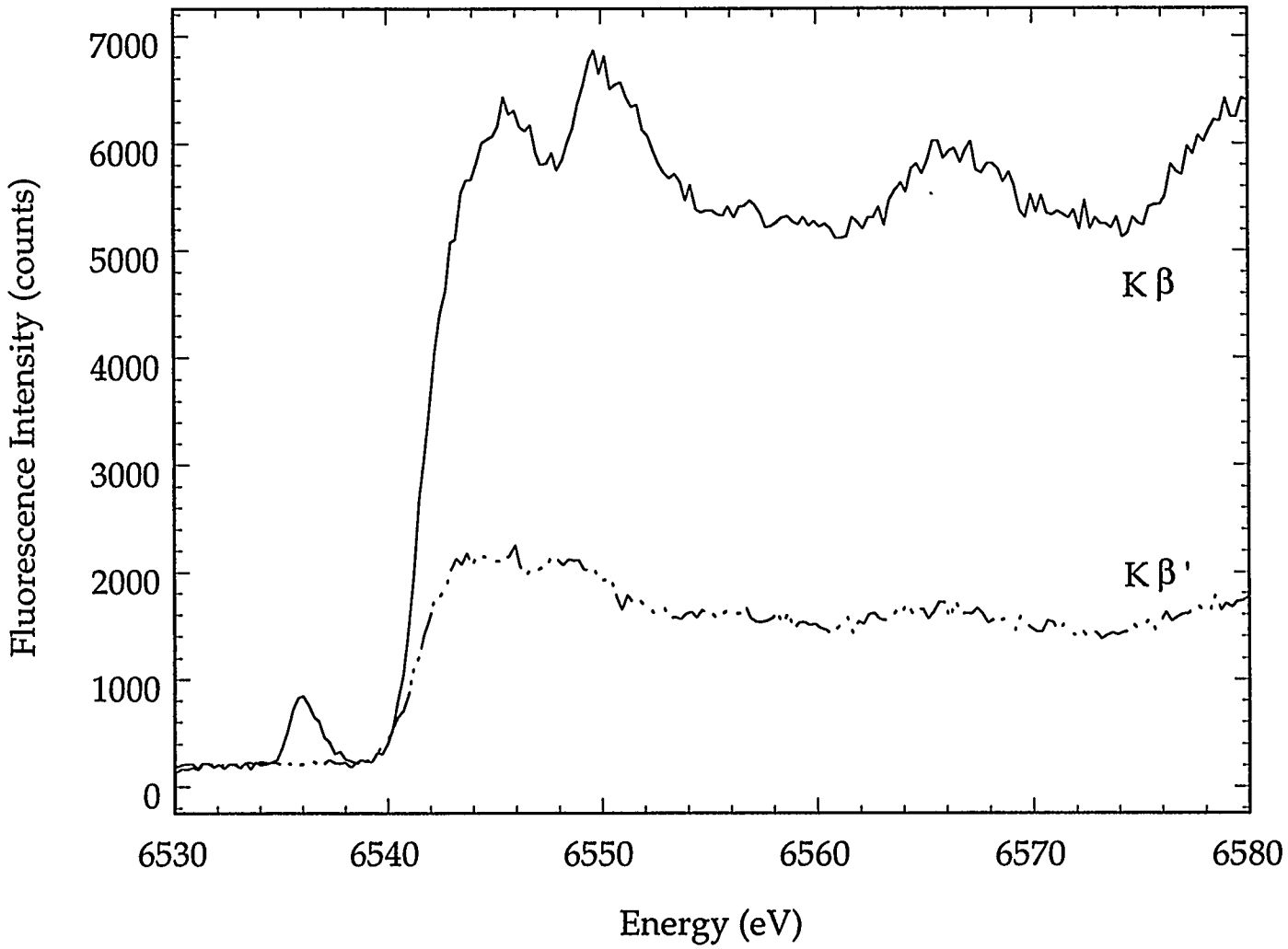
Fluorescence Intensity (counts)
7000
6000
5000
4000
3000
2000
1000
0
6530
6540
6550
6560
6570
6580
Energy (eV)
Kβ
Kβ'

Figure 3.13: SPEXAFS of MnF_2 recorded using high resolution fluorescence detection. Left: The k^2-weighted spin-polarized EXAFS, as obtained from Kβ' (solid line) and Kβ detection (dotted line) and smoothed over a 0.1 $Å^{-1}$ range. Right: The spin-polarized Fourier transforms, as obtained from Kβ' (solid line) and Kβ detection (dotted line). The Fourier transforms have been phase corrected for Mn.

Fluorescence Intensity (counts)
7000
6000
5000
4000
3000
2000
1000
0
6530
6540
6550
6560
6570
6580
Energy (eV)
Kβ
Kβ'
Intensity (a.u.)
0.35
0.3
0.25
0.2
0.15
0.1
0.05
0
0 1 2 3 4 5 6 7 8
R (Å)

normalized and instead reflect the difference in intensity resulting from Kβ versus Kβ' detection. Only when the outgoing electron is spin down (Kβ detection) is there a significant amount of intensity in the pre-edge region.

This suggests that spin polarized EXAFS (SPEXAFS) can be obtained by subtracting the two spin-polarized spectra. The EXAFS should then be due to only paramagnetic scatterers as the diamagnetic contributions should be identical in the two spin orientations and cancel out. Extra care must be taken in both the background subtraction and normalization steps as a bad spline can mask spin-dependent changes in the Fourier transforms. As a test case, the spin-selective EXAFS of MnF_2 was recorded. The spin up and down spectra are different from each other, as is illustrated in Figure 3.13. The raw data were smoothed over a 0.1 $Å^{-1}$ range and only the k^2 EXAFS data from 1.0 to 8.5 $Å^{-1}$ were used in the Fourier transforms. As is expected, the first peak in the Fourier transform, due to fluoride backscatterers, is very similar in the spin up and spin down spectra while contributions from Mn backscatterers at 3.3, 3.8, 4.9, and 5.9 Å are spin-dependent.

Once a library of spin selective EXAFS data is assembled, the existing theory can be tested and further developed to allow quantitative analysis of SPEXAFS. One can envision being able to collect and analyze SPEXAFS from protein systems, gaining information on only the paramagnetic scatterers. For systems such as Photosystem II (see Chapter 7) where there are multiple contributions to the EXAFS at similar distances, being able to ignore the diamagnetic scatterers would greatly simplify the obtainment of structural information. High resolution fluroescence detected SPEXAFS can be obtained from paramagnetic and antiferromagnetic complexes, as well as ferromagnetic samples, in a comparatively straightforward manner as compared to current methods. Using the core hole electron as an internal

spin reference eliminates the need for the circularly polarized light and powerful magnets which have recently made collection of spin polarized XAS on paramagnetic metalloproteins possible using x-ray detected magnetic circular dichroism (van Elp et al., 1993).

The high resolution Kβ fluorescence technique offers many useful applications for mixed valence Mn systems such as Photosystem II. Kβ emission spectra can provide an approximate oxidation state prediction for an unknown complex. In addition, site- and spin-selective EXAFS can drastically simplify the extraction and analysis of structural information from Mn clusters.

Table 3.1: Data Points for the Correlation of Average Mn Oxidation State and Kβ peak energy.

Model Compound	Average Mn Oxidation State		Kβ peak(eV)
$Mn(II)_3(O_2CPh)_6(bpy)_2$	2.00		6491.60
$Mn(II)(acac)_2$	2.00		6491.48
$Mn(II)(HB(3,5\text{-}(CH_3)_2pz)_3)_2$	2.00		6491.36
$MnCl_2$	2.00		6491.33
$Mn(II)(B(pz)_4)_2$	2.00		6491.24
$[Mn(II)_2(HB(3,5\text{-}(CH_3)_2pz)_3)_2\text{-}(\mu\text{-}OH)(CH_3CO_2)_2][PF_6]$	2.00		6491.17
		Mn(II) average =	6491.36
$Mn(II)Mn(III)biphen_2\text{-}(biphenH)(bipy)_2$	2.50		6490.99
$Mn(II)Mn(III)_2O(O_2CPh)_6(py)_2\text{-}(H_2O)$	2.67		6490.96
$[Mn(II)Mn(III)Mn(IV)Mn(II)O_2\text{-}(tphpn)_2(H_2O)_2(ClO_4)_2]\text{-}(ClO_4)_3$	2.75		6490.77
$Mn(III)(acac)_3$	3.00		6490.83
$[Mn(phen)]Cl_3$	3.00		6490.74
$Mn(III)_2O(CH_3CO_2)_2(bpy)_2(H_2O)_2]\text{-}(ClO_4)_2$	3.00		6490.71
$Mn(III)_2O(CH_3CO_2)_2Cl_2(bipy)_2]\text{-}(CH_3CO_2H)^*H_2O$	3.00		6490.71
$[L_2Mn(III)_2O(CH_3CO_2)_2][BPh_4]_2$	3.00		6490.71
$[Mn(III)_3O(O_2C(CH_3))_6(py)_3](ClO_4)$	3.00		6490.69
Mn(III)(acen)Cl	3.00		6490.67
$Mn(III)_4O_2(CH_3CO_2)_6(py)_2(dbm)_3$	3.00		6490.67
$Mn(III)_2(CH_3CO_2)_2(bpy)_2(H_2O)\text{-}(S_2O_8)$	3.00		6490.62
		Mn(III) average =	6490.71
$[Mn(III)(HB(3,5\text{-}(CH_3)_2pz)_3)_2][ClO_4]$	3.00	***	6489.63
$K_3Mn(III)(CN)_6$	3.00	***	6489.38
$Mn_2(III,IV)O_2(bipy)_4(ClO_4)_3$	3.50		6490.34
$[Mn_2O_2(CH_3CO_2)Cl_2(bpy)_2$	3.50		6490.31
$[Mn_2(III,IV)O_2(phen)_4](ClO_4)_3$	3.50		6490.19
		Mn(III)Mn(IV) average =	6490.28

$BaMn(III)Mn(IV)_7O_{16}\cdot 2H_2O$	3.875		6490.04
$[Mn(IV)_2(CH_3CO_2)_2(bpy)_2(H_2O)_2]$-$[ClO_4]_2$	4.00		6490.18
$[Mn_2(IV,IV)O_2(pic)_4]$	4.00		6490.12
$[Mn(IV)_4O_6$(1,4,7-triazacyclononane)$_4](ClO_4)_4$	4.00		6490.00
$[L_2Mn(IV)_2(\mu\text{-}O)_3][PF_6]_2$	4.00		6489.94
$[Mn(IV)(HB(3,5\text{-}(CH_3)_2pz)_3)_2]$-$[ClO_4]_2$	4.00		6489.89
		Mn(IV) average =	6490.02

*** low spin complexes, not used in correlation plots

Table 3.2: Simulation Parameters for $Mn_3O(O_2CPh)_6(py)_2(H_2O)$ spectra

1. Mn(II) Selective Data

N	A-B	R fit (crystal)	σ^2	E_0	F
2.5	Mn-O	1.963	.00467	-05.11	0.27
3.5	Mn-O	2.174	.00100	-12.30	
2.0	Mn-Mn	3.411 (3.364)	.00658	-13.61	
3.1	Mn-O	1.947	.01057	-10.00	0.35
2.9	Mn-O	2.195	.00100	-10.00	
2.0	Mn-Mn	3.435 (3.364)	.00685	-10.00	
3.2	Mn-O	1.948	.01163	-10.00	0.30
2.8	Mn-O	2.196	.00100	-10.00	
4.0	Mn-O	3.451	.00138	-10.00	
4.0	Mn-C	3.145	.01077	-10.00	
2.0	Mn-Mn	3.364 (3.364)	.00549	-10.00	
3.2	Mn-O	1.946	.01164	-10.00	0.29
2.8	Mn-O	2.196	.00100	-10.00	
4.0	Mn-O	3.452	.00159	-10.00	
2.8	Mn-C	3.142	.00673	-10.00	
2.0	Mn-Mn	3.363 (3.364)	.00537	-10.00	

$$F = \frac{\Sigma\left|X(k)_{exp} - X(k)_{fit}\right|^2}{N_{points}}$$

2. Mn(III) Selective Data

N	A-B	R fit (crystal)	σ^2	E_0	F
2.5	Mn-O	1.934	.01140	-03.46	0.43
3.5	Mn-O	2.159	.00432	-12.10	
2.0	Mn-Mn	3.005 (3.289)	.01048	-17.97	
2.5	Mn-O	1.922	.00558	-05.18	0.18
3.5	Mn-O	2.130	.00139	-15.68	
1.0	Mn-Mn	3.161 (3.214)	.00150	01.44	
1.0	Mn-Mn	3.454 (3.364)	.00290	06.67	
2.5	Mn-O	1.878	.01190	-10.00	0.49
3.5	Mn-O	2.164	.00580	-10.00	
2.0	Mn-Mn	3.050 (3.289)	.01071	-10.00	
2.5	Mn-O	1.870	.01244	-10.00	0.32
3.5	Mn-O	2.160	.00656	-10.00	
1.0	Mn-Mn	3.047 (3.214)	.00221	-10.00	
1.0	Mn-Mn	3.276 (3.364)	.01229	-10.00	
2.8	Mn-O	1.877	.01394	-10.00	0.47
3.2	Mn-O	2.163	.00493	-10.00	
4.0	Mn-O	3.407	.00428	-10.00	
6.0	Mn-C	3.077	.00291	-10.00	
2.0	Mn-Mn	3.288 (3.289)	.00806	-10.00	
2.8	Mn-O	1.877	.01378	-10.00	0.41
3.2	Mn-O	2.163	.00484	-10.00	
4.0	Mn-O	3.413	.00420	-10.00	
4.6	Mn-C	3.076	.00100	-10.00	
2.0	Mn-Mn	3.288 (3.289)	.00806	-10.00	
2.7	Mn-O	1.874	.01320	-10.00	0.46
3.3	Mn-O	2.161	.00538	-10.00	
4.0	Mn-O	3.410	.00561	-10.00	
6.0	Mn-C	3.076	.00364	-10.00	
1.0	Mn-Mn	3.221 (3.214)	.00736	-10.00	
1.0	Mn-Mn	3.342 (3.364)	.00353	-10.00	
2.7	Mn-O	1.874	.01289	-10.00	0.38
3.3	Mn-O	2.160	.00521	-10.00	
4.0	Mn-O	3.419	.00567	-10.00	
4.3	Mn-C	3.076	.00100	-10.00	
1.0	Mn-Mn	3.220 (3.214)	.00779	-10.00	
1.0	Mn-Mn	3.341 (3.364)	.00312	-10.00	

3. Transmission Data

N	A-B	R fit (crystal)	σ^2	E_0	F
1.25	Mn-O	1.842	.00610	-01.05	0.10
4.75	Mn-O	2.060	.01451	-13.76	
2.00	Mn-Mn	3.315 (3.314)	.01812	-22.95	
1.25	Mn-O	1.815	.00870	-06.29	0.10
4.75	Mn-O	2.076	.01691	-12.43	
0.67	Mn-Mn	3.242 (3.214)	.00342	03.66	
1.33	Mn-Mn	3.331 (3.364)	.00477	-15.35	
2.4	Mn-O	1.846	.02159	-10.00	0.17
3.6	Mn-O	2.127	.01364	-10.00	
2.0	Mn-Mn	3.423 (3.314)	.02149	-10.00	
2.4	Mn-O	1.845	.02216	-10.00	0.13
3.6	Mn-O	2.123	.01390	-10.00	
0.67	Mn-Mn	2.981 (3.214)	.01153	-10.00	
1.33	Mn-Mn	3.373 (3.364)	.02474	-10.00	
2.4	Mn-O	1.841	.02126	-10.00	0.13
3.6	Mn-O	2.123	.01358	-10.00	
4.0	Mn-O	3.454	.00153	-10.00	
5.33	Mn-C	3.053	.02756	-10.00	
2.0	Mn-Mn	3.316 (3.314)	.00649	-10.00	
2.4	Mn-O	1.843	.02147	-10.00	0.11
3.6	Mn-O	2.125	.01358	-10.00	
4.0	Mn-O	3.456	.00209	-10.00	
2.7	Mn-C	3.040	.01477	-10.00	
2.0	Mn-Mn	3.316 (3.314)	.00629	-10.00	
2.5	Mn-O	1.845	.02124	-10.00	0.15
3.5	Mn-O	2.125	.01266	-10.00	
4.0	Mn-O	3.450	.00793	-10.00	
5.33	Mn-C	3.054	.03405	-10.00	
0.67	Mn-Mn	3.235 (3.214)	.00611	-10.00	
1.33	Mn-Mn	3.372 (3.364)	.00709	-10.00	
2.5	Mn-O	1.847	.02185	-10.00	0.12
3.5	Mn-O	2.127	.01291	-10.00	
4.0	Mn-O	3.443	.00949	-10.00	
2.2	Mn-C	3.009	.01616	-10.00	
0.67	Mn-Mn	3.224 (3.214)	.00554	-10.00	
1.33	Mn-Mn	3.365 (3.364)	.00737	-10.00	

Bashkin, J.S.; Schake, A.R.; Vincent, J.B.; Chang, H.-R.; Li, Q.; Huffman, J.C.; Chirstou, G.; Hendrickson, D.N. *J. Chem. Soc., Chem. Commun.* **1988**, 700-702.

Berman, L.E. ; Hastings, J.B.; Oversluizen, T.; Woodle, M. *Rev. Sci. Instrum.* **1992**, *63*, 428-432.

Blackman, A.G.; Huffman, J.C.; Lobkovsky, E.B.; Christou, G. *J. Chem. Soc., Chem. Commun.* **1991**, 989-991.

Brooker, S.; McKee, V. *J. Chem. Soc., Chem. Commun.* **1989**, 619-620.

Boucher, L. J.; Day, V.W. *Inorg. Chem.* **1977**, *16*, 1360-1367.

Chan, M.K.; Armstrong, W.H. *Inorg. Chem.* **1989** *28*, 3777-3779.

Chan, M.K.; Armstrong, W.H. *J. Am. Chem. Soc.* **1990** *112*, 4985-4986.

Chan, M.K. **1991** Ph.D thesis, University of California, Berkeley.

Christou, G. *Acc. Chem. Res.* **1989**, *22*, 328-335.

Cooper, S.R.; Calvin, M. *J. Am. Chem. Soc.* **1977** *99*, 6623-6630.

deGroot, F.M.F.; Pizzini, S.; Fontaine, A.; Hämäläinen, K.; Kao, C.-C.; Hastings, J.B. *Phys. Rev. B - Cond. Matt.* **1995**, *51*, 1045-1052.

Dexpert-Ghys, J.; Piriou, B.; Jacquetfrancillon, N.; Sombret, C. *J. Non-Crys. Sol.* **1990**, *1-2*, 117-128.

Ekstig, B.; Källne, E.; Noreland, E.; Manne, R. *Phys. Scripta* **1970**, *2*, 38-44.

Gmelins Handbuch der Anorganishen Chemie. Vol. D3 **1982**, pp201,241, Springer-Verlag, Berlin.

Goulon, J.; Tola, P.; Brochon, J. C.; Lemonnier, M.; Dexpert-Ghys, J.; Guilard, R. *EXAFS and Near Edge Structure III;* Hodgson, K. O., Hedman, B., Penner-Hahn, J. E., Eds., Springer-Verlag: Berlin, 1984, pp. 490-495.

Hämäläinen, K.; Siddons, D. P.; Hastings, J. B.; Berman, L. E.; *Phys. Rev. Lett.*, **1991**, *67*, 2850-2853.

Hämäläinen, K.; Kao, C.-C.; Hastings, J. B.; Siddons, D. P.; Berman, L. E.; Stojanoff, V.; Cramer, S. P. *Phys. Rev. B*, **1992**, *46*, 14274-14277.

Hämäläinen, K.; Siddons, D. P.; Berman, L. E.; Kao, C.-C.; Hastings, J. B. *Resonant Anomalous X-ray Scattering*; Materlik, G., Sparks, C. J., Fischer, K., Eds., Elsevier Science: Amsterdam, 1994, pp. 485-493.

Hendrickson, D.N.; Christou, G.; Schmitt, E.A.; Libby, E.; Baskin, J.S.; Wang, S.; Tsai, H.-L.; Vincent, J.B.; Boyd, P.D.W.; Huffman, J.C.; Folting, K.; Li, Q.; Streib, W.E. *J. Am. Chem. Soc.* **1992**, *114*, 2455-2471.

Hoyer, E.; Bahr, C.; Chan, T.; Chin, J.; Elioff, T.; Halbach, K.; Harnett, G.; Humphries, D.; Hunt, D.; Kim, K.-J.; Lauritzen, T.; Lindel, D.; Shirley, D.; Tafelski, R.; Thompson, A.; Cramer, S.; Eisenberger, P.; Hewitt, R.; Stöhr, J.; Boyce, R.; Brown, G.; Golde, A.; Gould, R.; Hower, N.; Lindau, I.; Winick, H.; Yang, J.; Harris, J.; Scott, B. *Nucl. Inst. & Meth.* **1983**, *208*, 117-125.

Jaeger, R.; Stöhr, J. *Phys. Rev. Lett.* **1980**, *45*, 1870-1873.

Kao, C.C.; Hämäläinen, K.; Krisch M.; Siddons, D.P.; Oversluizen, T.; Hastings, J.B. *Rev. Sci. Inst.* **1995** *66*, 1699-1702.

Malgrange C.; Ferret D. *Nuc. Inst. Meth.* **1992**, *314*, 285-296.

Peng, G.; deGroot, F.M.F.; Hämäläinen, K.; Moore, J. A.; Wang, X.; Grush, M.M.; Hastings, J.B. ; Siddons, D.P.; Armstrong, W.H.; Mullins, O.C.; Cramer, S.P. *J. Am. Chem. Soc.* **1994**, *116* , 2914-2920.

Pickering, I. J.; Sansone M.; Marsch J.; George G. N. *Jap. J. App. Phys.* **1993**, *32*, 206-208.

Plaskin, P.M.; Stoufer, R.C.; Mathews, M.; Palenik, G.J. *J. Am. Chem. Soc.* **1972** *94*, 2121-2122.

Sansone, M.; Via, G.; George, G.N.; Meitzner, G.; Hewitt, R. *X-ray Absorption Fine Structure;* Hasnain, S.S., Ed., Ellis Horwood Ltd.: W. Sussex, England, 1991, pp. 656-658.

Schake, A.R.; Tsai, H.-L.; Webb, R.J.; Folting, K., Christou, G.; Hendrickson, D.N.*Inorg. Chem.* **1994** *33,* 6020-6028.

Sheats, J.E.; Czernuszewicz, R.S.; Dismukes, G.C.; Rheingold, A.L.; Petrouleas, V.; Stubbe, J.; Armstrong, W.H.; Beer, R.H.; Lippard, S.J. *J. Am. Chem. Soc.* **1987** *109,* 1435-1444.

Sorensen, L. B.; Cross, J. O.; Newville, M.; Ravel, B.; Rehr, J. J.; Stragier, H.; Bouldin, C. E.; Woicik, J. C. *Resonant Anomalous X-ray Scattering;* Materlik, G., Sparks, C. J., Fischer, K., Eds., Elsevier Science: Amsterdam, 1994, pp. 389-420.

Stojanoff, V.; Hämäläinen, K.; Siddons, D.P.; Hastings, J.B.; Berman, L.E.; Cramer, S.; Smith, G. *Rev. Sci. Instrum.* **1992** *63,* 1125-1127.

Suzuki, M.; Senda, H.; Suenaga, M.; Sugisawa, T.; Uehara, A. *Chem. Lett.* **1990** 923-926.

Trageser, G.; Eysel, H.H. *Inorg. Nucl. Chem. Lett.* **1978**, *14,* 65-70.

VanElp J.; George, S.J.; Chen, J.; Peng G.; et al.*PNAS* **1993** 90, 9664-9667.

Vincent, J. B.; Chang, H.-R.; Folting, K.; Huffman, J. C.; Christou, G.; Hendrickson, D. N. *J. Am. Chem. Soc.* **1987** *109,* 5703-5711.

Vincent, J.B.; Christmas, C.; Chang, H.-R.; Li, Q.; Boyd, P.D.W.; Huffman, J.C.; Hendrickson, D.N.; Christou, G. *J.Am.Chem.Soc.* **1989** *111,* 2086-2097.

Vincent, J.B.; Tsai, H.-L.; Blackman, A.G.; Wang, S.; Boyd,P.D.W.; Folting,K.; Huffman,J.C.; Lobkovsky,E.B.; Hendrickson,D.N.; Christou, G. *J.Am.Chem.Soc.* **1993** *115,* 12353-12361.

Wieghardt, K.; Bossek, U.; Gerbert, W. *Angew. Chem. Int. Ed. Engl.* **1983** 22, 328- 329.

Wieghardt, K.; Bossek, U.; Ventur, D.; Weiss, J. *J. Chem. Soc. Chem., Chem. Commun.* **1985** 347-349.

Wieghardt, K.; Bossek, U.; Nuber, B.; Weiss, J.; Bonvoisin, J.; Corbella, M.; Vitols, S.E.; Gired, J.J. *J. Am. Chem. Soc.* **1988** *110,* 7398-7411.

Yokoyama, T.; Takata, Y.; Yoshiki, M.; Ohta, T.; Funabashi, M.; Kitajima, Y.; Kuroda, H. *Jap. J. App. Phys.* **1989** *28,* L1637-L1640.

Part II : Biological Systems

Chapter 4: Mn Catalase - L-edge Experiments

Catalases are responsible for the detoxification of hydrogen peroxide to the less harmful species of molecular oxygen and water in aerobic cells (Penner-Hahn et al., 1992):

$$2H_2O_2 \rightarrow 2H_2O + O_2 \qquad (1).$$

Although most catalases are heme proteins, manganese catalases have been isolated from three species of bacteria, *Lactobacillus plantarum* (Kono et al., 1983), *Thermoleophilum album* (Algood et al., 1986), and *Thermus thermophilus* (Barynin et al., 1986). These catalases are similar and all contain a pair of Mn at the active site. In *L. plantarum*, each dinuclear Mn site is contained in a 34 kDa subunit and is thought to be arranged in a homohexameric fashion (Baldwin, 1991).

It has been proposed, based on electron paramagnetic resonance (EPR), XANES, optical, and reactivity studies, that the native enzyme cycles between Mn(II)Mn(II) and Mn(III)Mn(III) oxidation states (Penner-Hahn, 1992). A mechanism for the breakdown of hydrogen peroxide based on these oxidation states has been presented by J.E. Penner-Hahn and is shown in Figure 4.1. Results from optical spectroscopy suggest that the two Mn are linked by an oxo bridge in the Mn(III)Mn(III) form, and that this bridge may play a role in the mechanism (Penner-Hahn, 1992). The (μ-oxo)(μ-carboxylato)$_2$ bridging structure shown is common in binuclear Mn(III) models. Typical Mn-Mn distances for this geometry are 3.0-3.3 Å. EXAFS of the reduced Mn(II)Mn(II) form do not require a Mn-Mn interaction around 3.3 Å in order to obtain a

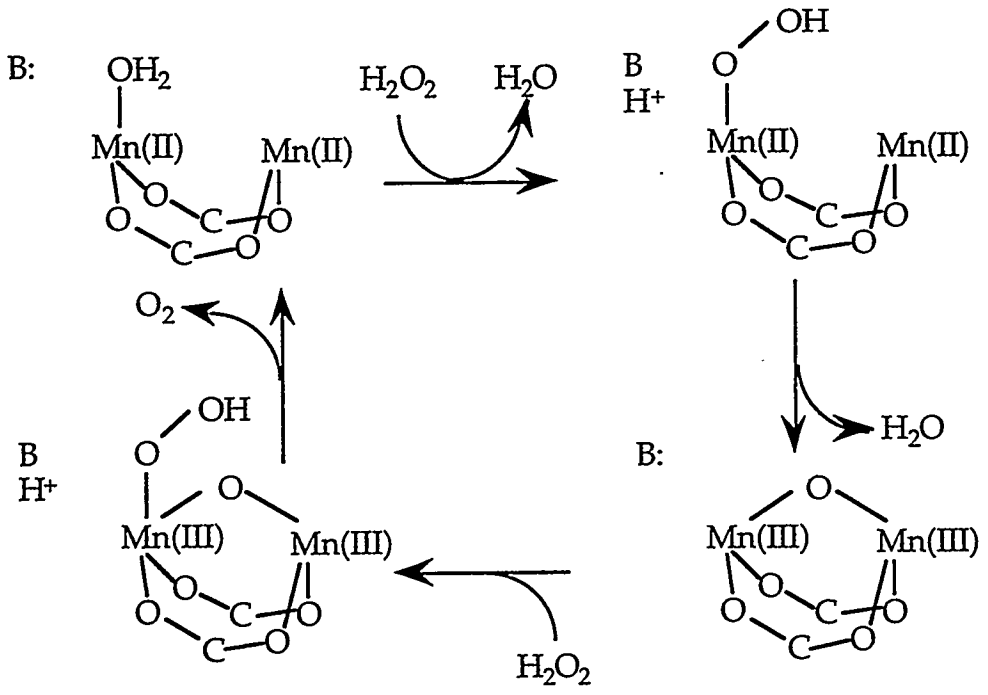

Figure 4.1: A Proposed Mechanism for Mn Catalase. B represents a basic amino acid side chain facilitating H transfer.

good fit. However, simulations of the super-oxidized Mn(III)Mn(IV) include a Mn-Mn distance of 2.67 Å (Waldo et al., 1992). This distance is indicative of $(\mu\text{-oxo})_2$ bridging and is a major structural change from that which has been proposed for the active enzyme. EXAFS (Waldo et al., 1991; Waldo et al., 1992) and electron spin echo studies (Dikanov et al., 1988; Stemmler et al., manuscript in preparation) indicate the presence of at least one histidine imidazole ligand to the Mn. More recent EPR and pulsed EPR studies, however, indicate that a nitrogen from a lysine residue forms a bridge between the two Mn in superoxidized catalase and also rule out the presence of a histidine ligand (Ivancich et al., 1995). These results concur that the majority of the ligands to the manganese are oxygen. However, the number and types of ligands have not been conclusively determined for the reduced

or super-oxidized forms of catalase. Understanding the electronic structure of the Mn sites at different parts of the catalytic cycle, including the oxidation states, ligand fields, and magnetic couplings, is important for understanding the overall mechanism.

The work presented here has been performed on Mn catalase isolated from *L. plantarum* by T.L. Stemmler in the J.E. Penner-Hahn lab (University of Michigan). Both the reduced Mn(II)Mn(II) and a super-oxidized Mn(III)Mn(IV) form were available for characterization and comparison with the more complicated catalytic system of Photosystem II. The Mn catalase was purified from *L. plantarum* as has been described by Kono et al (Kono et al., 1983), with the exception that chromatographic separation using fast flow Sepharose was performed instead of the initial batchwise DEAE extraction, and a G-150 Sephadex column was added for final size exclusion. Samples were then concentrated to 35.9 mg/mL and assayed using a Clark-type oxygen electrode interfaced to a Zenith PC. The specific activity of these samples was typically 3600 AU/mg, where 1 activity unit corresponds to the decomposition of 1 mmol of H_2O_2/min, $[H_2O_2]$ = 20 mM. The total Mn concentration was ~5 mM. Thin films of protein were dried on Si wafers. Analysis of a thin film of Mn(II)Mn(II) catalase which had been exposed to the x-ray beam for approximately 24 hours, temperature cycled numerous times, exposed to ultra high vacuum, and rehydrated still showed 60-70% of the original specific activity.

The protein spectra were recorded on undulator Beamline X1B at the National Synchrotron Light Source (Randall et al., 1992), with the undulator gap set at 41.5 mm, and on the soft x-ray station of wiggler Beamline 10-1 at the Stanford Synchrotron Radiation Lab (Karpenko et al., 1989). The beamline monochromator slits were set at 30 microns, resulting in the energy

resolution of the beamline being ~0.29 eV. Thin films of the protein on silicon wafers were transferred to a cold finger inside the UHV chamber and placed at a glancing angle with respect to the incoming beam. Protein samples were maintained at a temperature of ~30 K with a Janis cryostat.

Using a combination of filters and a 13 element windowless Ge detector as described in Chapter 2, the single channel analyzer windows were set for acceptance of Mn L_α fluorescence and the Mn L-edge spectra of Mn catalase in both the reduced and super-oxidized states were measured. Mn model spectra presented here for comparison with the catalase were recorded as previously described in Chapter 2. The data presented here was analyzed by the same methods as described earlier (Chapter 2).

Figure 4.2 presents the spectrum of Mn catalase in the reduced form. This spectrum consists of a main L_{III} peak at 640 eV and a smaller L_{II} peak ~12 eV higher. Also shown for comparison are the spectrum from $[Mn_4(2\text{-}OHpicpn)_4](ClO_4)_4$ and the results from atomic multiplet simulations on Mn(II)Mn(II) catalase. The catalase spectrum is a sum of a total of 10 scans, 4 seconds per point, and has been smoothed with a window of 0.2 eV.

$[Mn_4(2\text{-}OHpicpn)_4](ClO_4)_4$ is a so-called "dimer of dimers" model compound, consisting of divalent Mn with octahedral coordination. It has a sharp L_{III} peak at 640 eV and a broader L_{II} edge at 652 eV (Figure 4.2). There are two resolved shoulders on the high energy side of the L_{III} in this $[MnN_4O_2]$ compound, as well as an unresolved shoulder on the low energy side. The L_{II} region is split into a doublet. These features are consistent with those from the Mn(II)Mn(II) catalase spectrum. Spectra from compounds with significant ionic character, such as $MnSO_4$, have a well resolved shoulder ~1 eV lower than the main L_{III} peak. (compare Figure 4.2 with Figure 2.5).

Figure 4.2: Mn_2(II/II) L-edge Absorption Spectra. From top to bottom: a) Mn_2(II/II) catalase; b) $[Mn_4(2\text{-}OHpicpn)_4](ClO_4)_4$, a Mn_2(II/II) dimer of dimers; c) atomic multiplet simulation of Mn_2(II/II) catalase, theoretical calculation (sticks) and smoothed theoretical spectrum (solid line).

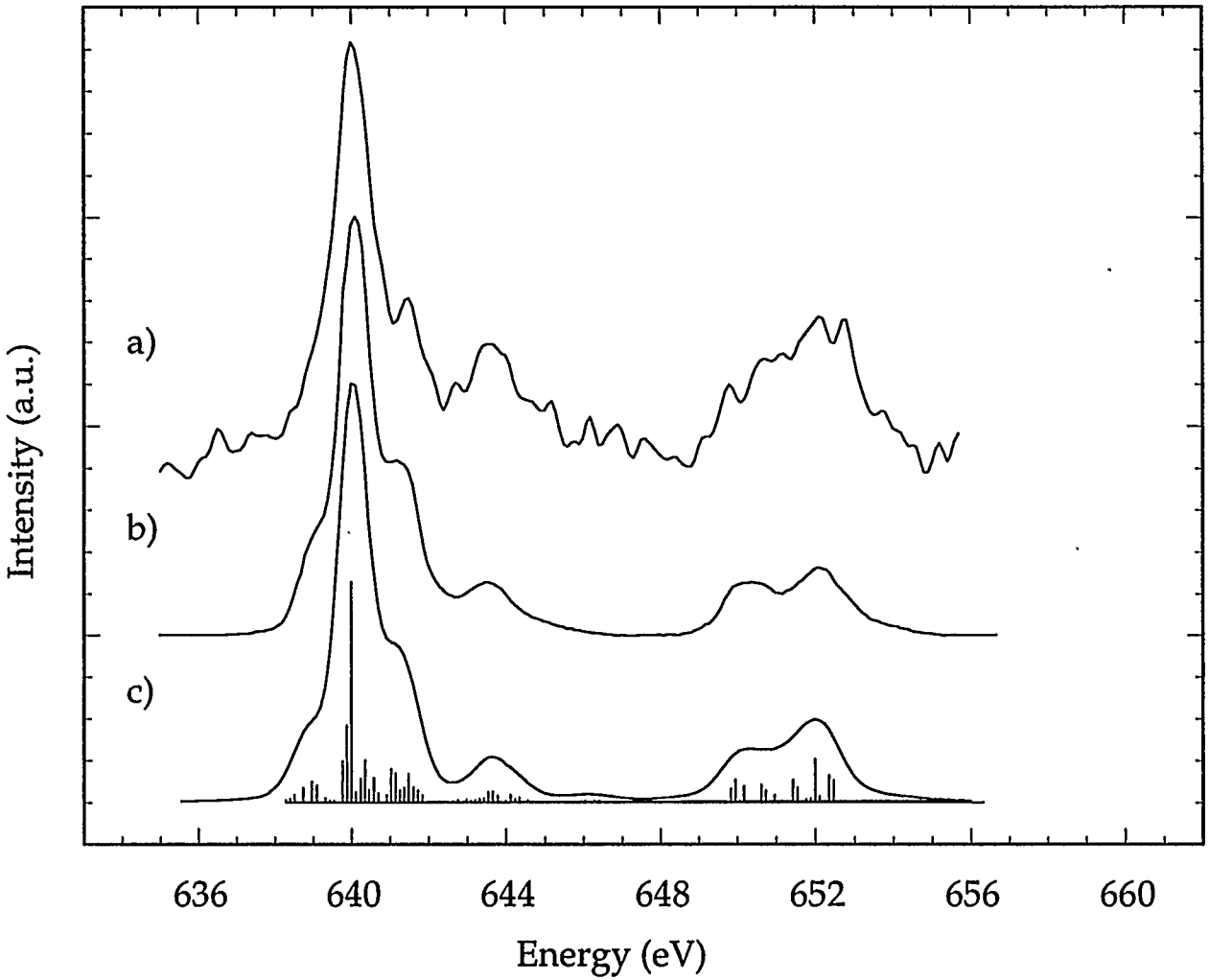
a)
b)
c)
Intensity (a.u.)
636
640
644
648
652
656
660
Energy (eV)

A series of atomic multiplet calculations with varying octahedral ligand field values were performed as previously described in Chapter 2, except that a Gaussian of 0.3 eV was used to account for the poorer resolution resulting from the use of 30 micron monochromator entrance and exit slits. A ligand field value of 0.80 eV gave the best agreement to the experimental spectrum (Figure 4.2). As Mn L-edges have been shown to yield ligand field values ~25% smaller than those obtained from UV-vis spectroscopy (Cramer et al., 1991), this result corresponds to an optical 10Dq value of 1.1 eV. This number is consistent with predominately nitrogen and oxygen coordination to the Mn (Jorgensen, 1971). The similarities between the protein data and that from $[Mn_4(2\text{-}OHpicpn)_4](ClO_4)_4$ suggest that this is a reasonable model for the Mn in reduced catalase. The spectra rule out extreme cases such as tetrahedral Mn or sulfur ligation. Modest covalent character due to predominantly nitrogen and oxygen ligation is in agreement with current EXAFS results on reduced Mn catalase which suggest 2-4 imidazoles per Mn and possible bridging ligands of either $(\mu\text{-carboxylato})_n$ or $(\mu\text{-OH})(\mu\text{-carboxylato})_n$, where n=1-3 (Waldo et al., 1991; Waldo et al., 1992).

Figure 4.3 presents the spectrum of super-oxidized Mn catalase. The L_{III} peak occurs ~2 eV higher in energy than in the reduced form and the energy separation between the L_{III} and L_{II} is again ~12 eV. The Mn(II)Mn(II) protein spectrum is much sharper and has more intense L_{III} transitions than those associated with the broad spectrum obtained from the Mn(III)Mn(IV) form, as is expected. Also shown for comparison are $Mn_2O_2(OAc)Cl_2(bpy)_2$ and the results from the empirical mixed valence simulations. The super-oxidized spectrum represents 12 scans, 6 seconds per point and has been smoothed with a window of 0.5 eV.

Figure 4.3: Mn(III)Mn(IV) L-edge Absorption Spectra. From top to bottom: a) Mn(III)Mn(IV) catalase; b) $Mn_2O_2(OAc)Cl_2(bpy)_2$, a Mn(III)Mn(IV) dimer; c) Mn(III)Mn(IV) catalase which has been corrected to compensate for 8% photoreduction; d) empirical mixed valence simulation of the corrected Mn(III)Mn(IV) catalase; and e) Mn(III)Mn(IV) catalase which contains ~45% Mn(II) due to photoreduction.

a)
b)
c)
d)
e)
636
640
644
648
652
656
660
Energy (eV)
Intensity (a.u.)

Table 4.1: Mixed Valence Simulation Fitting Parameters

Catalase	Oxidation States	Fit Fraction	Energy Shift
Mn_2(III,IV) catalase	(III)(IV)	0.28 Mn(III)/total Mn	-0.62 eV(3+) -0.26 eV(4+)
Mn_2(III,IV) catalase (corrected for photoreduction)	(III)(IV)	0.36 Mn(III)/total Mn	+0.62 eV(3+) -0.17 eV(4+)

$Mn_2O_2(OAc)Cl_2(bpy)_2$ is a Mn(III)Mn(IV) dimer with octahedral coordination. This mixed valence dimer exhibits a broader spectrum than the divalent manganese, with the middle of the L_{III} region occuring at 642 eV and the L_{II} at 654 eV (Figure 4.3). The broad features of the Mn(III)Mn(IV) dimer are consistent with those from the super-oxidized Mn catalase.

The mixed valence simulation results obtained using the mixed valence simulation routine described in Chapter 2 are summarized in Table 4.1. The best fit to the original experimental spectrum of super-oxidized Mn catalase was found to be a Mn(III) to Mn(IV) ratio of $0.7 \pm 0.1 : 1.3 \pm 0.1$ (Figure 4.3). The energy shift of the Mn(IV) component was -0.26 eV, while that of the Mn(III) component was larger, at -0.62 eV. A simple explanation for these relatively large negative energy shifts is that even though care was taken to change the position of the protein frequently, some photoreduction by the x-ray beam occured.

Photoreduction is an important concern for soft x-ray experiments and has been observed in other proteins, such as blue copper proteins and iron rubredoxin (George et al., 1993; George et al., 1992). Figure 4.3 also shows a photoreduced Mn(III)Mn(IV) catalase sample which had been continuously

in the beam for ~8 hours. The main L_{III} feature at 640 eV in this spectrum is due to Mn(II) from centers which have been photoreduced. From the mixed valence simulation routines, it is estimated that on the order of 45% of the Mn has been photoreduced.

Upon subtraction of 8% Mn(II) from the original super-oxidized Mn catalase data, the correct ratio of 0.9 ± 0.1 Mn(III) to 1.1 ± 0.1 Mn(IV) is obtained from the simulation routines (Figure 4.3, Table 4.1). The relatively large energy shifts of the Mn(III) and Mn(IV) components towards each other (+0.62 eV and -0.17 eV) suggest that the Mn in superoxidized catalase is more delocalized than that in $Mn_2O_2(OAc)Cl_2(bpy)_2$.

This interpretation of a mixed valence fluorescence spectrum using a simulation routine based on spectra taken by electron yield shows the promise of the fluorescence L-edge technique as applied to dilute protein samples, in spite of recent evidence (deGroot et al., 1994) that there are minor differences between electron yield and fluorescence spectra. Future simulations taking into account these differences should help to narrow down the uncertainty in predictions using the mixed valence simulations presented here. However, for some applications, the current simulation routine is sufficient. For example, it should be possible to settle the question of whether the oxygen-evolving complex associated with Photosystem II in green plants and cyanobacteria consists of a tetramer of trivalent Mn or instead has the oxidation states of $Mn_2(III)Mn_2(IV)$ in the S_1 state. The difference between a fit fraction of 1 in the former case and 0.5 in the latter is very large compared to the internal error bars of ± 0.02 associated with this simulation routine (see Chapter 2).

With more efficient detectors, photoreduction should be less of a problem and obtaining Mn L-edge spectra on more dilute systems such as Photosystem II should be feasible.

Algood, G.S.; Perry, J.J. *J. Bacteriol.* **1986**, *168*, 563-567.

Baldwin, E. **1991** Ph.D thesis, University of North Carolina, Chapel Hill.

Barynin, V.V.; Grebenko, A.I. *Dokl. Akad. Nauk. SSSR* **1986**, *286*, 461-464.

Cramer, S.P.; deGroot, F.M.F.; Ma, Y.; Chen, C.T.; Sette, F.; Kipke, C.A.; Eichhorn, D.M.; Chan, M.K.; Armstrong, W.H.; Libby, E.; Christou, G.; Brooker, S.; McKee, V.; Mullins, O.C.; Fuggle, J.C. *J. Am. Chem. Soc.* **1991**, *113*, 7937-7940.

deGroot, F.; Arrio, M.A.; Sainctavit, P.; Cartier, C.; Chen, C.T. *Solid State Communications* **1994**, *92*, 991-995.

Dikanov, S.A.; Tsvetkov, Yu.D.; Khàngulov, S.V.; Gol'dfeld, M.G. *Dokl. Akad. Nauk SSSR* **1988**, *302*, 1255-1257.

George, S.J.; Lowery, M.D.; Solomon, E.I.; Cramer, S.P. *J. Amer. Chem. Soc.* **1993** *115*, 2968-2969.

George, S.J.; van Elp, J.; Chen, J.; Ma, Y.; Chen, C.T.; Park, J.-B.; Adams, M.W.W.; Searle, B.G.; deGroot, F.M.F.; Fuggle, J.C.; Cramer, S.P. *J. Amer. Chem. Soc.* **1992** *114*, 4426-4427.

Ivancich, A.; Barynin, V.V.; Zimmermann, J.-L. *Biochemistry* **1995**, *34*, 6628-6639.

Jorgensen, C.K. *Modern Aspects of Ligand Field Theory;* North-Holland Publishing Co.: Holland, 1971.

Karpenko, V.; Kinney, J.H.; Kulkarni, S.; Neufeld, K.; Poppe, C.; Tirsell, K.G.; Wong, J.; Cerino, J.; Troxel, T.; Yang, J.; Hoyer, E.; Green, M.; Humphries, D.; Marks, S.; Plate, D. *Rev. Sci. Instr.* **1989**, *60*, 1451-1456.

Kono, Y.; Fridovich, I. *J. Biol. Chem.* **1983**, *258*, 6015-6019.

Penner-Hahn, J.E. "Structural Properties of the Mn site in the Mn Catalases," in *Mn Redox Enzymes* ; Pecoraro, V.L., Ed., VCH Publishers: New York, 1992.

Randall, K.J.; Eberhardt, W.; Feldhaus, J.; Erlebach, W.; Bradshaw, A.M.; Xu, Z.; Johnson, P.D.; Ma, Y. *Nucl. Instr. and Meth A* **1992**, *319*, 1-3:101-105.

Stemmler, T.L.; Sturgeon, B.E.; Randall, D.W.; Britt, R.D.; Penner-Hahn, J.E., manuscript in preparation.

Waldo, G.S.; Fronko, R.M.; Penner-Hahn, J.E. *Biochemistry* **1991**, *30*, 10486-10490.

Waldo, G.S.; Yu, S.Y.; Penner-Hahn, J.E.*J. Am. Chem. Soc.* **1992**, *114*, 5869-5870.

The four electron oxidation of water is linked to the one electron light induced charge separation of Photosystem II (PSII) by a tetrameric Mn cluster, called the oxygen evolving complex (OEC). The OEC cycles through a series of "S_n" states, where n represents the number of oxidizing equivalents that have been accumulated. Once the S_4 state is reached, molecular oxygen is released and the OEC returns to the S_0 state (Figure 5.1).

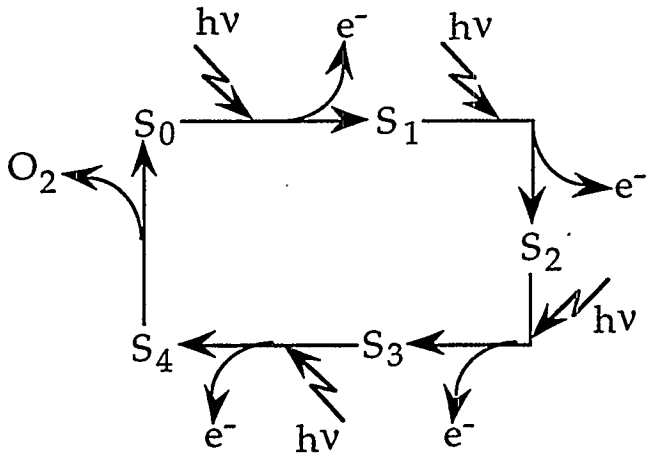

Figure 5.1: The Kok Cycle (Kok et. al, 1970).

A recent structural model for the OEC has been presented by the Klein group and is shown in Figure 5.2 (Yachandra et al., 1993).

The Mn Oxidation States in S_1

Much effort has been spent in trying to decipher the oxidation states of the four Mn. So far, however, definitive assignments have not yet been made.

XANES studies indicate that the average oxidation state of the Mn in

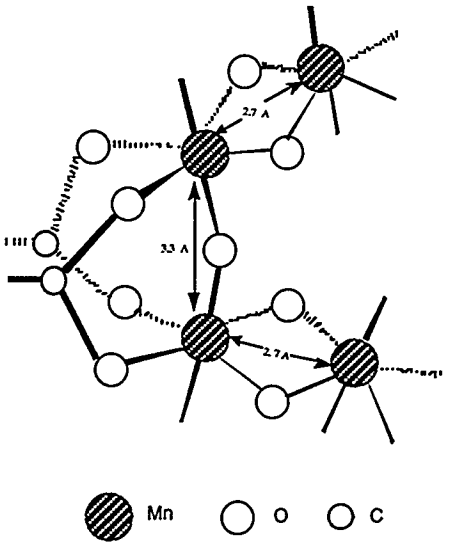

Figure 5.2: A Structural Model for the Oxygen-Evolving Complex.

the S_1 state is Mn(III) (Kirby et al., 1981; Kusunoki et al., 1990; Penner-Hahn et al., 1990). This is in agreement with microwave power saturation studies (Styring et al., 1988), nuclear magnetic resonance (NMR) relaxation enhancement measurements (Srinivasan et al., 1986a; Srinivasan et al., 1986b), and spin-lattice relaxation time measurements (Evelo et al., 1989). Mn oxidation states of $(III)_4$ are also suggested as a better match for the pre-edge features in Mn K-edges of the S_1 state (Kusunoki et al., 1991). Simulations of the multiline EPR signal in the S_2 state indicate oxidation states of $Mn(III)_3Mn(IV)$ which would agree with an assignment of $Mn(III)_4$ for the S_1 state (Zheng et al., 1992). Similarity of the XANES from S_1, S_2, and S_3 states rules out any Mn(II) in the S_1 state as an oxidation from Mn(II) to Mn(III) would cause significant structural changes in the Mn coordination sphere (Sauer et al., 1992).

Second derivatives of XANES spectra taken in the Klein group (Yachandra et al., 1993) are reproduced somewhat better by simulations using

a mixed valence $(III)_2(IV)_2$ tetramer. Data from the Penner-Hahn lab is in agreement with an assignment of $(III)_2(IV)_2$ (Riggs et al., 1992). The parallel polarization EPR signal from Bill Armstrong's $(III)_2(IV)_2$ "dimer of dimers" (Chan et al., 1991) qualitatively resembles the signal reported once from the S_1 state of the OEC by the Klein group (Dexheimer et al., 1992). Bond valence sums which assume the average Mn-O distance is 1.91Å, that there are 1-2 nitrogen atoms, and that the average Mn-O distance does not change from S_1 to S_2, predict a mixed valence tetramer with a homovalent Mn(III) tetramer being inconsistent (Thorp, 1992).

In summary, there is evidence supporting both oxidation state assignments of $(III)_2(IV)_2$ and $(III)_4$. For a more in-depth analysis of the various arguments supporting both oxidation state possibilities, as well as descriptions of the other S states, the reader is referred to comprehensive review articles (Debus, 1992; Rutherford et al., 1992). Conclusive assignment of the Mn oxidation states in the various S-states should be possible from examination of the Mn L-edge XANES. As L-edges have much better resolution than K-edges (Chapter 2), deciphering the mixtures of oxidation states is more straightforward and has been demonstrated using both model compounds and Mn catalase (Chapters 2 and 4).

Mn L-edge Experiments

KM particles (Kuwabara et al., 1982) were isolated from spinach leaves by A. Rompel in the M.P. Klein lab (University of California, Berkeley). Help with sample preparation and characterization was provided by H. Visser, also in the Klein laboratory. The pellet was unfrozen, resuspended in sucrose buffer, and centrifuged. It was then resuspended to a consistency which was viscous but still pipettable (~5.9 mg Chl/ml with a Chl a/Chl b ratio of 2.5). Al

strips which were thin enough to fit into an EPR cryostat were affixed to a Cu sample holder with double sided sticky tape which had been previously determined to be free of EPR-detectable transition metal contamination. Two 50 µl portions of Photosystem II were deposited onto an area of ~1.69 cm^2. Each layer was allowed to dry for several hours in a 4 °C cold room under a flow of nitrogen gas. Following dark adaptation, the sample holder was slowly frozen in liquid nitrogen. EPR sample holders containing similar amounts of PSII were also prepared in the same manner.

Traditionally, our group has made L-edge samples by depositing thin films of purified protein on Si wafers. However, proteins often do not adhere well to this surface. When the protein studied is a concentrated Fe-S cluster, it is sometimes possible to locate the single speck of remaining film and record the spectrum quickly enough to avoid photodamage of the sample. With Photosystem II, another alternative was needed. Si wafers were first chosen because of the flat, clean surface, in addition to the availability. It is, however, an insulator and thus is not desirable due to the bad thermal contact obtained between the Si and the liquid helium cold finger. Industrial grade Al foil was found to be a good alternative to the Si as it is flat, does not have a large EPR background, and is a good thermal conductor. More importantly, Photosystem II films adhere reasonably well to the Al and generate multiline signals when illuminated to the S_2 state.

Transferring the L-edge sample holder from liquid nitrogen to the liquid helium cold finger inside our L-edge chamber also required some special adaptations to previous methods. Typically, a sample is placed in the load lock where it is pumped on by a turbo pump station for approximately 20 minutes until achieving pressures in the low 10^{-6} range or better. It is then transferred to the cold finger inside the UHV chamber. The three special

concerns for loading the PSII were: 1) to keep the sample dark, 2) to avoid frost buildup on the surface of the PSII which would greatly cut down on photon flux both going into and coming out of the sample, and 3) to avoid (or at least minimize) lyophilizing the sample by only pumping on it while it was frozen. To accomplish these objectives, 1) all manipulations of the sample were carried out under black cloth and with a green flashlight, 2) the sample was transferred from liquid nitrogen to the load lock inside a nitrogen-filled glove bag, and 3) immediately after being placed on the load lock, the sample was attached to a home built sample preparation chamber which was at liquid nitrogen temperatures. The sample preparation chamber consisted of a copper cold finger through which liquid nitrogen was flowing. After the sample was attached to this cold finger, it was then pumped on until the pressure was sufficiently low that it could be inserted into the main chamber. Photosystem II samples were maintained at a temperature of ~14 K inside the chamber with a Janis cryostat.

X-ray spectra were obtained on undulator Beamline 7.0 at the Advanced Light Source (Warwick et al., 1995). The beamline monochromator slits were set at 30 microns, resulting in the energy resolution of the beamline being ~0.15 eV. After approximately 8 hours of collecting data, changing the sample position regularly to minimize photoreduction, the three working detector channels were summed and linear backgrounds were subtracted from the resulting spectrum. The preliminary Mn L-edge data from Photosystem II are presented in Figure 5.3. The chemical shift series from Chapter 2 is again presented for easier examination of the Photosystem II spectrum. In spite of the spectrum being very noisy, there is a hint of a Mn L-edge spectrum, most noticably in the L_{III} region.

Figure 5.3: Mn L-edge spectrum of Photosystem II. From top to bottom: Photosystem II raw data (solid line); homovalent Mn(II) (dotted line), Mn(III) (solid line), and Mn(IV) (dotted and dashed line) spectra. The L_{III} edge of the Mn(II) spectrum has been multiplied by 0.5 for easier comparison with the other spectra.

Intensity (a.u.)
636
640
644
648
652
656
660
Energy (eV)

Prognosis

Although encouraged by this result, it was decided not to signal average any longer as the improvement in the signal to noise ratio is proportional to the square root of the number of scans - i.e. to improve the signal by a factor of 10 would require a 100 times more scans, or about a month of data collection!

Clearly, improvements need to be made before this is a viable experiment. As this data was collected on an undulator beamline at the ALS, a third generation synchrotron source, significant improvements in photon flux are not expected in the near future. And, given the fast rates of photo-damage seen in other samples during this beamtime, they are not necessarily desirable, either. An increase in the number of detector channels would significantly reduce the amount of time for data collection. What would have taken a month with only three detector channels would become about a week if all thirteen channels were working. If delivery of a new 30+ element detector is ever realized, it would allow the Mn oxidation states in the OEC to be probed by L-edge absorbtion spectroscopy by further reducing the time necessary for signal averaging to about 3 days - a slow but feasible and worthwhile experiment.

Chan, M.K.; Armstrong, W.H. *J. Am. Chem. Soc.* **1991** *113*, 5055-5057.

Debus, R.J. *Biochim. Biophys. Acta* **1992** *1102*, 269-352.

Dexheimer, S.L.; Klein, M.P. *J. Am. Chem. Soc.* **1992** *114*, 2821-2826.

Evelo, R.G.; Styring, S.; Rutherford, A.W.; Hoff, A.J. *Biochim. Biophys. Acta* **1989** *973*, 428-442.

Kirby, J.A.; Goodin, D.B.; Wydrynski, T.; Robertson, A.S.; Klein, M.P. *J. Am. Chem. Soc.* **1981** *103*, 5537-5542.

Kok, B., Forbush, B.; McGloin, M. *Photochem. Photobiol.* **1970** *11*, 457-476.

Kusunoki, M.; Ono, T.-A.; Matsushita, T.; Oyanagi, H.; Inoue, Y. *J. Biochem.* **1990** *108*, 560-567.

Kusunoki, M.; Ono, T.; Inoue, Y.; Suzuki, M.; Uehara, A.; Matsushita, T.; Oyanagi, H. "Mn K-edge XANES Spectroscopy for water-splitting Mn-enzyme in photosynthesis. High quality pre-edge features in the S_1 and S_2 states." in *X-ray Absorption Fine Structure*; Hasnain, S.S., Ed., Ellis Horwood Limited: West Sussex, 1991, pp. 174-177.

Kuwabara, T.; Murata, N. *Plant Cell Physiol.* **1982** *23*, 533-539.

Penner-Hahn, J.E.; Fronko, R.M.; Pecoraro, V.L.; Yocum, C.F.; Betts, S.D.; Bowlby, N.R. *J. Am. Chem. Soc.* **1990** *112*, 2549-2557.

Riggs, P.J.; Mei, R.; Yocum, C.F.; Penner-Hahn, J.E. *J. Am. Chem. Soc.* **1992** *114*, 10650-10651.

Rutherford, A.W.; Zimmermann, J.-L.; Boussac, A. "Oxygen Evolution" in *The Photosystems: Structure, Function and Molecular Biology* , Barber,J., Ed., Elsevier Science: Amsterdam, 1992, pp. 179-229.

Sauer, K.; Yachandra, V.K.; Britt, R.D.; Klein, M.P. in *Mn Redox Enzymes* ; Pecoraro, V.L., Ed., VCH Publishers: New York, 1992, pp. 141-175.

Srinivasan, A.N.; Sharp, R.R. *Biochim. Biophys. Acta* **1986a** *851*, 369-376.

Srinivasan, A.N.; Sharp, R.R. *Biochim. Biophys. Acta* **1986b** *850*, 211-217.

Styring, S.A.; Rutherford, A.W. *Biochem.* **1988** *27*, 4915-4923.

Thorp, H.H. *Inorg Chem.* **1992** *31*, 1585-1588.

Warwick, T.; Heimann, P.; Mossessian, D.; McKinney, W, Padmore, H.*Rev. Sci. Inst.* **1995** *66*, 2037-2040.

Yachandra, V.K.; DeRose, V.J.; Latimer, M.J.; Mukerji, I.; Sauer, K.; Klein, M.P. *Science* **1993** *260*, 675-679.

Zheng, M.; Dismukes, G.C. "Photosynthetic water oxidation: What have we learned from the multiline EPR signals?" in *Research in Photosynthesis*, Murata, N., Ed., Kluwer Academic Publishing: Dordrecht, 1992, pp. 305-308.

Chapter 6: The Oxygen-Evolving Complex II - High Resolution Fluorescence Experiments

Photosystem II core particles (PSII) were isolated from spinach by P.S. DeMarois in the J.E. Penner-Hahn lab (University of Michigan) as has been previously described (Ghanotakis et al., 1986; Ghanotakis et al., 1987). These preparations differ from other PSII preparations only in the composition of the extrinsic polypeptides. The PSII was dark adapted for half an hour at 4 °C in order to trap the S_1 state (Styring et al., 1987). Reduced S state samples were prepared by incubating the S_1 particles with 200 mM hydroquinone for half an hour, removing the excess reductant by 40-fold dilution, and treating with ferricyanide to oxidize excess hydroquinone. The protein samples were placed in gold-plated copper sample holders with a depth of ~2 mm and maintained at 8 ± 1 K with a Displex He refrigerator during x-ray exposure.

The Mn high resolution fluorescence spectra of Photosystem II were recorded on NSLS Beamline X25 (Berman et al., 1992) using either a Si(220) or Si(111) excitation monochromator and an array of spherically bent Si(440) fluorescence analyzers (Chapter 3). Kβ emission spectra of the S_1 state were also measured on SSRL Beamline 6-2 (Hoyer et al., 1983) using Si(111) monochromator crystals and the same Si(440) fluorescence analyzers. Spectra were measured, calibrated, and reduced as described in Chapter 3. It was necessary to subtract a linear background from the reduced Photosystem II Kβ data. PSII XANES spectra were smoothed over a 15 point range which corresponded to a 1.5 eV window at the edge. It was necessary to subtract linear backgrounds from the PSII XANES spectra before normalization, as will be illustrated.

Photosystem II in the S_1 state

The Kβ emission spectrum of Photosystem II particles poised in the S_1 state is presented in Figure 6.1. Also shown for comparison are Mn model compounds with Mn oxidation states ranging from Mn(II)Mn(III) through Mn(IV) (Figure 6.1). As it is hard to determine by eye whether $Mn(III)_4O_3Cl(O_2CMe)_3(dbm)_3$ or $Mn(III)Mn(IV)O_2(O_2CMe)Cl_2(bpy)_2$ is a better oxidation state model for Photosystem II, a χ^2 quality of fit parameter was calculated for each of the spectra in Figure 6.1, as is summarized in Table 6.1. Quantitatively, the S_1 spectrum is best modeled by $Mn(III)Mn(IV)O_2(O_2CMe)Cl_2(bpy)_2$.

Using a value of 6490.31 eV for the Photosystem II Kβ peak and the correlation between Kβ peak energy and oxidation state (Chapter 3), an oxidation state prediction of 3.5 ± 0.3 was obtained. For a tetramer, an average oxidation state of 3.5 ± 0.3 corresponds to complexes with between 0.8 and 3.2 Mn(IV)s, ruling out an oxidation state assignment of $Mn(III)_4$ for the S_1 state. A mixed valence $Mn(III)_2Mn(IV)_2$ tetramer would be consistent with the Kβ emission data.

This mixed valence oxidation state assignment suggests that Photosystem II in the S_1 state would be a good candidate for site-selective XAS. By selectively monitoring the detection energy, both XANES and EXAFS can be obtained which are predominately from only Mn(III) or Mn(IV) species. This would allow a more specific probe of the different Mn environments within the OEC than has previously been possible using conventional XAS.

By recording the Mn K-edge absorption spectrum at 6488.6 and 6491.9 eV, fluorescence energies more favorable to higher and lower oxidation state detection, respectively, the site-selective XANES on Photosystem II in the

Figure 6.1: Kβ Emission Spectrum of Photosystem II in the Resting State, S_1, versus Mn(II)Mn(III), Mn(III), Mn(III)Mn(IV), and Mn(IV) models. Top to bottom: S_1 (dotted line) and Mn(II)Mn(III)biphen$_2$(biphenH)(bipy)$_2$ (solid line); S_1 (dotted line) and Mn(III)$_4$O$_3$Cl(O$_2$CMe)$_3$(dbm)$_3$ (solid line); S_1 (dotted line) and Mn(III)Mn(IV)O$_2$(O$_2$CMe)Cl$_2$(bpy)$_2$ (solid line); S_1 (dotted line) and Mn(IV)$_2$O$_2$(O$_2$Ac)$_2$(bpy)$_2$ClO$_4$ (solid line).

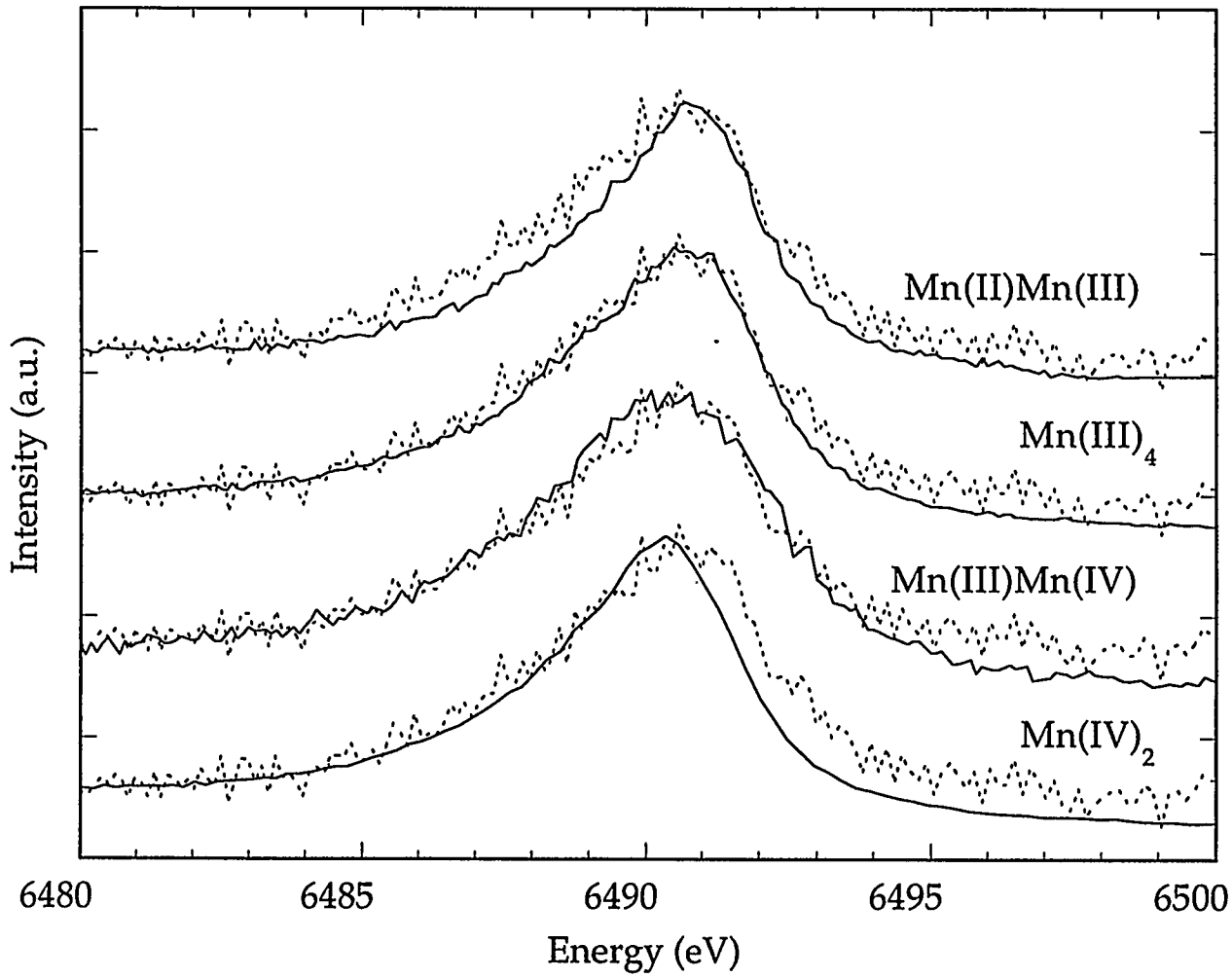
Intensity (a.u.)
Mn(II)Mn(III)
Mn(III)$_4$
Mn(III)Mn(IV)
Mn(IV)$_2$
6480
6485
6490
6495
6500
Energy (eV)

Table 6.1: Quality of fit for the Kβ emission spectrum of Photosystem II in the S_1 state using Mn model compounds. An energy range of 6485-6495 eV was used for the least-squares determination.

Model Compound	Average Mn Oxidation State	χ^2
$Mn_2biphen_2(biphenH)(bipy)_2$	2.5	1.25
$Mn_4O_3Cl(O_2CMe)_3(dbm)_3$	3.0	1.14
$Mn_2O_2(O_2CMe)Cl_2(bpy)_2$	3.5	0.48
$Mn_2O_2(O_2Ac)_2(bpy)_2ClO_4$	4.0	1.84

$$\chi^2 = \Sigma(Intensity_{(model)} - Intensity_{(PSII)})^2$$

resting state was measured. A serious background problem was encountered and is presented in Figure 6.2. An almost identical background is observed for Photosystem II preparations in other S states, regardless of the angle of the analyzers (detection energy). The origin of this signal has yet to be fully understood although a somewhat similar background was also observed for a frozen sucrose solution (Figure 6.2). The sharp peak at the low energy end of the spectrum occurs when the elastic scatter energy matches the energy of detection. Linear backgrounds fit to both the pre-edge and EXAFS regions were subtracted from the spectra in order to extract the XANES which were then smoothed over a 5 point interval, corresponding to a 0.15 eV range at the edge.

The site-selective XANES spectra obtained in this manner are presented in Figure 6.3. The overall shape of the two edges is very similar, as seen with site-selective XANES on Mn model compounds which do not contain Mn(II) (Chapter 3, Figure 3.7). The main difference between these spectra occurs in the pre-edge region where the higher oxidation state-

Figure 6.2: The Background Problem in Site-Selective XANES of Photosystem II. From top to bottom: raw XANES data of Photosystem II in the S_1 state (solid line) and a frozen sucrose solution (dotted line). The PSII spectrum has been divided by a factor of 5 in order to compare with the sucrose solution on an equal number of I_0 counts per data point basis.

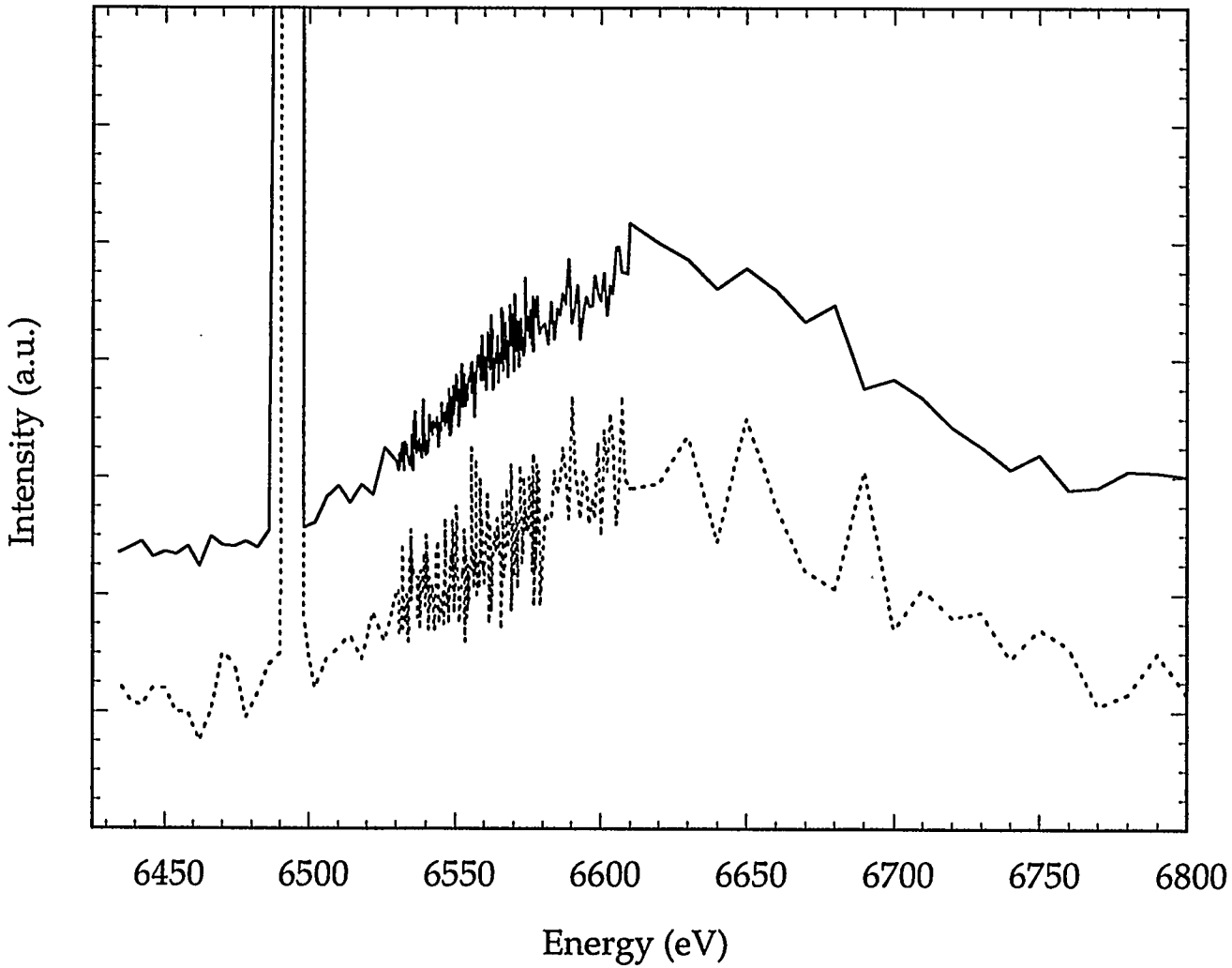
Intensity (a.u.)
6450
6500
6550
6600
6650
6700
6750
6800
Energy (eV)

Figure 6.3: Site-Selective XANES of Photosystem II in the S_1 state. The XANES obtained by detection at higher fluorescence energies which are favorable to lower oxidation state(s) (solid line) and lower fluorescence energies which are favorable to higher oxidation state(s) (dotted line).

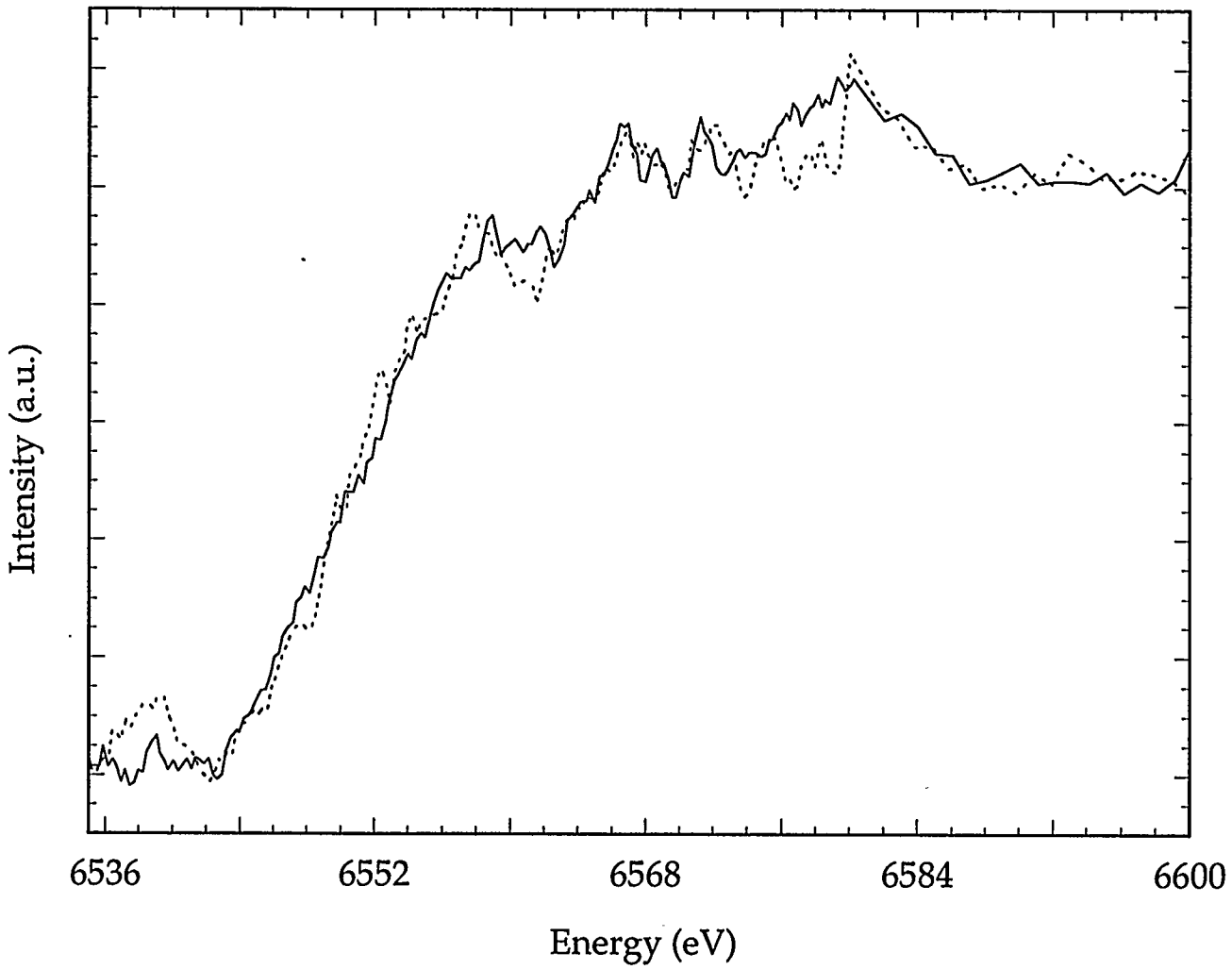
Intensity (a.u.)
6536
6552
6568
6584
6600
Energy (eV)

detected spectrum has a more intense 1s to 3d feature than the lower oxidation state-detected spectrum. This is consistent with pre-edge effects seen in the chemical shift series presented in Figure 1.2 (Chapter 1).

Reduced Photosystem II

Photoactivation of the OEC is believed to occur in several steps: a ligated Mn^{2+} is photooxidized to an unstable Mn^{3+} intermediate, following which another Mn^{2+} can be incorporated into the complex. Photooxidation converts this unstable Mn(II)Mn(III) intermediate to a stable Mn(III)Mn(III) dimer. Two more Mn^{2+} then spontaneously complete the assembly of the reduced precursor to the OEC (Debus, 1992 and references therein).

Active PSII samples poised in the S_1 state can be chemically reduced by incubation with hydroquinone (PSII-HQ). This reduced state has been proposed as a potential model for an intermediate in the photoactivation process (Riggs-Gelasco et al., 1996). XANES (Riggs et al., 1992) and EPR (Mei et al., 1992) studies on PSII-HQ show that this reduced state contains roughly 50 % Mn(II) and that the effect of hydroquinone on the PSII is photoreversible. EXAFS experiments on PSII-HQ show significant structural rearrangement of the Mn complex, however, interpretation of the changes are difficult as conventional EXAFS averages over all Mn environments in the sample. Site-selective EXAFS would be a sensitive probe of this system, allowing the extraction of information about only the Mn(II) sites and leading to a deeper understanding of the effects of hydroquinone on PSII preparations.

The Kβ emission spectrum of Photosystem II particles poised in a chemically reduced S state by treatment with hydroquinone is presented in Figure 6.4. Mn model compounds with Mn oxidation states of Mn(II) and Mn(II)Mn(III) are also shown in this figure. Qualitatively, the PSII-HQ

spectrum resembles the spectrum of $Mn(II)(acac)_2$ much more than that from the mixed valence $Mn_2(II,III)(biphen)_2(biphenH)(bipy)_2$. The Kβ peak of the reduced Photosystem II was assigned a value of 6491.28 eV. Using the Kβ peak energy and average oxidation state correlation, this corresponds to an average Mn oxidation state of 2.1 ± 0.3, suggesting that the Mn in this sample was predominantly Mn(II).

Site-selective XANES on PSII-HQ were measured by detecting the Mn K-edge absorption spectrum at 6488.5 and 6493.1 eV, energies more favorable to higher and lower oxidation state detection, respectively. The data was reduced in the same manner as that described for the XANES from PSII in the S_1 state. The resulting spectra are presented in Figure 6.5 and, even though the noise level is quite high, the spectra are obviously different. The spectrum obtained using lower oxidation state detection qualitatively resembles that from Mn(II) species - note the sharp peak around 6552 eV and compare with Figure 3.7 (Chapter 3) - while it is absent from the XANES which probe predominately higher oxidation states. This is very promising as it indicates the possibility of recording site-selective spectra on reduced Photosystem II.

Photoreduction

Photodamage is, as always in x-ray studies on metalloproteins, a concern. Through trial and error, it has been possible to learn how sensitive Photosystem II is to photodamage and to compensate for this effect during data collection. The PSII data presented in this chapter were obtained by taking care to switch to a fresh spot on the sample at least once an hour. On samples which were exposed for 3-4 hours per spot, photoreduction of

Figure 6.4: Kβ Emission Spectrum of Photosystem II in a Chemically Induced Reduced State versus Mn(II) and Mn(II)Mn(III) models. Top to bottom: PSII-HQ (dotted line) and $Mn(II)(acac)_2$ (solid line); PSII-HQ (dotted line) and $Mn_2(II,III)(biphen)_2(biphenH)(bipy)_2$ (solid line).

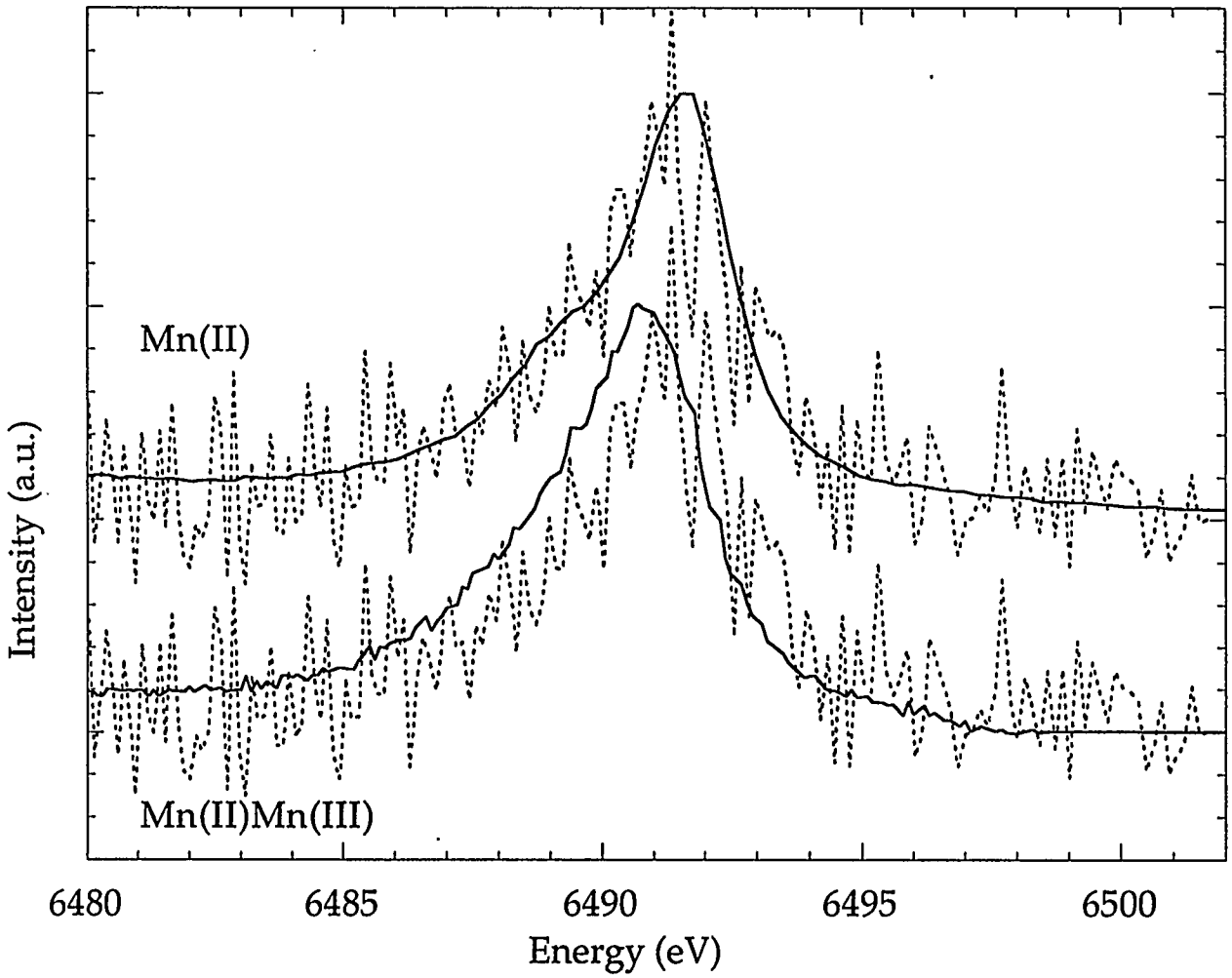
Mn(II)
Mn(II)Mn(III)
Intensity (a.u.)
6480
6485
6490
6495
6500
Energy (eV)

Figure 6.5: Site-Selective XANES of Photosystem II in a Reduced State. The PSII-HQ XANES obtained by detection at higher fluorescence energies which are favorable to lower oxidation state(s) (solid line) and lower fluorescence energies which are favorable to higher oxidation state(s) (dotted line).

Intensity (a.u.)
6536
6552
6568
6584
6600
Energy (eV)

Photosystem II originally poised in the S_1 state is apparent, as is illustrated in the Mn Kβ spectra presented in Figure 6.6.

Prognosis

These results are promising as they indicate that, once signal intensity-related problems can be overcome, it should be possible to record site-selective spectra of Photosystem II. However, before site-selective XANES experiments on Photosystem II can be quantitatively analyzed, improvement in signal to noise must be made. Each of the XANES protein spectra presented earlier represents about 4 hours of successful data collection (and at least 8 hours of set-up, alignment, and tweaking of the experiment). In order to have any hope of extracting quantitative information from this data, an improvement in the signal to noise of the spectra on the order of a factor of 10 must be made. Using the experimental set-up of January, 1996, good quality XANES of Photosystem II would require roughly 17 days of good data collection - more than a month for a site-selective XANES experiment using two different detection energies.

Only ~190 counts were obtained for the PSII samples in 4 hours of signal averaging above the edge. The amplitude of EXAFS oscillations are only a few percent of the edge jump. Assuming that a signal to noise ratio for the EXAFS of at least 5 is necessary for analyzable data, acquiring satisfactory statistics for EXAFS analysis would require ~7.4×10^4 signal counts per point, corresponding to more than 2 months of data collection (and truckloads of spinach) for each detection energy!

Clearly, signal averaging will not solve the signal to noise problems and improvements in the experiment need to be made before site-selective XANES and EXAFS on Photosystem II becomes a useful tool. A factor of 50

Figure 6.6: Photoreduction of Photosystem II. Photosystem II in the S_1 state (solid line) and Photosystem II originally poised in the resting state which has been Photoreduced (dotted line).

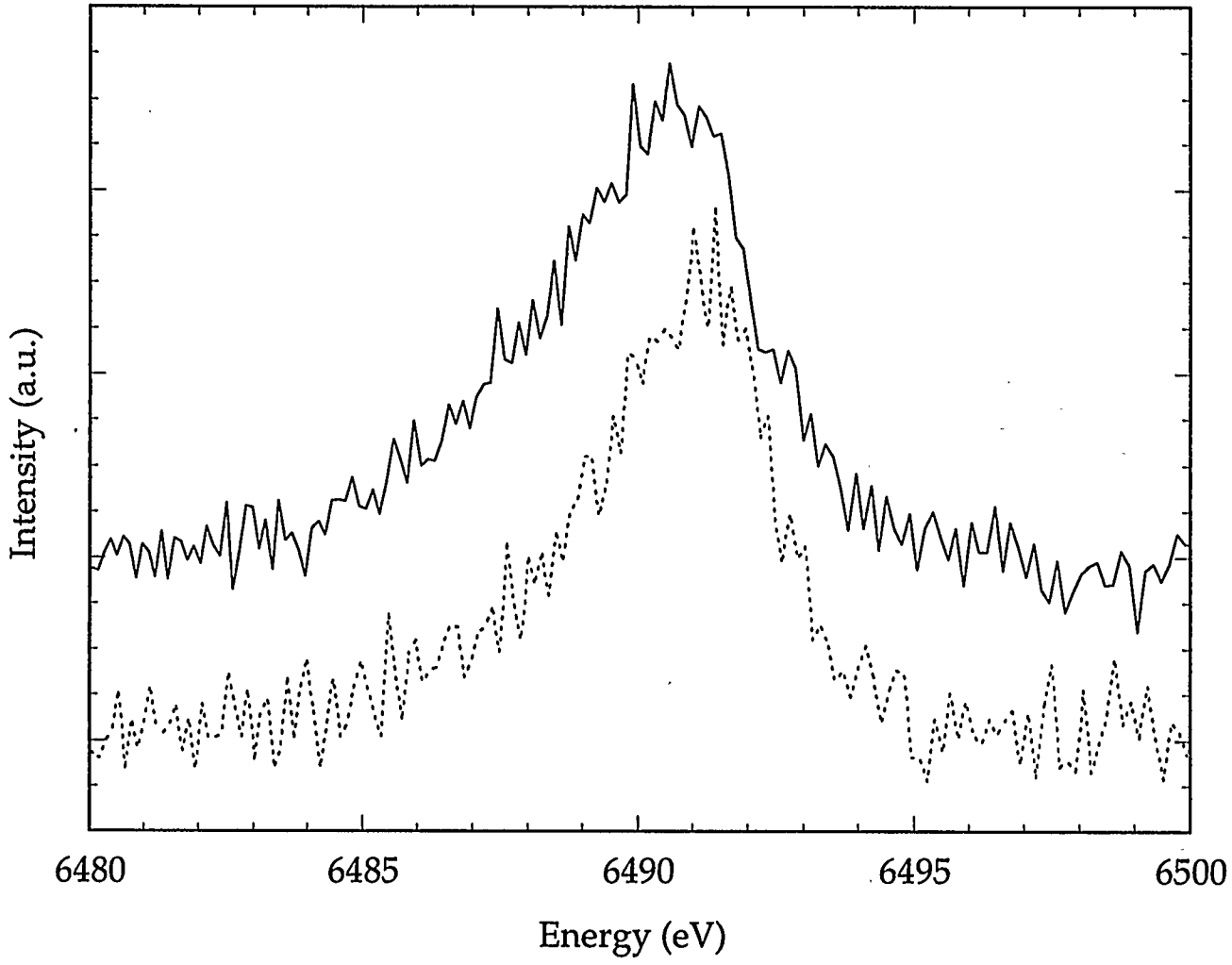
Intensity (a.u.)
6480
6485
6490
6495
6500
Energy (eV)

in improvement would make XANES a practical experiment - at about 8 hours an edge, and EXAFS an undertaking for the truly adventurous - requiring roughly 31 hours of usable data for each EXAFS spectrum.

The XANES data was collected on X25, a high brightness beamline with on the order of 10^{12} photons/s focussed to an ~1 x 2 mm spot. Although some improvements in flux may be made in new beamlines being constructed at third generation synchrotron sources, they will not necessarily be advantageous to this experiment due to the current photoreduction problems.

A spectrometer upgrade was recently completed (March, 1996, see Table 6.2). Much of the air path in the experiment was eliminated by using custom-built helium paths. The number and thickness of windows was also reduced as much as possible. These improvements decrease the flux attenuation by a factor of 4.4. Further reduction of losses due to the window material is difficult as the windows must be thick enough to contain an ~6 torr vacuum. One possibility for further improvement would be to eliminate the vacuum path and instead immerse the entire experiment in a helium atmosphere, gaining ~1.4 times the flux as compared to the March 1996 experimental set-up. This will also increase the amount of scattered radiation, however, as the current background is virtually zero (≤3 counts/s), this may not be a great concern.

By arranging the crystals as close to each other as possible, the amount of dead space needed between the analyzers for the crystal supports and the motors which scan theta is reduced to ~2 inches. The amount of surface area exposed to fluorescence is compared for various sizes of crystals in Table 6.3. Using two 6 inch crystals instead of the current four 2 inch crystals would further improve the count rate by a factor of ~4.5. Depending on the spherical

Table 6.2: Attenuation of flux in the Si(440) spectrometer.

	Flux Attenuator	Transmitted Intensity
January 1996	254 μ Kapton	0.70
	762000 μ air path	0.24
	vacuum path	0.98
		total = 0.16
March 1996	152 μ Kapton	0.81
	19 μ Polypropylene	0.99
	50800 μ air	0.91
	711200 μ helium	0.996
	vacuum path	0.98
		total = 0.71
Future	2438400 μ helium	total = 0.99

Table 6.3: Usable surface area of the Si(440) analyzers. Calculations assume an arc ~16 inches long for positioning the analyzers, with the sample holder blocking the rest of the fluorescence. Approximately 2 inches is required between adjacent crystals for the crystal supports and the motors.

Number and size of Crystals Area(in^2)	Surface Area (in^2)/Crstal	Total
4 - 2" diameter crystals	3.1	12.6
3 - 4" diameter crystals	12.6	37.7
2 - 6" diameter crystals	28.3	56.5

abberations in the larger crystals, increasing the size of the analyzer crystals may, however, result in a trade-off between loss of resolution and count rate improvement.

Immersing the experiment in a helium atmosphere and increasing the size of the analyzer crystals should result in an ~28-fold improvement in flux. This should allow the obtainment of site-selective XANES on systems as dilute as Photosystem II. Good quality XANES of PSII using two different detection energies should be obtainable in a little over a day of data collection. The technique of site-selective EXAFS has the potential to be invaluable in the attainment of information about specific Mn environments in catalytic cycles. However, until count rate capabilities are further improved, site-selective EXAFS will most likely not become a routine probe of Photosystem II.

There remain, however, many systems to which the advantages of site-selective EXAFS can be applied with the experimental sensitivity available in the near future. Examples of Mn-containing systems which could benefit from this technique are catalase, $Li_xMn_2O_4$ batteries, and magnetoresistance materials.

Berman, L.E. ; Hastings, J.B.; Oversluizen, T.; Woodle, M. *Rev. Sci. Instrum.* **1992** *63*, 428-432.

Ghanotakis, D.F.; Yocum, C.F. *FEBS Lett.* **1986** *197*, 244.

Ghanotakis, D.F.; Demetriou, D.M.; Yocum, C.F. *Biochim. Biophys. Acta* **1987** *891*, 15-21.

Hoyer, E.; Bahr, C.; Chan, T.; Chin, J.; Elioff, T.; Halbach, K.; Harnett, G.; Humphries, D.; Hunt, D.; Kim, K.-J.; Lauritzen, T.; Lindel, D.; Shirley, D.; Tafelski, R.; Thompson, A.; Cramer, S.; Eisenberger, P.; Hewitt, R.; Stöhr, J.; Boyce, R.; Brown, G.; Golde, A.; Gould, R.; Hower, N.; Lindau, I.; Winick, H.; Yang, J.; Harris, J.; Scott, B. *Nucl. Inst. & Meth.* **1983**, *208*, 117-125.

Mei, R.; Yocum, C.F. *Biochemistry* **1992** *31*, 8449-8454.

Riggs, P.J.; Mei, R.; Yocum, C.F.; Penner-Hahn, J.E. *J. Am. Chem. Soc.* **1992** *114*, 10650-10651.

Riggs-Gelasco, P.J.; Mei, R.; Yocum, C.F.; Penner-Hahn, J.E. *J. Am. Chem. Soc.* **1996** *118*, 2387-2399.

Styring, S.; Rutherford, A.W. *Biochemistry* **1987** *26*, 2401-2405.

Chapter 7: The Oxygen-Evolving Complex III - Search For a Better Method of Determining if Calcium is Near the Manganese Cluster

Both calcium and chloride are necessary cofactors for oxygen evolution in Photosystem II. Though not for lack of effort, the location of the 2-3 calcium binding sites associated with the PSII, as well as their possible role in oxygen evolution, remains unclear. There is a high affinity Ca^{2+} binding site which must be filled in order for the Mn cluster to assemble (Blubaugh et al., 1990). This Ca^{2+} can be removed by either relatively harsh treatments (Kalosaka et al., 1990) or by lanthanide substitution (Bakou et al., 1992). In addition, there at least one more loosely bound Ca^{2+} ion which is necessary for oxygen evolution but not for the assembly of the OEC (Tamura et al., 1987; Miller et al., 1989; Tamura et al., 1989) and can be removed by milder treatments such as a low pH incubation with citrate (Ono et al., 1988). Recent studies using radioactive $^{45}Ca^{2+}$ indicate that there is only one Ca^{2+} associated with oxygen evolution capability (Adelroth et al., 1995). The affinity of the more loosely bound calcium depends on the redox state of the OEC (Boussac et al., 1988c).

A number of different cations have been substituted into calcium binding sites, but only preparations with Sr^{2+} and VO^{2+} still evolve oxygen, albeit at a lower rate (Debus, 1992; Yocum, 1991). Much attention has been focussed on Sr^{2+}-substituted PSII preparations (PSII-Sr). PSII-Sr samples exhibit altered multiline signals in the S_2 state (Boussac et al., 1988a; Boussac et al., 1988b; Latimer et al., 1995). This, together with the dependence of the affinity of the more loosely bound calcium on the redox state of the Mn and the need for Sr^{2+} in the absence of Ca^{2+} for oxygen evolution, suggest that at least one calcium binding site may be in close proximity to the Mn cluster.

As x-ray absorption spectroscopy (XAS) is a powerful tool for structural characterization, it has been applied to PSII-Sr samples by several laboratories (Latimer et al., 1995; Riggs-Gelasco et al., 1996). Using different PSII preparations as well as different biochemical treatments to replace the Ca^{2+} with Sr^{2+}, both groups see the altered multiline signals of PSII-Sr samples, but no change in the XANES as compared to either native or Ca^{2+}-repleted PSII samples. This indicates that Sr^{2+}-substitution does not cause a drastic change in the average ligand coordination sphere or oxidation state of the Mn.

Changes in the Mn EXAFS upon Sr^{2+}-substitution have been observed by some laboratories, but not by others. Recent results from the Klein laboratory (Latimer et al., 1995) show that the most likely interpretation of an increase in the third peak of the Fourier transform of PSII-Sr samples is that a Sr scatterer at a distance of 3.54 Å replaces a Ca ion 3.46 Å away from the Mn cluster. They attribute the increase in Mn-Ca/Sr binding site distance to an ~0.1 Å increase in the ionic radius of Sr^{2+} as compared to Ca^{2+}. The other simulation components are similar to those reported previously for control preparations (DeRose et al., 1994; Penner-Hahn et al., 1990). In contrast, in data from the Penner-Hahn laboratory, there is no obvious change in the third peak of the Fourier transform (Riggs-Gelasco et al., 1996). Their best simulations over a 1.5 to 11.5 $Å^{-1}$ *k*-range contain the usual Mn-Mn distances of 2.7 Å and 3.3 Å in addition to a shell of oxygen atoms at 1.9 Å with a coordination number of only 3. Inclusion of a Sr scatterer instead of the Mn-Mn interaction at 3.3 Å decreases the quality of fit by ~9%. Although the lack of a need for a Sr contribution is not surprising from comparison of their Fourier transforms of PSII-Sr and native preparations, it is surprising that they have chosen to analyze a *k*-range which should favor both low Z elements and multiple scattering and that the simulations do not include a

realistic first coordination shell for the Mn. Standardizing the range of data used both for EXAFS analysis and Fourier transforms would be helpful in comparing, and perhaps understanding, the differences in data from different laboratories.

Substitution of calcium with lanthanides instead of Sr^{2+} is an attractive candidate for XAS studies as 1) the atomic number of a lanthanide is much larger than that of calcium or strontium, resulting in much larger backscattering amplitudes and therefore presumably more easily identifiable contributions to the EXAFS and 2) the lanthanides also have access to the tightly bound site, allowing structural studies on both types of calcium binding sites by XAS.

Mn EXAFS has been measured on samples with Dy^{3+}-substituted for Ca^{2+} (Riggs-Gelasco et al., 1996). In theoretical simulations, these researchers show that a Mn-Dy interaction at 3.3 Å should appear in the non-phase-corrected Fourier transform at an apparent distance ~0.23 Å longer than that expected for a Mn-Mn or Mn-Ca interaction at 3.3 Å. In the Fourier transforms of the experimental data on Dy^{3+}-substituted PSII samples, both the 2nd and 3rd peaks appear to shift to higher R values by ~0.13 Å. Simulations using a Dy backscatterer at 3.37 Å are ~4% better than similar fits with a Mn-Mn interaction at 3.26 Å. In spite of these results, the data has been interpreted as not indicative of a Mn-Ca binding site interaction at ~3.3 to 3.4 Å.

It can be concluded that unambiguous extraction of information from Mn EXAFS is difficult due to the large number of backscatterer contributions within 4 Å of the Mn and to the heterogeneity of the Mn sites. Presumably, only one or two of the four Mn may have a Ca neighbor in close proximity. Understanding the structure surrounding the calcium binding site(s) in PSII

will therefore require a different approach. Several possible ways of probing the calcium binding sites have been examined and are presented in this chapter.

Tb^{3+} has been shown to be a linear competitive inhibitor of Ca^{2+} binding to the OEC (Hatch et al., 1995) with an ~200-fold increase in site affinity for Tb^{3+} as compared to Ca^{2+}. In addition to Mn EXAFS studies of PSII samples with Tb^{3+} substituted for Ca^{2+}, Tb EXAFS experiments on samples which contain ≤ 2 Tb were instigated in order to gain further information about the Ca binding site(s), from the point of view of the Tb. These are the first EXAFS experiments probing the Ca binding site which are not from the Mn point of view.

Examining the Ca EXAFS on PSII preparations which have had all but the 2-3 Ca associated with PSII removed would by far be the most sensitive EXAFS probe of the calcium binding site(s). Both the experimental difficulties associated with these measurements and the preliminary Ca EXAFS results are presented in this chapter.

Tb^{3+} Substitution

Mn and Tb EXAFS samples were provided by C.E. Hatch and R. Bradley in the W.D. Frasch lab (Arizona State University). Samples were prepared by resuspending isolated PSII particles (Boussac et al., 1988b) to 0.2 mg chlorophyll/ml in a buffer containing 10 mM NaCl, 25 mM Mes, and 30 μM $TbCl_3$ at pH 6.5. Washing with 1 mM EDTA reduced the Tb concentration to 8 Tb per 4 Mn as determined by atomic absorption spectroscopy and inhibited oxygen evolution by 90% (PSII-Tb). Further reduction of the Tb concentration to ≤ 2 Tb per 4 Mn required washing the pellet with 70 mM NTA (pH 6.5) (PSII-Tb-lo). The extrinsic polypeptides which are released during incubation

with lanthanides were reconstituted in the final preparation of the PSII-Tb samples. For the Tb EXAFS experiments, the PSII-Tb-lo samples contained 0.94 Tb per 4.0 Mn, as determined by atomic absorption spectroscopy.

The addition of Ln^{3+} or Dy^{3+} to PSII preparations has been found to inhibit the S_1 to S_2 transition (Bakou et al., 1992). Measurements of the relaxation enhancement of the nearby tyrosine residue, Y_D^+, observed upon illumination of PSII-Tb samples that were prepared as described earlier, however, indicate that the turnover to the S_2 state does still occur. This relaxation effect is larger for PSII-Tb preparations than for Ca^{2+}-containing samples (Frasch et al., 1987) which has been interpreted as the faster relaxing Tb^{3+} contributing significantly to the relaxation enhancement of Y_D, but too far away from the radical to completely eliminate this signal. Neither of the characteristic EPR signals from the S_2 state, the so-called "multiline" around g=2 (Dismukes et al., 1981; Hänsson et al., 1982) or the g=4.1 signal (Casey et al., 1984; Zimmermann et al., 1984) have to date been reported from PSII-Tb preparations.

Mn K-edge spectra were measured on NSLS Beamlines X19A and X10C (Sansone et al., 1991) using Si(220) and Si(111) monochromator crystals, respectively, and Tb L_{II}-edge spectra on Beamline X19A with Si(311) crystals. Vertical entrance slits to the monochromator were set at 2 mm. Samples were kept between 12 and 18 K with an Oxford cryostat. A single scattering approximation used tabulated phase and amplitude functions (McKale et al., 1986) for the simulations. The Fourier-filtered data were back-transformed over several different ranges and analyzed before fitting the raw data.

Figure 7.1: Mn EXAFS of Photosystem II Samples which have Tb^{3+} substituted for Ca^{2+}. Left: Raw data (solid line) and simulation (dotted line) of the Mn EXAFS of PSII-Tb. Right: Fourier transforms of the raw data (solid line) and simulation fit (dotted line) to the Mn EXAFS of PSII-Tb. The Fourier transforms have been phase corrected for a Mn backscatterer ($R_{apparent} \approx R_{actual}$).

Intensity (a.u.)
8
6
4
2
0
-2
-4
-6
4
6
8
10
12
k (Å^{-1})
Intensity (a.u.)
1.4
1.2
1
0.8
0.6
0.4
0.2
0
0 1 2 3 4 5 6 7
R (Å)

The Mn K-edge EXAFS of PSII-Tb samples is presented in Figure 7.1 along with the Fourier transform of the data. The simulation results for a *k*-range of 3.5 to 11.5 $Å^{-1}$ are shown in the same figure and tabulated in Table 7.1. Three main peaks are observable in the Fourier transform. The first peak can be fit with a shell of O at 1.88 Å and a shell of N at 2.19 Å. Adding a third component results in shells of O at 1.90 Å and 2.39 Å and a shell of N at 2.19 Å. This reduces the overall fit error by > 50%, with very little change in the components of the second and third peaks. Attempts were made to fit the second and third peaks with a variety of backscatterers: C, N, O, S, Cl, Ca, Mn, and Tb. The second peak was nicely simulated by 1.3 Mn at a distance of 2.75 Å. The third peak was best fit using 0.5 Mn at a distance of 3.36 Å. These coordination numbers and distances are consistent with those that have been reported for control S_1 preparations (DeRose et al., 1994; Penner-Hahn et al., 1990). Neither peak requires another component for the fit, as can be seen upon examination of Figure 7.1. The Debye-Waller disorder term for the Mn shell at 2.75 Å is quite large compared to the other shells, suggesting that there is heterogeneity in the Mn-Mn interactions after Tb^{3+} substitution. When allowed to separate into two separate interactions, distances of 2.70 Å and 2.81 Å were obtained. A decrease in the Debye-Waller term was observed although the quality of fit was not significantly improved (≥ 1% improvement). Each addition of a subsequent shell of backscatterers improved the quality of fit between 16 and 43%.

A search profile for the most likely Mn-Tb distance yielded a a shell of 0.4 Tb at 4.05 Å. However, it must be cautioned that upon addition of this component the fit becomes overdetermined, the quality of the fit is only increased by 5%, and the corresponding peak in the Fourier transform is barely above the noise level of the data. Fitting of the data with Tb or Ca

Table 7.1: Simulation parameters for Mn EXAFS of PSII-Tb. The raw data was fit from 3.5 to 11.5 $Å^{-1}$.

Coordination Number and Type of Backscatterer	Distance	σ^2	ΔE_0	f
1.9 O	1.90 Å	0.0010	-8.8	80
2.3 N	2.19 Å	0.0010	-8.9	
1.8 N	2.39 Å	0.0027	-8.8	
1.3 Mn	2.78 Å	0.0100	-9.6	
0.5 Mn	3.39 Å	0.0048	-9.6	

$f = (\Sigma | X(k)_{exp} - X(k)_{fit} |^2)/N_{points}$

instead of the Mn backscatterer at 3.39Å resulted in a fit error which was worse by more than a factor of five. Attempts to include a shell of Tb at either 3.41 or 4.36Å changed the quality of the fit by less than 2%. Addition of a shell of Tb at 3.33Å decreased the quality of fit by ~4 %.

This data suggests that the Ca binding sites that are accessible to Tb substitution either are located at least 4 Å away from the Mn cluster or have a very large disorder, making the Mn-Tb interaction(s) unobservable by Mn EXAFS.

Tb EXAFS on samples which contain ≤ 3 Tb should provide a simpler view of the Ca binding site(s) as compared to that reconstructable from the Mn EXAFS. The difficulty of the experiment lies in the quantitation of the Tb. In samples which have too many Tb per PSII, the Tb EXAFS is the result of contributions from Tb ions occupying the Ca binding sites of interest as well as adventitious Tb^{3+}. Any Mn backscattering contribution that may be present is then diluted and there is less chance of it being observed.

The energies of the three Tb L-edges in order of diminishing intensity are: the L_{III} edge at 7514 eV, L_{II} at 8252 eV, and L_I at 8708 eV. Several factors

must be weighed when deciding which L-edge to measure. The highest intensity transition is desirable for signal to noise reasons. The longer the *k*-range, the better the likelihood that EXAFS will be able to resolve individual backscatterers at similar distances. The L_{III} edge optimizes both of these considerations, however, the main fluorescence decay from this transition is unresolvable from Fe K_α fluorescence. PSII preparations typically contain a significant amount of both Fe and Cu. The L_I edge is also not a possibility as, in addition to having the weakest intensity, it also has the shortest *k*-range (Cu K-edge ~8979 eV). The limited range of L_{II} EXAFS was therefore determined to be the only option for measuring Tb EXAFS.

Tb L_{II} EXAFS on PSII-Tb-lo samples containing ~1 Tb per PSII are presented in Figure 7.2. Due to the low signal to noise ratio, this data was smoothed by 0.3 $Å^{-1}$ and only a *k*-range of 2.25 to 9.00 $Å^{-1}$ was analyzed. Both the raw EXAFS and Fourier filtered data were simulated and similar results were obtained. For the simulations presented in Figure 7.3 and summarized in Table 7.2, only data from 1.39 $Å^{-1}$ to 3.69 $Å^{-1}$ was Fourier filtered and analyzed. The best fit included shells of oxygen at 2.44 Å and 2.87 Å. This is consistent with a survey on lanthanide binding in proteins (Evans, 1990) which found that the most frequent souce of oxygen ligation to Ln^{3+} ions are carboxyl groups and that there are no nitrogen ligands. Additional oxygen ligands are provided by carbonyl or hydroxyl groups or water. A search profile for a Tb-Mn/Fe interaction at ~3.33 Å yielded a minimum with a fit quality on the order of at least 50% better than other possible backscatterers (C, N, O, S, Cl, Ca, Tb), see Figure 7.4. Although a Tb-Fe interaction cannot be ruled out on the basis of this data alone, Fe has not been implicated as a cofactor for oxygen evolution and it is therefore more likely to be a Mn in

Figure 7.2: Tb EXAFS of Photosystem II Samples which have Tb^{3+} substituted for Ca^{2+}. Left: Raw (solid line) and smoothed data (dotted line) of the Mn EXAFS of PSII-Tb-lo. Right: Fourier transforms of the raw (solid line) and smoothed data (dotted line) data. The Fourier transforms have been phase corrected for a Mn backscatterer ($R_{apparent} \approx R_{actual}$).

Intensity (a.u.)
50
0
-50
0
2
4
6
8
10
k (Å-1)
Intensity (a.u.)
3
2.5
2
1.5
1
0.5
0
0
2
4
6
8
10
R (Å)

Figure 7.3: Tb EXAFS of Photosystem II Samples which have Tb^{3+} substituted for Ca^{2+}. Left: Filtered Tb EXAFS of PSII-Tb-lo (solid line) and simulation (dotted line). Right: Fourier transforms of the filtered Tb EXAFS of PSII-Tb-lo (solid line) and simulation (dotted line). The Fourier transforms have been phase corrected for a Mn backscatterer ($R_{apparent} \approx R_{actual}$).

Intensity (a.u.)
10
5
0
-5
-10
2
3
4
5
6
7
8
9
k (Å^{-1})
Intensity (a.u.)
2
1.5
1
0.5
0
0
1
2
3
4
5
6
7
R (Å)

Table 7.2: Simulation parameters for Tb EXAFS of PSII-Tb-lo. The data was Fourier filtered from 1.39 Å to 3.69 Å and fit from 2.25 to 9.00 $Å^{-1}$.

Coordination Number and Type of Backscatterer	Distance	σ^2	ΔE_0	f
5.0 O	2.43 Å	0.001	-10	472
6.0 O	2.43 Å	0.00680	-10	166
5.7 O	2.87 Å	0.001	-10	
6.0 O	2.42 Å	0.00491	-10	31
3.9 O	2.86 Å	0.001	-10	
2.0 Mn	3.34 Å	0.00235	-10	
5.9 O	2.44 Å	0.0041	-7.2	20
3.3 O	2.87 Å	0.0010	-7.2	
1.7 Mn	3.33 Å	0.0010	-11.1	

$f = (\Sigma | X(k)_{exp} - X(k)_{fit} |^2)/N_{points}$

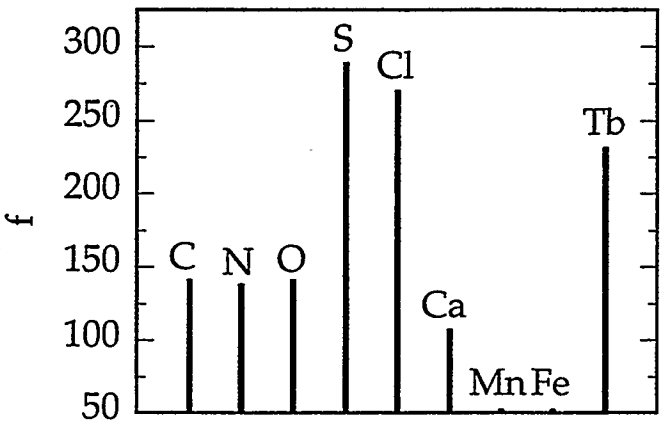

Figure 7.4: Search profile for a backscatterer at 3.3-3.4 Å. The least squares quality of fit parameter is defined as $f = (\Sigma | X(k)_{exp} - X(k)_{fit} |^2)/N_{points}$.

close proximity to the calcium binding site(s). The second and third shells of backscatterers improved the fit quality by 65% and 80%, respectively.

This preliminary data shows the potential of Tb EXAFS as a more sensitive probe of Mn-Tb interactions than Mn EXAFS. In spite of having a limited range of data collection, these results are consistent with at least one terbium-filled calcium binding site located ~3.4 Å away from the Mn cluster.

Ca EXAFS

A more powerful probe of the Ca binding site(s) near the OEC would be to measure Ca EXAFS. This would allow measurement on fully functional samples. In addition, a much larger *k*-range is obtainable as compared to Mn or Tb EXAFS - allowing for better resolution of multiple components.

One of the problems of this experiment is making certain that all adventitious Ca^{2+} is removed from the sample. Extreme care must also be taken to rid the glassware and sample holders of any adventitious Ca^{2+} which would also contribute to the Ca EXAFS, diluting the signals associated with the calcium binding site(s) near the OEC. Another difficulty associated with measuring Ca EXAFS is that the Ca K-edge binding energy occurs at ~4038.5 eV, an energy region where the absorption cross sections of nitrogen and oxygen are still quite high. This requires the sample to minimally be in a helium atmosphere, with a vacuum chamber being an even better alternative.

Besides PSII samples which have only 2 Ca per binding site and still exhibit similar activity to control preparations, another interesting candidate for Ca EXAFS experiments are Ca^{2+}-depleted preparations which presumably have only one Ca^{2+} ion remaining in the "tightly" bound site not necessary for oxygen evolution. In addition to this calcium binding site being

Figure 7.5: Preliminary Ca EXAFS of Photosystem II. Samples have ~12 Ca^{2+} per PSII. Left: Raw Ca EXAFS of PSII-Ca samples. Right: Fourier transform of the raw EXAFS data. The Fourier transforms have been phase corrected for a Mn backscatterer ($R_{apparent} \approx R_{actual}$).

Intensity (a.u.)
40
30
20
10
0
-10
-20
-30
-40
4
6
8
10
12
14
k (Å^{-1})
Intensity (a.u.)
3.5
3
2.5
2
1.5
1
0.5
0
0
1
2
3
4
5
6
7
R (Å)

interesting of itself, subtracting the Ca^{2+}-depleted data from the 2 Ca/PSII spectrum would allow examination of just the calcium essential for oxygen evolution. This would, however, require a very high signal to noise ratio.

BBY particles (Boussac et al., 1988b) used for preliminary Ca EXAFS experiments were isolated by G.A. Lorigan in the R.D. Britt lab (University of California, Davis). These samples had much of the adventitious Ca removed by dialysis (PSII-Ca) and were later shown to contain 12 Ca^{2+} per PSII reaction center, as determined by atomic absorption spectroscopy.

X-ray spectra were measured on NSLS Beamline X19A with Si(111) monochromator crystals. Vertical entrance slits to the monochromator were set at 2 mm. Samples were kept at ≤ 20 K with an Janis cryostat inside a UHV chamber.

The first Ca EXAFS data from PSII is shown in Figure 7.5. A survey of 27 Ca^{2+} binding sites in 17 different proteins indicates that all ligands to the Ca^{2+} are oxygen atoms. Coordination numbers vary from 6-8 and these distances are between 2.1 and 2.6 Å. Consistent with this, the Fourier transform of PSII-Ca EXAFS shows a large first peak at ~2.2Å.

A Ca-Mn interaction at ~3.5Å would be consistent with both Mn EXAFS data from the Klein group and the Tb EXAFS results presented here and may contribute to the Ca EXAFS. However, experiments on PSII preparations which have ≤ 3 Ca per PSII are necessary before information which is both useful and believeable can be extracted from the Ca EXAFS. The large *k*-range obtainable from Ca EXAFS on PSII suggests that, once quantitation problems can be overcome, this will be a powerful technique for probing the calcium binding sites associated with Photosystem II.

The Proximity of Ca^{2+} to the OEC

From the experiments presented here and those reviewed in the introduction to this chapter, it appears that observation of a calcium binding site from analysis of Mn EXAFS is extremely difficult. Tb^{3+} substitution affects the short Mn-Mn interactions, the distances for the two Mn-Mn dimers becoming 2.70 Å and 2.81 Å. Sensitivity of this interaction to biochemical perturbations has been observed previously. In NH_3-treated samples, the short Mn-Mn distances are best simulated by two separate interactions, one at 2.71 Å and the other at 2.86 Å (Dau et al., 1995). A Tb shell does not significantly improve the quality of the fit for the Mn EXAFS data on PSII-Tb samples. This suggests that if there is a Mn-Tb interaction near the OEC, it is too weak to be directly detected using this technique.

In spite of difficulties associated with Tb EXAFS experiments, structural data measured from the viewpoint of the calcium binding site(s) does appear to simplify the situation. This data is summarized in Table 7.3.

A distance of 3.47 Å between the Ca binding site(s)and the Mn cluster has been proposed based on conventional Mn EXAFS (Latimer et al., 1995). The preliminary results from Tb EXAFS suggest a 3.33Å Tb-Mn distance. The distance decreases by 0.14 Å upon substitution of Tb^{3+}, along with a corresponding decrease in the ionic radius of 0.07 Å. The correlation of ionic radius with Mn-Ca interaction was also observed by Latimer et al., where the ionic radius of the binding site occupant increased by 0.13 Å and the distance observed by EXAFS increased by 0.07 Å. There is also an inverse correlation between the strength as a Lewis acid of the Ca binding site occupant and the distance to the Mn cluster.

Table 7.3: A comparison of results from Mn, Tb, and Ca EXAFS experiments. The binding site occupants are listed in order of decreasing Lewis acidity.

Binding Site Occupant	Ionic Radius	Interaction	XAS Technique
Tb^{3+}	0.92Å	Tb-Mn @ 3.33 Å	Tb EXAFS
Ca^{2+}	0.99Å	Mn-Ca @ 3.47 Å**	Mn EXAFS
Sr^{2+}	1.12Å	Mn-Sr @ 3.54 Å**	Mn EXAFS

** (Latimer et al., 1995)

Clearly, from measuring EXAFS from the Ca binding site(s) point of view much more information about the OEC can be learned than has previously been obtained from just Mn EXAFS. Although there are difficulties in both biochemical preparations and data collection of the Ca EXAFS, these experiments are a more sensitive probe than either Mn or Tb EXAFS and should offer a more complete understanding of the calcium binding sites associated with Photosystem II in the near future.

References

Adelroth, P.; Lindberg, K.; Andreasson, L.E. *Biochemistry* **1995** *34*, 9021-9027.

Bakou, A.; Buser, C.; Dandulakis, G.; Brudvig, G.; Ghanotakis, D. *Biochim. et Biophys. Acta* **1992** *1099*, 131-136.

Blubaugh, D.J.; Cheniae, G.M. *Plant Physiol.* **1990** *93*, 22.

Boussac, A.; Rutherford, A.W. *Chem. Scr.* **1988a** *28A*, 123-126.

Boussac, A.; Rutherford, A.W. *Biochemistry* **1988b** *27*, 3476-3483.

Boussac, A.; Rutherford, A.W. *FEBS Lett.* **1988c** *236*, 432-436.

Casey, J.L.; Sauer, K. *Biochim. Biophys. Acta* **1984** *767*, 21-28.

Dau, H.; Andrews, J.C.; Roelofs, T.A.; Latimer, M.J.; Liang, W.; Yachandra, V.K.; Sauer, K.; Klein, M.P. *Biochemistry* **1995** *34*, 5274-5287.

Debus, R.J. *Biochim. Biophys. Acta* **1992** *1102*, 269-352.

DeRose, V.; Mukerji, I.; Latimer, M.; Yachandra, V.; Sauer, K.; Klein, M.P. *J. Am. Chem. Soc.* **1994** *116*, 5239-5249.

Dismukes, G.C.; Siderer, Y. *Proc. Natl. Acad. Sci. USA* **1981** *78*, 274-278.

Evans, C.H. *Biochemistry of Lanthanides;* Frieden, E., Ed., Plenum Press: New York, 1990.

Frasch, W.; Mei, R. *Biochemistry* **1987** *26*, 7325-7332.

Hänsson, O.; Andreasson, L.E. *Biochim.Biophys. Acta* **1982** *679*, 261-268.

Hatch, C.; Grush, M.; Bradley, R.; LoBrutto, R.; Cramer, S.; Frasch, W. in *Photosynthesis: from Light to Biosphere, Vol. II;* Mathis, P., Ed., Kluwer Academic Publishers: Dordrecht, 1995, pp 425-429.

Kalosaka, K.; Beck, W.F.; Brudvig, G.W.; Cheniae, G.M. in *Current Research in Photosynthesis, Vol. I;* Baltscheffsky, M., Ed, Kluwer Academic Publishers: Dordrecht, 1990, pp 721-724.

Latimer, M.J.; DeRose, V.J.; Mukerfi, I.; Yachandra, V.K.; Sauer, K.; Klein, M.P. *Biochemistry* **1995** *34,* 10898-10909.

McKale, A.G.; Knapp, G.S.; Chan, S.-K. *Phys Rev. B* **1986**, *33,* 841-846.

Miller, A.-F.; Brudvig, G.W. *Biochemistry* **1989** *28,* 8181-8190.

Ono, T.-A.; Inoue, Y. *FEBS Lett.* **1988** *227,* 147-152.

Penner-Hahn, J.E.; Fronko, R.; Pecoraro, V.; Yocum, C.; Betts, S.; Bowlby, N. *J. Am. Chem. Soc.* **1990** *112,* 2549-2257.

Riggs-Gelasco, P.J.; Mei, R.; Ghanotakis, D.F.; Yocum, C.F.; Penner-Hahn, J.E. *J. Am. Chem. Soc.* **1996** *118,* 2400-2410.

Sansone, M.; Via, G.; George, G.N.; Meitzner, G.; Hewitt, R. *X-ray Absorption Fine Structure;* Hasnain, S.S., Ed., Ellis Horwood Ltd.: W. Sussex, England, 1991, pp. 656-658.

Tamura, N.; Cheniae, G.M. *Biochim. Biophys. Acta* **1987** *890,* 179-194.

Tamura, N.; Inoue, Y.; Cheniae, G.M. *Biochim. Biophys. Acta* **1989** *976,* 173-181.

Yocum, C.F. *Biochim. Biophys. Acta* **1991** *1059,* 1-15.

Zimmerman, J.-L.; Rutherford, A.W. *Biochim. Biophys. Acta* **1984** *767,* 160-167.

Conclusion

The major motivation for this thesis has been to use synchrotron radiation to probe the structure and function of the Mn tetramer responsible for catalyzing the oxidation of water associated with Photosystem II in green plants. To this end, novel x-ray techniques such as Mn L-edge absorption and high resolution x-ray fluorescence have been developed for application to Mn-containing complexes. These two techniques, as well as the more conventional EXAFS, have been applied to Photosystem II, with some successes and some near misses.

The first Mn L-edge absorption spectra of a Mn metalloprotein have been presented here (Chapter 4). Both reduced and super-oxidized Mn catalase were examined by fluorescence detected soft x-ray absorption spectroscopy, and their Mn L-edge spectra are dramatically different. The spectrum of reduced Mn(II)Mn(II) catalase has been interpreted by ligand field atomic multiplet calculations and by comparison to model compound spectra. The analysis finds a 10Dq value of ~1.1 eV, consistent with coordination by predominately nitrogen and oxygen donor ligands. For interpretation of mixed valence Mn spectra, an empirical simulation procedure based on the addition of homovalent model compound spectra was developed and applied to a variety of Mn complexes (Chapter 2), including a polynuclear "Mn_{16}" aggregate, and super-oxidized Mn catalase (Chapter 4).

I have used Mn catalase as a test case for the L-edge experiments, learning the subtleties involved in measuring Mn protein L-edge spectra and testing the sensitivity of simulation routines on this partially characterized system. Most of the L-edge data has been previously published elsewhere (Grush et al., 1996). Applying this technique to Photosystem II has been a

challenge (Chapter 5). Although a very preliminary result has been obtained, use of the L-edge technique to extract oxidation state information from this system awaits a more efficient detector.

In light of difficulties in probing the Mn L-edges of Photosystem II, help in deciphering the Mn oxidation state scenario was obtained from the high resolution fluorescence technique. The position of the Kβ emission is strongly correlated with oxidation state (Chapter 3). Kβ results support oxidation states of $Mn(III)_2(IV)_2$ for the S_1 state of Photosystem II (Chapter 6) while preparations which were reduced by hydroquinone were found to contain predominately Mn(II). More precise oxidation state determinations await Mn L-edge data from this metalloprotein.

The first demonstration that chemical shifts in x-ray fluorescence energies can be used to obtain site-selective x-ray absorption spectra is presented here and looks promising from both qualitative and quantitative viewpoints (Chapter 3). The physical mixture and trimer experiments have been presented elsewhere (Grush et al., 1995). The site-selective XANES technique has been applied to both control and reduced preparations of Photosystem II (Chapter 6). Oxidation state specific EXAFS (Chapter 3) promises to become invaluable in the attainment of information about specific Mn environments in metal clusters. However, before site-selective EXAFS can become a powerful tool for studying the structure of the oxygen-evolving complex, improvements in the signal to noise ratio are sorely needed (Chapter 6).

There are many cases where fluorescence lines change with chemical environment. Useful chemical shifts in emission spectra are known for heavier metals such as the rare earths (Ekstig et al., 1970), for high-spin versus low-spin iron (Peng et al., 1994), for different oxidation states of sulfur (Nilar

et al., 1990), and even for light atoms such as carbon (Skytt et al., 1994). With improvements in signal-to-noise ratios, site-selective XAS using high resolution fluorescence detection should become a more common and valuable technique with broad applicability.

The energy separation between Kβ and Kβ' regions is easily resolvable using the high resolution fluorescence technique. This results in the possibility of measuring spin-selective EXAFS. The first detection of SPEXAFS using high resolution detected Mn fluorescence is shown for MnF_2 (Chapter 3).

The oxygen-evolving complex has been intensively studied by conventional Mn EXAFS. When studying a small biochemical perturbation on a complex system such as the OEC, there are limitations in the sensitivity of the Mn EXAFS technique (Chapter 7). Mn EXAFS experiments on PSII samples which had Tb^{3+} substituted for Ca^{2+} failed to see a Tb backscatterer, as has been presented elsewhere (Hatch et al., 1995). This is presumably due to both the weakness of the interaction and other backscatterers contributing to the EXAFS at similar distances. I have investigated the potential of using Tb and Ca EXAFS as probes of the Ca^{2+} binding site(s) thought to be in close proximity to the Mn cluster. These studies are the first XAS probes of the calcium binding sites not taken from the Mn point of view. A Mn-Ca^{2+} binding site interaction was determined to have a distance of ~3.3 Å from Tb EXAFS experiments on PSII-Tb samples.

The long *k*-range obtainable in Ca EXAFS experiments on PSII preparations and the ability to examine fully functional samples make this technique the more powerful probe of the calcium binding site(s). Future work on this system will undoubtedly clear up much speculation about the location of the calcium binding sites associated with Photosystem II.

The x-ray absorption techniques of Mn L-edge Spectroscopy and High Resolution Mn Kβ Fluorescence have been developed for application to metalloproteins. These techniques, in addition to conventional EXAFS, have been applied to the Mn cluster associated with Photosystem II in order to learn about the structure of this important enzyme.

Ekstig, B.; Källne, E.; Noreland, E.; Manne, R. *Phys. Scripta* **1970**, *2*, 38-44.

Grush, M.M.; Chen, J.; Stemmler, T.L.; George, S.J.; Ralston, C.Y.; Stibrany, R.T.; Gelasco, A.; Gorun, S.M.; Christou, G.; Penner-Hahn, J.E.; Cramer, S.P. *J. Am. Chem. Soc.*, **1996** *118*, 65-69.

Grush, M.M.; Christou, G.; Hämäläinen, K.; Cramer, S.P. *J. Am. Chem. Soc.* **1995** *117*, 5895-5896.

Hatch, C.; Grush, M.; Bradley, R.; LoBrutto, R.; Cramer, S.; Frasch, W. in *Photosynthesis: from Light to Biosphere, Vol. II*; Mathis, P., Ed., Kluwer Academic Publishers: Dordrecht, 1995, pp 425-429.

Nilar, S. H.; Zerner, M. C.; Manne, R. *Chem. Phys. Lett.* **1990**, *168*, 260-264.

Peng, G.; Wang, X.; Randall, C.R.; Moore, J.A.; Cramer, S.P. *Appl. Phys. Lett.* **1994**, *65*, 2527-2529.

Skytt, P.; Glans, P.; Mancini, D.C.; Guo, J.-H.; Wassdahl, N.; Nördgren, J. *Phys. Rev. B.* **1994**, *50*, 10457-10461.